CHAPTER 1

INTRODUCTION AND THEORETICAL BACKGROUND

1.1 What is a Quantum Dot (QD)?

Low-dimensional nanometer-sized systems have defined a new research area in condensed-matter physics over the last 20 years. Modern semiconductor processing techniques allowed the artificial creation of quantum confinement of only a few electrons. Such finite fermion systems have much in common with atoms, yet they are man-made structures, designed and fabricated in the laboratory. Usually they are called ‘‘QDs’’ referring to their quantum confinement in all three spatial dimensions. Molecular systems or metallic islands can also serve as QDs.

A QD has a unique characteristic, usually called the charging energy, which is analogue to the ionization energy of an atom. This is the energy required to add or remove a single electron from the dot. Because of the analogies to real atoms, QDs are sometimes referred to as artificial atoms. The atom-like physics of dots is studied by measuring their transport properties, that is, their ability to carry an electric current. The QD can be connected to source and drain electrodes through tunnel barriers for current flow and can be coupled to a gate electrode by which one can control the electrostatic energy of the QD and the number of electrons in the dot one by one. This system is called a single electron transistor and a schematic picture is shown in Fig. 1.1.

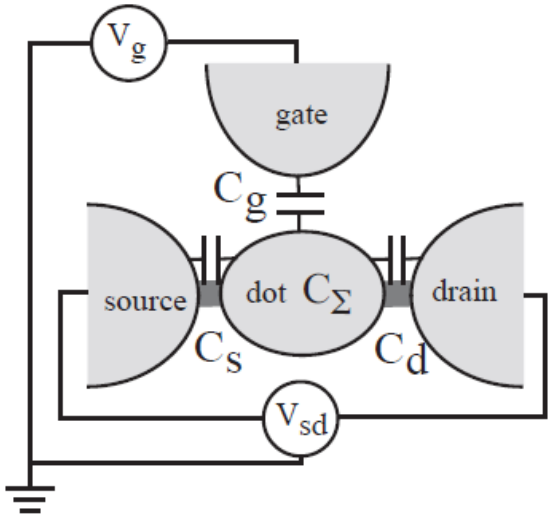

Figure 1.1: Schematic picture of a QD connected to source and drain contacts by tunnel junctions and to a gate by a capacitor.

1.2 Energy scales in a QD system

Transport properties of QDs connected to large metallic leads depend mainly on four energy scales, E_c the charging energy, Δ the energy level spacing, Γ the resonance width and $k_B T$ the thermal energy.

E_c, the charging energy, is the energy required to introduce an additional electron in the system. The charging energy is called the Coulomb blockade (CB) of tunneling and is given by the formula:

$$E_c = \frac{e^2}{C} = \frac{e^2}{4\pi\varepsilon\varepsilon_0 R} \qquad (1.2.1)$$

where ε_0 is the dielectric constant of air, ε is the dielectric constant of the surrounding media, C is the capacitance of the dot and R is the radius of the QD. The larger the size of the QD, the smaller is the energy which is required to add an electron into the dot.

Δ, the energy level spacing due to the energy quantization in the QD, depends on the dimensionality of the QD. Here the dimensionality is determined by the ratio of the electron Fermi wavelength λ_F and the dot length. The level spacing at the Fermi energy E_F for a system of size L with N electrons, including spin degeneracy, is:

$$\Delta = \begin{cases} \frac{N}{4} \cdot \frac{\hbar^2 \pi^2}{mL^2} & 1D \\ \frac{1}{\pi} \cdot \frac{\hbar^2 \pi^2}{mL^2} & 2D \\ \left(\frac{1}{3\pi^2 N}\right)^{1/3} \cdot \frac{\hbar^2 \pi^2}{mL^2} & 3D \end{cases} \qquad (1.2.2)$$

Here $\hbar$ is the Planck constant. For a one dimensional system (1D) system, the level spacing grows with increasing N. In a 2D QD it is constant, while in 3D it decreases as N increases.

Γ, the coupling of the dot to leads, from a classical point of view, is related to the tunneling rate of the electron from the lead to the dot and is inverse proportional to the time the electron "spends"

in the dot, $\Gamma = \frac{1}{RC}$. From a quantum point of view, it is the level broadening due to coupling to leads. In other words, Γ is related to the tunneling rate of the electron from the lead to the level in the dot. When the energy level is well connected to the leads, the tunneling rate of an electron which tunnels from the leads to that level is larger, and thus the electron "spends" less time in this level. This can be easily seen from the uncertainty principle: $\Gamma \cdot \Delta t \cong \hbar$.

When the coupling to the external leads is weak, Γ may be treated as a perturbation and is calculated by the perturbation theory. The first-order perturbation theory yields the Fermi golden rule:

$$\Gamma(\Delta F) = \frac{2\pi}{\hbar}\sum_i \sum_f \left|T_{if}\right|^2 f(E_i)(1-f(E_f))\delta(E_i - E_f - \Delta F) \qquad (1.2.3)$$

Where $f(E)$ is the Fermi distribution function. This width of the state is related by Fermi golden rule to the square of the matrix element for tunneling between the lead and the dot, $\left|T_{if}\right|^2$.

$$\Gamma = \pi N \upsilon \left|T_{if}\right|^2 \qquad (1.2.4)$$

υ is the density of states (DOS) in the lead, N is the number of leads. A convenient expression for the matrix element in terms of the lead and the dot wave functions, ψ_l and ψ_d, respectively, was derived by Bardeen[1], and can be expressed as,

$$\left|T_{if}\right| = \frac{\hbar^2}{m_*}\int_S dr\, \psi_l(r)\nabla\psi_d(r) \qquad (1.2.5)$$

where m_* is the effective mass and the surface S is the edge of the QD. The width Γ, then, depends on the square of the normal derivative of the dot wave function at the edge weighted by the lead wave function. The width then has the form[2]:

$$\Gamma[\psi_d] = \frac{2\pi\hbar^4}{m_*^2}\sum_l \rho_l \int_S dr_1 \cdot \nabla\psi_d(r_1) \times \int_S dr_2 \cdot \nabla\psi_d(r_2) * [\psi_l(r_1) * \psi_l(r_2)] \qquad (1.2.6)$$

The temperature, T, in the system supplies to the electron a thermal energy $k_B T$. If the thermal energy is larger than the charging energy it screens the charging effects in the QD.

1.3 Physical regimes in a QD

In this section we will review the main physical regimes in a QD. There are two main regimes, the weak coupling regime (also known as weak tunneling regime) and the strong coupling regime. The parameter which determines the weak/strong regime is the factor $g = \frac{\Gamma}{\Delta}$. The factor g determines the degree of coupling and distinguishes between the two regimes. When $g << 1$, the system is in the weak coupling regime, often called the closed dot regime, otherwise, when $g \geq 1$ the system is in the strong coupling regime or in other words the open dot regime.

In addition, one can distinguish between the classical regime and the quantum regime. The parameter that determines the classical/quantum regime is $\frac{k_B T}{\Delta}$.

In the **weak coupling regime** we can distinguish between three temperature regimes:

1. $\frac{e^2}{C} \leq k_B T$ - This regime is the high temperature limit. The conductance is independent of the electron number and the discreteness of charge cannot be resolved. The conductance is given by the Ohmic sum of the two barrier conductances $\frac{1}{G} = \frac{1}{G_{Left}} + \frac{1}{G_{Right}}$. This high temperature conductance is independent of the size of the dot and is characterized completely by the two barriers.

2. $h\Gamma < \Delta < k_B T < \frac{e^2}{C}$ - This is the **classical regime** where the thermal energy is larger than energy level spacing. In this regime many levels are excited by thermal fluctuations. This regime is described by the Orthodox model which will be discussed in section (1.4.1.1).

3. $k_B T$, $h\Gamma < \Delta < \frac{e^2}{C}$ - This is the **quantum regime**, where the thermal energy is smaller than the energy level spacing and only one or a few levels participate in transport.

1.4 Transport properties of a QD

By fabricating a transistor geometry as shown in Fig. 1.1, one can study transport properties when measuring the conductance as a function of the gate voltage or as a function of the bias voltage[3,4,5,6]. Throughout this section we will explain in details different types of measurements by which one can study the transport properties of a QD. In the following two sub-sections we will discuss the transport properties in the weak coupling regime (section (1.4.1)) and in the strong coupling regime (section (1.4.2)) while distinguishing between the classical and quantum regimes.

1.4.1 Transport properties of a QD in the weak coupling regime

In this section we will describe different types of transport measurements in a QD system and describe the conductance behavior in the weak coupling regime.

1.4.1.1 The Orthodox model (classical regime)

The classical regime was first studied by Kulik and Shekter[7]. In this case a continuum of energy levels in the QD participates in the conductance. This regime is usually described by the Orthodox model. In the following we describe the important principles of this model.

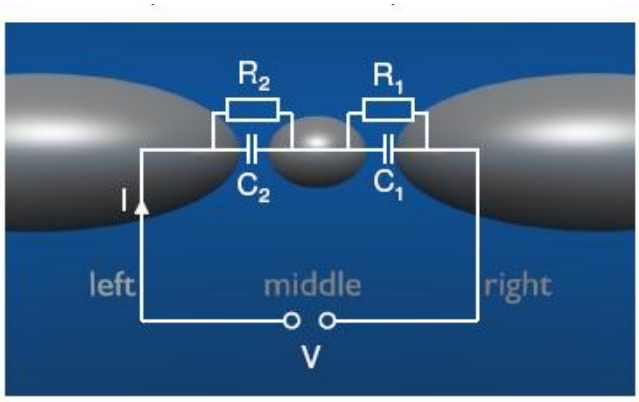

Figure 1.2: Schematic of a QD connected to two leads according to the Orthodox theory**.** Each electrode is considered as a resistor connected in parallel to a capacitor.

A schematic picture of a QD according to the Orthodox model is shown in Fig. 1.2. The device consists of two tunnel junctions coupled in series with small insulator between them, hence, this system is called Double Barrier Tunnel Junction (DBTJ). Each electrode is considered as a resistor connected in parallel to a capacitor. The middle section between the junctions is referred to as the dot.

This model describes the conductance by the total bias voltage and by the number of electrons in the dot. Applying voltage to the system causes two different voltage drops over the tunnel junctions:

$$V_1 = \frac{C_2}{C} V_{sd} - \frac{N \cdot e}{C} \qquad (1.4.1)$$
$$V_2 = \frac{C_1}{C} V_{sd} + \frac{N \cdot e}{C}$$

where C is the total capacitance of the dot, $C = C_1 + C_2 + C_g$, C_g being the capacitance between the dot and the gate electrode. In the Orthodox approach the conductance is found from the balance of the tunneling rates of electrons between the leads and the dot, with the rates being calculated in the lowest-order perturbation theory in the tunneling matrix element, as in Eq. (1.2.3). This lowest-order perturbation describes the sequential tunneling event. After integrating this equation the tunneling rates can be derived:

$$\Gamma = \frac{1}{e^2 R} \frac{\Delta E}{(1 - \exp(-\Delta E / k_B T))} \qquad (1.4.2)$$

Where R is the resistance of the barrier and ΔE represents the electrostatic energy difference of the system before and after the tunneling event. To this difference one should add the gain in energy due to the bias voltage, V_{sd}, and to the gate voltage, V_g. There are four different tunneling rates in the system: $\Gamma_{L\to D}, \Gamma_{D\to L}, \Gamma_{R\to D}, \Gamma_{D\to R}$, where the letters L, R, D denote the left barrier, the right barrier, and the dot, respectively. In case of symmetric barrier the tunneling rates at $T = 0$ and for $\Delta E < 0$, become:

$$\Gamma_{L\to D} = \frac{\Delta E}{e^2 R} = ((n + 0.5 - \frac{C_g \cdot V_g}{e}) \frac{e^2}{C} - \frac{eV_{sd}}{2}) \frac{1}{e^2 R}$$
$$\Gamma_{D\to L} = \frac{\Delta E}{e^2 R} = -((n + 0.5 - \frac{C_g \cdot V_g}{e}) \frac{e^2}{C} - \frac{eV_{sd}}{2}) \frac{1}{e^2 R} \qquad (1.4.3)$$
$$\Gamma_{R\to D} = \frac{\Delta E}{e^2 R} = ((n + 0.5 - \frac{C_g \cdot V_g}{e}) \frac{e^2}{C} + \frac{eV_{sd}}{2}) \frac{1}{e^2 R}$$

$$\Gamma_{D\to R}=\frac{\Delta E}{e^2R}=-((n+0.5-\frac{C_g\cdot V_g}{e})\frac{e^2}{C}+\frac{eV_{sd}}{2})\frac{1}{e^2R}$$

For $\Delta E>0$ we take all the tunneling rates to zero.

Tunneling through the island is a random process, so we cannot predict when an electron is going to tunnel. The Orthodox theory takes this into account by building a distribution function for the system which defines the probability ρ, at the time t, for the system to have N extra electrons on the island when the voltages V_{sd} and V_g are supplied. This probability depends on the tunneling rates in the DBTJ. This relation is demonstrated by the master equation. Let's define two quantities:

(1.4.4)
$$x(N)=\Gamma_{L\to D}(V_{sd},V_g,N)+\Gamma_{R\to D}(V_{sd},V_g,N)$$
$$y(N)=\Gamma_{D\to L}(V_{sd},V_gN)+\Gamma_{D\to R}(V_{sd},V_g,N)$$

The first quantity refers to a case where one electron has jumped onto the island leaving the system with (N+1)-state. The second quantity refers to a case where one electron has jumped off the island leaving the system in a (N-1)-state. Now we can write down the master equation:

(1.4.5)

$$\frac{\partial\rho(V_{sd},V_g,N,t)}{\partial t}=\rho(V_{sd},V_g,N-1,t)\cdot x(N-1)+\rho(V_{sd},V_g,N+1,t)\cdot y(N+1)-\rho(V_{sd},V_g,N,t)\cdot[x(N)+y(N)]$$

The first two terms demonstrate the contribution to the probability that the system should jump into the (N)-state from (N-1)-state or from (N+1) state. The last term gives a contribution that the system should leave the (N)-state, that's why its sign is minus.

If we look for steady state solutions for the master equation we take the derivative to zero:

(1.4.6)

$$0=\rho(V_{sd},V_g,N-1,t)\cdot x(N-1)+\rho(V_{sd},V_g,N+1,t)\cdot y(N+1)-\rho(V_{sd},V_g,N,t)\cdot[x(N)+y(N)]$$

The solution for this equation is calculated and the final expression for the current is given by the formula:

(1.4.7) $$I(V_{sd},V_g)=e\sum\rho(N,V_{sd},V_g)[\Gamma_{L\to D}(N,V_{sd},V_g)-\Gamma_{D\to L}(N,V_{sd},V_g)]$$

From Eq. (1.4.7) one can derive the conductance as a function of the bias voltage (shown in Fig. 1.6) and the gate voltage (shown in Fig. 1.4a).

In the following sections we will describe different types of transport measurements. We will present the predicted conductance behavior in the quantum regime and the classical regime. Here, all the formulas which are related to the classical regime are derived from the Orthodox model described above.

1.4.1.2 Gate voltage dependence

Experimentally, one can measure the linear conductance through the QD as a function of the gate voltage, V_g, applied to the gate electrode. The role of the gate voltage is to change the electrostatic energy of the system,

$$E = \frac{(Q - eN)^2}{2C} \quad (1.4.8)$$

Where Q is the charge of the QD, C is the total capacitance of the system and N is the averaged number of electrons in the dot, $N = \frac{C_g V_g}{e}$. The electrostatic energy of the system as a function of Q is a set of parabolas with minima at $Q_0 = \frac{C_g V_g}{2C}$. If charge were not quantized, Q_0, the charge which minimizes the electrostatic energy in Eq. (1.4.8), could attain any value by varying V_g. However, if the potential barriers separating the QD from the leads are high, the charge Q is quantized and is an integer in units of e. Thus, only discrete values of the energy E are possible. When $Q_0 = N \cdot e$, the ground state of the system corresponds to some integer value of charge, and states with different values of Q are separated by the electrostatic gap $\frac{e^2}{C}$. In other words when $Q_0 = N \cdot e$, an integral number of electrons minimize the energy E and the Coulomb interaction results in the same energy difference $\frac{e^2}{C}$ for increasing or decreasing N by 1. For all other values of Q_0 except for $Q_0 = -(N + \frac{1}{2}) \cdot e$, there is a smaller, but nonzero, energy for either adding or subtracting an electron. Under such circumstances no current can flow at low temperature. However, if $Q_0 = -(N + \frac{1}{2}) \cdot e$, when the values of the gate voltage correspond to half-integer

values of N, the state with $Q = -N \cdot e$ and that with $Q = -(N+1) \cdot e$ are degenerate and the gap vanishes. Since the ground state is degenerate in charge Q the charge fluctuates between the two values even at zero temperature. For example at $N = \frac{1}{2} \cdot e$ the ground state can have either $Q = 0$ or $Q = e$. Therefore at half-integer N, the tunneling of an electron into or out of the QD doesn't lead to the increase of the electrostatic energy of the system and the CB is lifted, hence, current can flow. Therefore, the peaks in conductance are periodic with V_g, occurring when $\frac{C_g \cdot V_g}{2C} = -(N + \frac{1}{2}) \cdot e$, spaced in gate voltage by $\frac{e^2}{C}$.

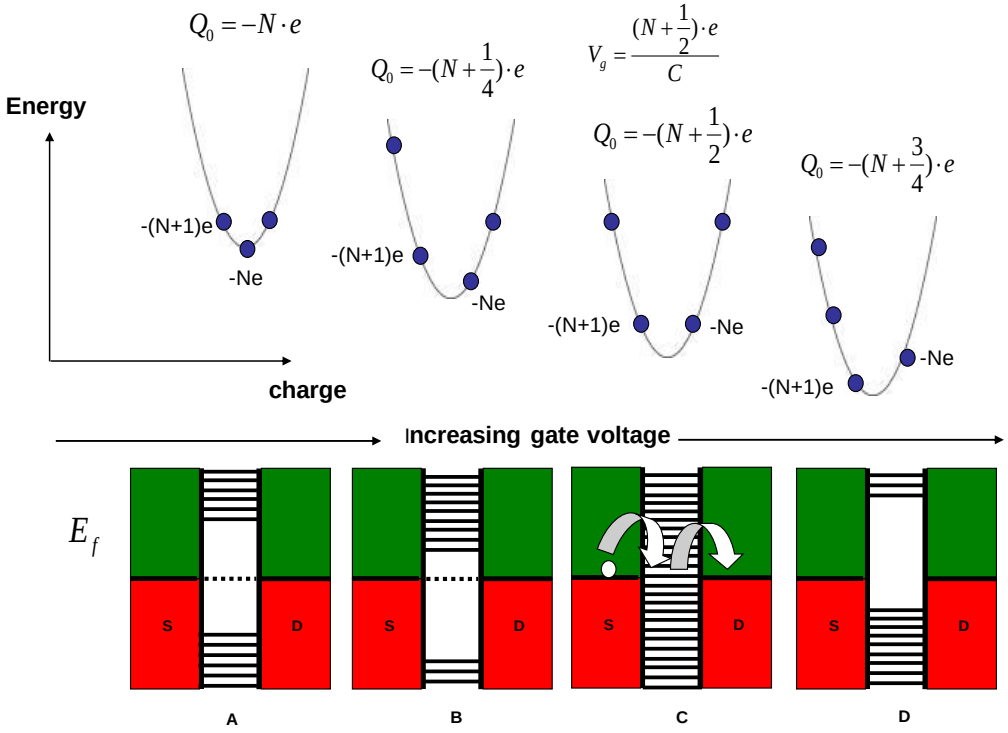

Figure 1.3: Total energy E (top) and tunnel energies (bottom) for a QD. As the gate voltage is increased the charge Q_0 for which the energy is minimized changes from $-N \cdot e$ and $-(N+\frac{3}{4}) \cdot e$. Only the points corresponding to discrete number of electron in the QD are allowed (dots on upper curves). Lines in the lower diagram indicate energies needed for electrons to tunnel onto the QD. When $Q_0 = -(N+\frac{1}{2}) \cdot e$ (diagram c) the gap in tunneling energies vanishes and current can flow.

There is a gap in the tunneling spectrum for all values of V_g except the charge-degeneracy points as shown in Fig. 1.3. As V_g is increased continuously the gap is pulled down relative to the Fermi energy until a charge-degeneracy point is reached. Upon moving through this point there is a discontinuous change in the tunneling spectrum. The gap collapses and then reappears shifted up by $\frac{e^2}{C}$. Simultaneously, the charge on the QD increases by 1 and the process starts over again. A charge degeneracy point and a conductance CB peak are reached every time the energy is increased by $\frac{e^2}{C}$, the amount necessary to add one electron to the QD. Hence, while sweeping the gate voltage, conductance peaks are observed with a periodicity V_g which corresponds to a change of energy by $\frac{e^2}{C}$.

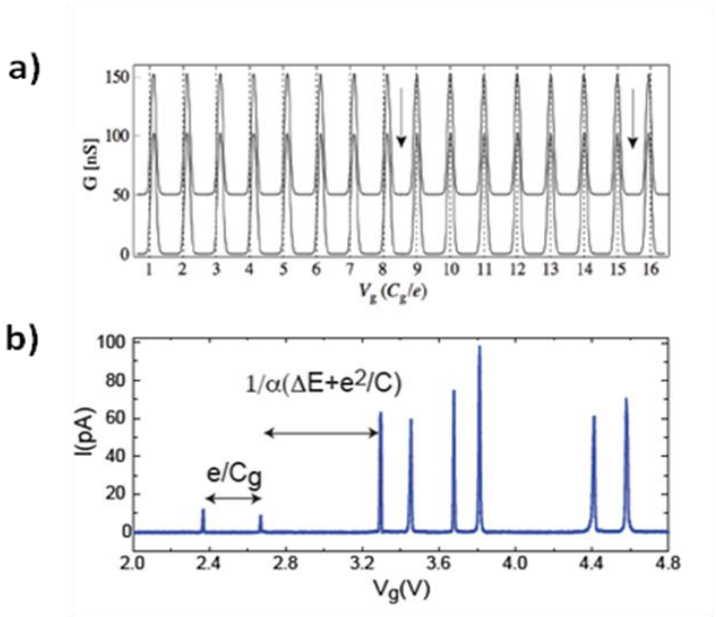

Figure 1.4: a) Typical conductance peaks in the classical regime obtained by the Orthodox model. **b)** Typical conductance peaks in the quantum regime.

The above explanation neglects the energy quantization in the dot and assumes that the energy is continuous. If the energy level spacing, Δ, cannot be neglected the CB peaks are separated by $\frac{e^2}{C}+\Delta$. In the classical regime the thermal energy exceeds the energy level spacing, hence Δ is

neglected and the CB peaks are period with a perfect periodicity of $\frac{e^2}{C}$. This is shown in Fig. 1.4a. In the quantum regime, however, the energy level spacing exceeds the thermal energy, hence the energy spectra should be taken into account. In this case the peaks are separated by $\frac{e^2}{C}+\Delta$ as shown in Fig. 1.4b.

An additional difference between the classical regime and quantum regime is the conductance line shape and its dependence on temperature.

In the classical regime the line shape of each conductance peak is given by:

$$\frac{G}{G_{\max}}=\frac{\Delta E/kT}{\sinh(\Delta E/kT)}\approx\cosh^{-2}(\frac{\Delta E}{2.5kT}) \qquad (1.4.9)$$

where $\Delta E=V_g-V_g(N=\frac{1}{2}\cdot e)$ and $G_{\max}=\frac{1}{2}\frac{G_L G_R}{G^L+G^R}$. Here G_L and G_R are the conductances of the left and the right barriers. In this regime the peak height is temperature independent and has the value $G=\frac{1}{2}\frac{G_L G_R}{G_L+G_R}$. The reason is that the $\frac{1}{T}$ temperature dependence of $G_{\max}$ associated with tunneling through an individual energy level is canceled by the T dependence of the number $\rho k_B T$ of levels participating in the conductance. Away from the center of the peak and at $T\to 0$, the tunneling of an electron into the QD is suppressed exponentially with gate voltage, because only a small fraction of electrons has the energy sufficient to overcome the electrostatic gap. The higher the temperature, the wider is of the peak. However, Eq. (1.4.9) is valid for low temperatures. When $k_B T$ approaches E_C, adjacent peaks start to overlap and the value of the conductance on the maximum rises. This can be seen at Fig. 1.5(a). At values $T<0.1E_C$ the dips increase with temperature but the peak value does not change and keeps its value of $G=\frac{1}{2}\frac{G_L G_R}{G_L+G_R}$. On the other hand, when $T>0.1\cdot E_C$ the peaks increase with temperature and at $T>0.4E_C$ the CB oscillations are not visible anymore.

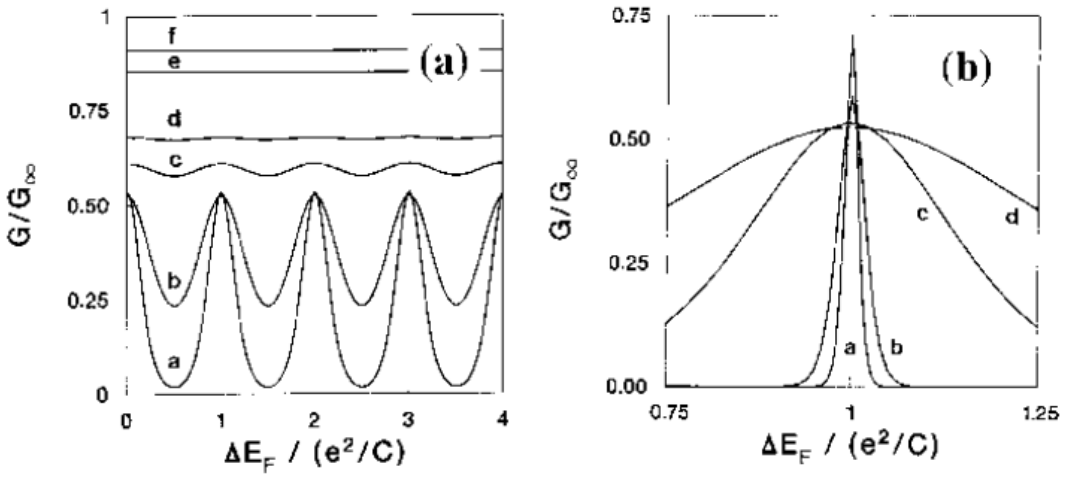

Figure 1.5: Calculated conductance peaks at different values of temperatures in the classical regime (Orthodox theory) **(a)** and in the quantum regime **(b).** In **(a)** the parameters are: $\Delta = 0.01E_C$ and $\frac{k_\beta T}{E_C} =$ 0.075[a], 0.15[b], 0.3[c], 0.4[d], 1[e], and 2[f]. In **(b)** the parameters are $\Delta = 0.01E_C$ and $\frac{k_\beta T}{\Delta} =$ 0.5[a], 1[b], 7.5[c], and 15[d].

In the quantum regime the line shape of a conductance peak depends on the relation between the thermal energy $k_B T$ and the level broadening $h\Gamma$. If $\hbar\Gamma << kT << \Delta$, only a single thermally broadened resonance contributes to the conductance. The shape of the conductance peaks obtains the form:

$$\frac{G}{G_{\max}} = \cosh^{-2}\left(\frac{\Delta E}{2kT}\right) \qquad \Delta E = E_0 - e\frac{C_g}{C}V_g \tag{1.4.10}$$

Here ΔE is the distance from the conductance peak. The peak height is:

$$G_{\max} = \frac{e^2}{4kT}\frac{\Gamma_L\Gamma_R}{\Gamma_L + \Gamma_R} \tag{1.4.11}$$

In this case, the peak height increased when the temperature decreased. This is shown in Fig. 1.5b.

If $kT << \hbar\Gamma << \Delta$ the transmission probability for non-interacting electrons has Breit-Wigner form:

$$G_{BW} = \frac{e^2}{\hbar}\frac{\Gamma_L\Gamma_R}{\Gamma_L + \Gamma_R}\frac{\Gamma}{(\varepsilon/\hbar)^2 + (\Gamma/2)^2} \tag{1.4.12}$$

ε is the energy separation of that level from the Fermi level in the reservoirs. The Breit-Wigner formula implies for a saturation of the peak height at a value which is at most $\frac{e^2}{h}$.

1.4.1.3 Bias voltage dependence

In the previous section we focused on the zero-bias conductance, namely conductance in the limit of very small bias between the source and drain leads. In this section we describe the conductance behavior as a function of the bias voltage.

When the QD potential is tuned to the fully blockaded state, midway between conductance peaks, no current flows in the neighborhood of zero bias, $V_{sd} \approx 0$. This suppression of current in the $I - V_{sd}$ curve can be observed in Fig. 1.7. It arises from the fact that away from charge degeneracy points, there is a finite charging energy required to place an additional electron on a QD. At low temperatures, current begins to flow only when V_{sd} is sufficiently large to supply this charging energy. This defines threshold energy, V_{th}, above which current can flow in the system.

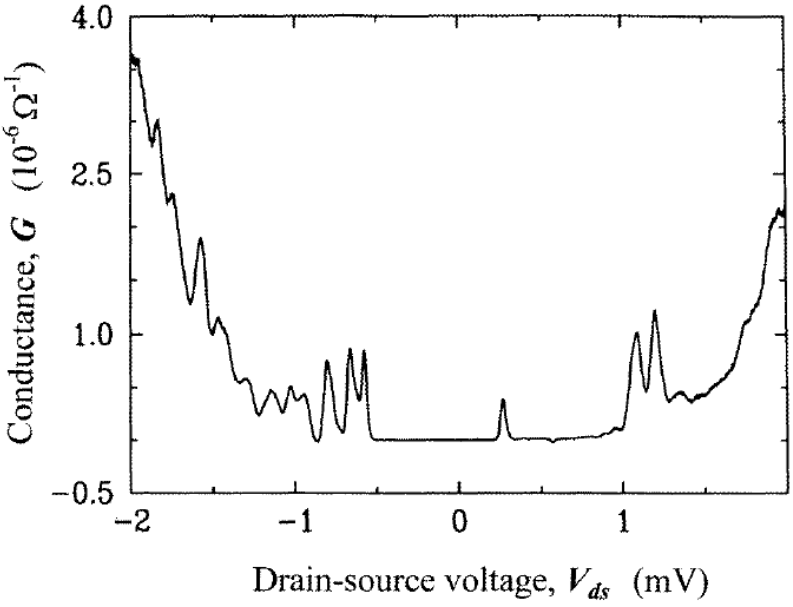

Figure 1.6: The differential conductance $G = \frac{dI}{dV_{sd}}$ as a function of V_{sd} measured in the quantum regime. The peaks are associated with the excited electron states in the QD, appearing whenever such an excitation is aligned with the Fermi level of one of the leads.

The current voltage characteristics above the threshold energy in the classical and quantum regimes are different. Since in the classical regime many electron levels participate in transport in the window of $k_B T$ the energy spectra is continuous. Hence, when the bias voltage is increased the current obeys the Ohmic law as in a metal, as shown in Fig. 1.7. In the quantum regime the situation is different. Once an electron populates the first level in the dot, the current is kept constant until the next level enters the window of $e \cdot V_{sd}$. At this stage, a jump in the current occurs since the electrons can tunnel through additional level in the dot. Whenever an additional level enters the window of $e \cdot V_{sd}$, the current jumps. Hence, the $\frac{dI}{dV_{sd}}$ versus V_{sd} curve in the quantum regime manifests the quantum spectrum of a QD. An example of such a curve is shown in Fig. 1.6.

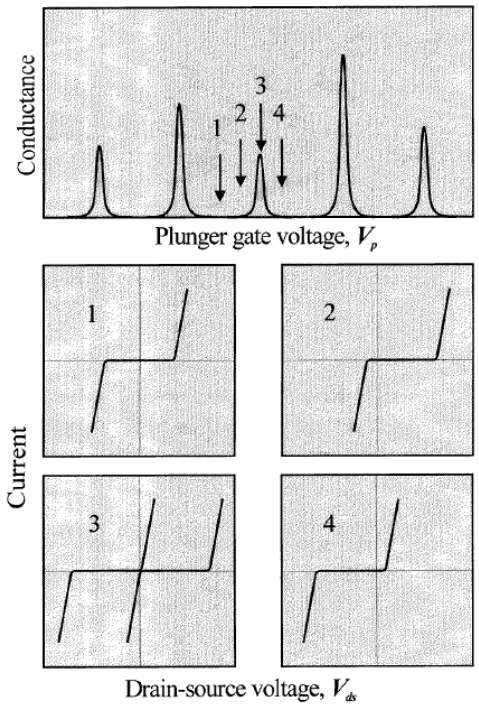

Figure 1.7: The current versus V_{sd} in a QD as a function of the gate voltage, V_g. Schematic $I - V_{sd}$ traces corresponding to different values of V_g show how the $I - V_{sd}$ curve shifts as V_g is increased.

The change in the $I - V_{sd}$ curve as the gate voltage V_g is swept is illustrated schematically in Fig. 1.7. If we ignore the capacitance between the dot and the drain lead, the $I - V_{sd}$ curve simply shifts with V_g while essentially preserving its shape. This is a direct result of the fact that the threshold energy to add (remove) an electron from the QD is reduced (increased) proportionally to the

positive shift in the electrostatic potential. Among other things, this implies that the $I-V_{sd}$ curve is highly asymmetric for all but two points in any gate voltage cycle. Interestingly, the total gap $\frac{e}{C}$ between positive threshold and negative threshold is preserved. Right at the conductance peak, the $I-V_{sd}$ curve nominally fluctuates between two curves corresponding to the two degenerate charge states of the QD: one shifted to the left, and other to the right[8]. Shifting further the gate voltage results in periodic behavior of the $I-V_{sd}$ curve.

The Coulomb Staircase (CS)

A particularly striking example of how single-electron charging can affect the $I-V_{sd}$ characteristics of a QD occurs when one tunnel barriers is significantly more transmitting than the other tunnel barrier. In this case the $I-V_{sd}$ curve exhibits what has been referred to as CS[9,10], namely a stepwise curve as seen in Fig. 1.8.

The most important point to make is that unlike the Coulomb suppression of current in the neighborhood of $V_{sd} \approx 0$, the staircase is not a universal feature of the CB. Rather, it is a special result of having very different tunneling rate through the two tunneling barriers. For simplicity, the lead with the more transparent tunnel barrier will be referred to as the drain. The Coulomb-blockade staircase arises in the following way. As V_{sd} is increased, eventually it becomes sufficiently large to overcome the Coulomb charging energy, and an electron rapidly tunnels into the QD through the drain barrier. The electron then dwells in the QD for a relatively long time, until it tunnels out through the more opaque source barrier. Tunneling out to the source is the rate-limiting step in transport through the QD, and the tunneling rate in this step is affected only by the potential difference between the QD and the source. This potential difference is equal to the charging energy plus the fraction of V_{sd} that falls across the source barrier which is $\Delta V_{source} = (\frac{C_d}{C}) \cdot V_{sd}$, where $C = C_d + C_s$ and C_d / C_s is the capacitance between the QD and the drain/source. Very interesting is to examine the case where $C_d << C_s$. In this case $\frac{C_d}{C}$ is sufficiently small, hence the potential difference driving the rate-limiting case is primarily determined by the charge state of the QD and it is nearly independent of V_{sd}. In other words, since $\frac{C_d}{C}$ is very small, the voltage mostly drops in the "wrong" place, the drain, and one fails to increase the voltage drop in the source barrier. Consequently, the electron cannot tunnel out to the more opaque barrier and current cannot flow till the charging energy is supplied. This is the

origin of the first plateau in the Coulomb-blockade staircase. The next step in which two electrons pass through the dot is blocked again and the second electron cannot tunnel out to the source since the voltage drop on it is very small. Hence, in this case, the current is voltage independent until a jump in the current is observed when additional amount of charging energy is supplied implying that the second electron succeeds to tunnel out to the source barrier. Successive plateaux are repeatedly arrived at as V_{sd} becomes large enough to charge the QD with incrementally more electrons, with commensurate increase in the dot-to-source potential drop.

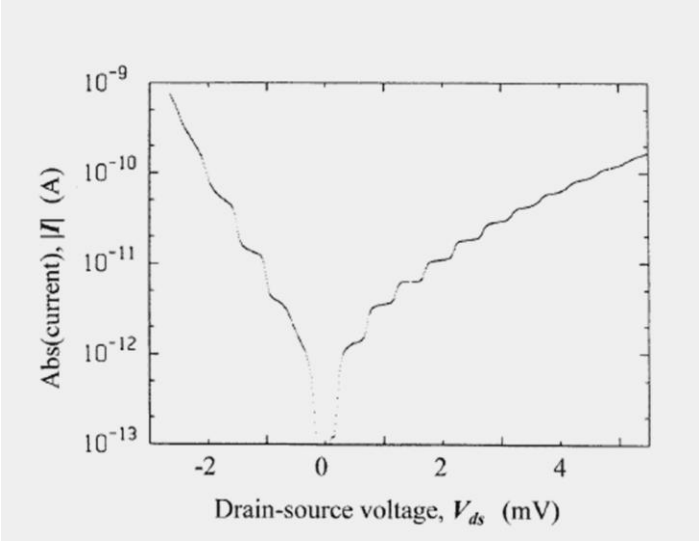

Figure 1.8: An experimental demonstration of the CS in a QD. The current, I, as a function of the bias, V_{sd}, between the leads shows a staircase behavior.

1.4.1.4 Charge stability diagrams and Coulomb diamonds

After considering the conductance dependence both on the gate voltage and bias voltage, we would like to show the charge configuration of a QD as a function of potential shifts due to the gate voltage and bias voltage. This is called charge stability diagram of a QD. The following description refers to the quantum regime although it is relevant also to the classical regime while neglecting the single-particles energies.

The total energy of the island is given by the sum of its single-particle energies, ε_i, plus the electrostatic energy $U(N)$:

$$E(N)=\sum_{i=1}^{N}\varepsilon_i+U(N)=\sum_{i=1}^{N}\varepsilon_i+\frac{e^2N^2}{2C}+eN\cdot\left(\frac{Q_{bg}}{C}+\frac{C_1}{C}\cdot V_1+\frac{C_2}{C}\cdot V_2+\frac{C_G}{C}\cdot V_G\right) \quad (1.4.13)$$

N is the number of electrons already in the dot, Q_{bg} is the charge that remains on the dot if all potentials are put to zero, C_1 and C_2 are the capacitances between the dot and the drain and source respectively, V_1 and V_2 are the voltage drops on the drain and source respectively and C is the total capacitance of the system.

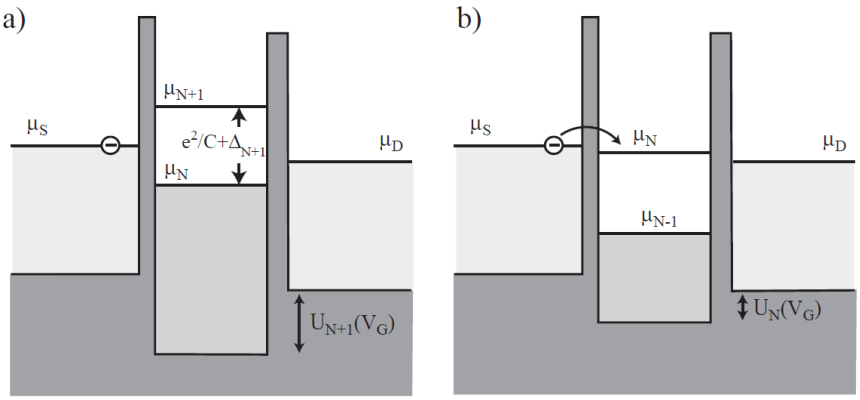

Figure 1.9: Energy diagram for a QD. The two tunnel barriers connect the dot to the source and drain contacts. **a)** Here, transport is blocked and the dot contains a fixed number of N electrons. **b)** The gate voltage was tuned in order to align the chemical potential in the dot with that of source and drain. In this situation the number of electrons on the dot can fluctuate between N-1 and N giving rise to a peak in the conductance.

Here, the electrochemical potential, μ_N, is defined as the energy required to add the N_{th} electron to a conductor and is defined as:

(1.4.14) $$\mu_N = E(N) - E(N-1) = \varepsilon_N + \frac{e^2}{C}\cdot(N-\frac{1}{2}) + e\cdot(\frac{Q_{bg}}{C} + \frac{C_1}{C}\cdot V_1 + \frac{C_2}{C}\cdot V_2 + \frac{C_G}{C}\cdot V_G)$$

Here we assume that the bias is applied symmetrically to the source and drain contacts which means $\mu_S = \mu_0 + \frac{eV_{sd}}{2}$ and $\mu_D = \mu_0 - \frac{eV_{sd}}{2}$ where μ_S and μ_D are the electrochemical potential in both contacts when a bias voltage is applied and μ_0 is the electrochemical potential in both contacts without an additional bias voltage.

This now leads to a set of requirements for the situation where a configuration with N electrons on the dot is stable.

For $V_{sd} > 0$ the requirements are (see Fig. 1.9):

(1.4.15)
$$\mu_N < \mu_0 - \frac{eV_{sd}}{2}$$

$$\mu_{N+1} > \mu_0 + \frac{eV_{sd}}{2}$$

For $V_{sd} < 0$ the requirements are: $\mu_N < \mu_0 + \frac{eV_{sd}}{2}$

$$\mu_{N+1} < \mu_0 - \frac{eV_{sd}}{2}$$

This inequalities lead to border-line equations describing the line where the Coulomb-blockade is lifted at the edge of the diamond shaped region. Using the expression for μ_N (Eq. (1.4.14)) one can find that for $V_{sd} > 0$ the border-lines are the following:

(1.4.16) $$V_G = \frac{1}{\alpha_G}[\varepsilon_N + E_C(N - \frac{1}{2}) - \mu_0 + e \cdot (1 - \alpha_S + \alpha_D) \cdot \frac{V_{sd}}{2} - e \cdot \alpha_G \cdot V_G + \frac{e \cdot Q_{bg}}{C}]$$

(1.4.17) $$V_G = \frac{1}{\alpha_G}[\varepsilon_{N+1} + E_C(N + \frac{1}{2}) - \mu_0 - e \cdot (1 + \alpha_S - \alpha_D) \cdot \frac{V_{sd}}{2} - e \cdot \alpha_G \cdot V_G + \frac{e \cdot Q_{bg}}{C}]$$

Here, $\alpha_S \equiv \frac{C_S}{C}$ and $\alpha_D \equiv \frac{C_D}{C}$ are the lever arms of the source and drain contacts and $\alpha_G \equiv \frac{C_G}{C}$ is the lever arm of the gate electrode. If the dot is symmetric, e.g. the tunnel barriers have the same geometry, then $\alpha_S = \alpha_D$ and the border lines have exactly the opposite slope $\pm \frac{1}{2\alpha_G}$. The two lines cross at $eV_{sd} = \Delta_{N+1} + \frac{e^2}{C}$ where Δ_{N+1} is the energy level spacing, $\varepsilon_{N+1} - \varepsilon_N$. This value defines the extent of the diamond. The separation between two CB peaks which corresponds to the value of $V_G(N+1) - V_G(N)$ is $\frac{1}{\alpha_G}(\Delta_{N+1} + \frac{e^2}{C_\Sigma})$. Therefore one can compare the extent of the diamond with the separation between the peaks and evaluate the lever arm α_G. Furthermore it turns out

that the difference between the slopes of the two border-lines is $\frac{1}{\alpha_G}$ irrespective of the levers arms of source and drain. The situation is shown in detail in Fig. (1.10a).

.

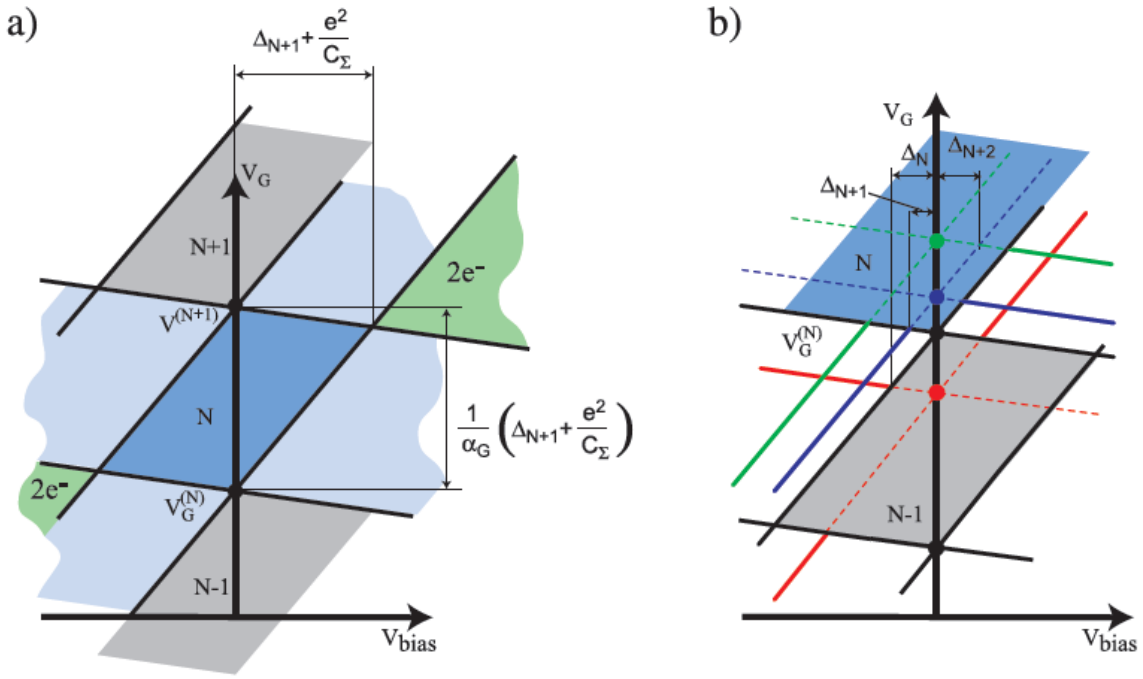

Figure 1.10: (a) CB diamonds. The current is blocked in the diamond shaped areas shaded in grey and dark blue. In these areas the number of electrons in the dot, N, is constant. Conductance peaks occur on the V_G-axis at points where neighboring diamonds touch (black dots). **(b)** Excited states move as lines parallel to the borderlines in the regions where the current is not blocked.

In the central diamond (dark blue region) the probability of finding N electrons on the QD is unity and the dot is a stable N-electron configuration. The light blue diamonds extending from the coulomb peaks (black dots) denote the regions where the probability for finding N electrons on the dot is between 0 and 1 and the electron number can fluctuate by one. Further away from the gate axis (green areas), the large bias $eV_{sd} > \frac{e^2}{C}$ allows for two electrons to tunnel at the same time. In a measurement of the differential conductance $\frac{dI}{dV}$ as a function of bias voltage V_{sd} and gate voltage V_G the borderlines will show up as peaks since this is where the current through the dot changes and a new transport channel opens/closes (see Fig. 1.10b).

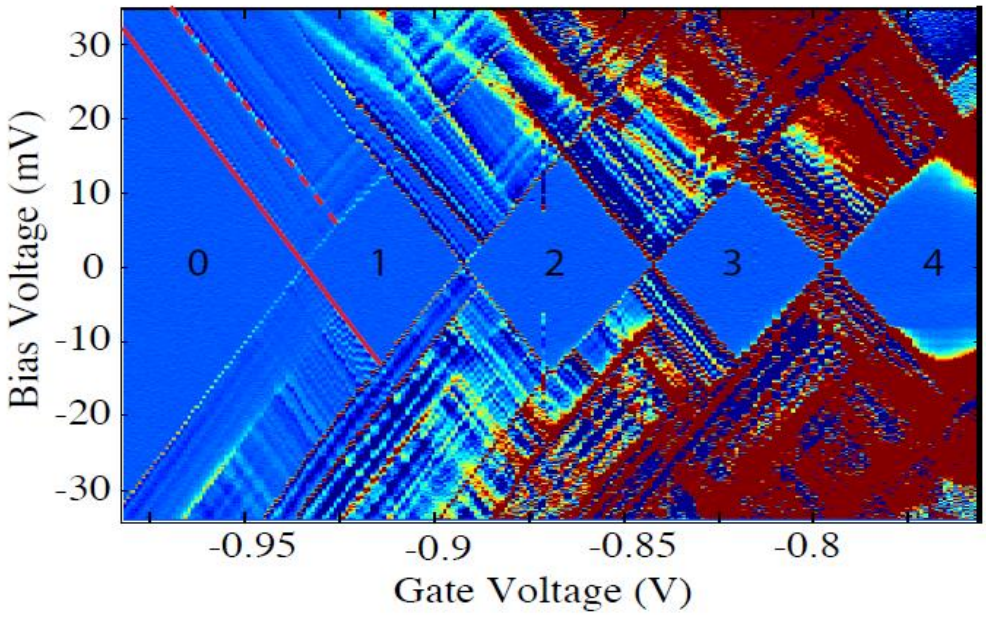

Figure 1.11: Measurement of CB diamonds in the differential conductance through a QD. Blue (red) indicate regions of low (high) differential conductance (dI/dV) respectively. The arrows at the top of the figure show how the levels are being filled with spins.

In the above discussion we assumed that only a single level ε_N contributes to the transport through the dot. This is not true for $eV_{sd} > \Delta_{N+1}$. In this case additional single-particle levels become accessible within the bounds given by the bias voltage and lead to an increase of the current through the dot and to additional boundary lines in the differential conductance. This is shown in Fig. 1.4.8b where for each coulomb peak additional lines occur outside the blockade diamonds. In real dots with many electrons there are also more complex collective excitations that have to be considered. In addition not all processes have the same amplitude which means that some of the lines in the diamonds are suppressed. Charge stability diagram of a real dot is shown in Fig. 1.11. The differential conductance is plotted on a logarithmic color scale in order to bring out the excited states more clearly.

1.4.1.5 Physical conditions for observing the CB phenomenon

Implicit in the Orthodox formulation of the CB model in the weak coupling regime is the condition that the number of electrons localized in the dot, N, is a well-defined integer. This is to say, well-defined in the classical sense, as opposed to a quantum definition which describes N in terms of an average value $< N >$, which is not necessarily an integer, and time-averaged fluctuations $< \delta N^2 >$. The CB theory requires $< \delta N^2 > << 1$. Under this condition the time that an electron

resides on the dot, τ , is much greater than $\delta\tau$, the quantum uncertainty in this time. The current I cannot exceed $\frac{e}{\tau}$ since (for moderate bias) no more than one extra electron resides on the dot at any instant. The energy uncertainty for an electron, δE , is not larger than the applied voltage, hence, the condition that $\delta\tau << \tau$ translates into macroscopic variables using $I < \frac{e}{\tau}$, $\delta\tau \cdot \delta E > h$, and $\delta E < eV_{sd}$. After algebraic manipulations the minimum tunneling resistance above which the CB theory is applicable is[11],

$$R >> \frac{h}{e^2} \qquad (1.4.18)$$

To be able to resolve the charge quantization in the QD, the charging energy has to be larger than the thermal energy:

$$E_C >> k_B T \qquad (1.4.19)$$

In order to observe the energy levels quantization in the QD, one has to measure in the quantum regime:

$$\Delta >> k_B T \qquad (1.4.20)$$

1.4.1.6 Higher order processes

There are two different mechanisms of low-temperature ($k_B T << \frac{e^2}{C}$) conductance. One contribution is due to real transitions of electrons between the leads and the dot. In the closed-dot regime the sequential single-electron tunneling is the most dominant process in transport, this is the first order correction in the perturbation theory[12,13], given by Eq. 1.2.3.

At low temperatures another mechanism of transport through the dot contributes. This mechanism, commonly referred to as the inelastic co-tunneling, corresponds to the second-order tunneling processes. The co-tunneling mechanism gives only a small correction to the peak value, however it dominates away from peaks as $T \to 0$. High order processes in transport dominate the conductance either when the temperature is very low or the coupling becomes strong. If sequential single electron is suppressed by the CB, higher order processes such as coherent "cotunneling" through several junctions become crucial. One of the cotunneling processes is the inelastic cotunneling in which two different electrons tunnel in the two junctions. One jumps into the

central electrode above its Fermi levels, and another jumps out of the electrode from below the level. In this case the state with an excess electron charge in the island exists only virtually. As a result of such a two-step process, one electron is transferred from the left lead to the right one and the charge of the QD is left unchanged. This tunneling process can be described without any coherence between two tunneling events in the two junctions. Such a tunneling involves a creation of an electron-hole excitation on the QD, and thus can be called inelastic. There are actually two channels which add coherently, meaning two options for this process. One option is that an electron tunnels first from the left lead onto the island, and then another electron tunnels from the island to the other lead. In this case the increase in charging energy of the intermediate state (ε_2) compared with the initial one (ε_1) is $\delta E_L = U(n+1) - U(n) - eV_L + \varepsilon_2 - \varepsilon_1$. Another option is that an electron tunnels first out of the island to the right lead and another electron from the left lead replaces the charge. In this case the increase in energy of the intermediate state is $\delta E_R = U(n-1) - U(n) + eV_R + \varepsilon_4 - \varepsilon_3$. At finite temperature and in the case $eV_{sd} << \delta E_L, \delta E_R$, one can calculate the tunneling rate and obtain:

(1.4.21) $$\Gamma = \frac{\hbar G_L G_R}{12\pi e}\left(\frac{1}{\delta E_L} + \frac{1}{\delta E_R}\right)^2 \left[\left(eV_{sd}\right)^2 + (2\pi k_B T)^2\right] \cdot V_{sd}$$

The corresponding conductance has only a power-law dependence on temperature:

(1.4.22) $$G = \frac{\pi\hbar G_L G_R}{3e^2}\left(\frac{T}{\Delta E}\right)^2 \qquad \Delta E = V_g - V_g\left(N = \frac{1}{2}\right)$$

Here ΔE is the distance from the conductance peak. This formula is valid only in the regime $T << \Delta E$.

At very low temperatures the tails of the peaks (dips) are dominated by the co-tunneling contribution given by Eq. (1.4.22) whereas the conductance near the peaks is dominated by the sequential contribution, given by Eq. (1.4.10).

1.4.2 Transport properties of a QD in the strong coupling regime

In this section we focus on the strong coupling regime where the conductance through the barriers is not so small compared to the conductance quantum $G_0 = \frac{e^2}{\hbar}$. This regime is known as the open-dot regime and characterized by strong fluctuations of the charge. In our research we studied the conductance of QDs in the strong coupling regime, and thus this regime is main focus in this

work. As was mentioned above, the single electron effects showing well-separated conductance peaks as a function of gate voltage are best visible when the conductivity of the tunnel junction is much smaller than the quantum of conductance. If the conductance of tunnel junctions is not so small the energy levels overlap and the concept of tunneling via discrete charge states becomes ill defined, raising the question of whether charging effects survive under such conditions or whether they are washed out completely by strong quantum fluctuations. Recent experimental and theoretical works[14,15,16,17,18,19,20,21,22] indicate that if the transmission coefficient is close to 1 the conductance shows periodic oscillations, although the peaks are not well separated. These altogether works show that quantum fluctuations of the charge do not destroy the CB of tunneling and the ground state energy retains the periodic dependence which represents the CB. However, the quantum fluctuations lead to a strong renormalization of the effective junction capacitance $C_{eff} \approx C\exp(\frac{\alpha}{R})$ where R is the tunneling resistance. Hence, the effective charging energy that is the charge dependent part of the ground state energy is suppressed and is given by:

$$E_{C_{eff}} = E_C \exp(-\frac{\alpha}{R}) \qquad (1.4.23)$$

There is a partial controversy as to the value of α, however, all of theoretical works agree that the amplitude has exponential decay with increasing coupling and charging energy vanishes only for perfect point contacts.

It is interesting to study the behavior of the CB conductance peaks as a function of the gate voltage. The theoretical results predict that the difference between the peaks and valleys becomes less pronounced and eventually instead of the peak structure, one observes only a weak periodic modulation. Assuming the transmission coefficients of the two contacts are close to unity, one can treat the system with an Hamiltonian of perfect transmission and then construct the perturbation theory with small reflection amplitudes, r_L and r_R. At low temperatures $T << E_c$ the conductance is given by:

$$G = \frac{e^2}{4\pi\hbar}\left(1 - \frac{\pi\Gamma_0(N)}{4T}\right), \qquad \Gamma_0(N) = \frac{2\gamma E_c}{\pi^2}\left[|r_L|^2 + |r_R|^2 + 2|r_L||r_R|\cos(2\pi N)\right] \qquad (1.4.24)$$

Here $\gamma = e^c$ with $C \sim 0.5772...$being the Euler's constant. This formula is valid only if $T >> \Gamma_0$.

Eq. (1.4.24) shows that strong tunneling (or weak scattering in the contacts) gives rise to a small **periodic** correction to the conductance. The same behavior was predicted for the average charge of the dot. However, unlike the average charge, the correction to conductance strongly depends on temperature. As the temperature is lowered, the conductance decreases linearly.

In the very low temperature limit, where $T << \Gamma_0$, the conductance is quadratic in temperature,

$$G = \frac{\pi e^2}{12\hbar}\left[\frac{T}{\Gamma_0(N)}\right]^2 \qquad (1.4.25)$$

Eq. (1.4.25) is invalid for the case of symmetric barriers on resonance, since when $|r_L| = |r_R|$ $\Gamma_0 \to 0$, and the formula is never achieved. In this case the conductance behaves according to Eq. (1.4.24) and the resonant value is $\frac{e^2}{4\pi\hbar}$, whereas away from the resonance the conductance has quadratic temperature dependence. An example of such conductance curve is shown in Fig. 1.12.

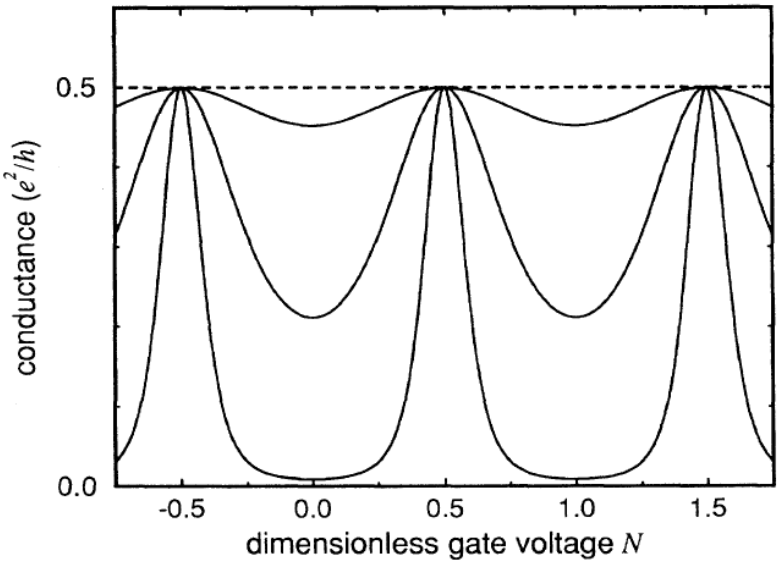

Figure 1.12: Calculated conductance curves as a function of dimensionless gate voltage (or N, the number of electrons in the QD) when the dot is symmetrically coupled to the leads. The three curves are calculated for E_C/T = 1, 10 and 100.

1.4.2.1 Interference effects in open dots

Mesoscopic transport in diffusively scattering metals has been studied much in the past[2324]. It is well known in these systems that interference of forward-scattered electron waves traveling by different paths causes time-independent conductance fluctuations and interference of time-reversed pairs of backscattered electron waves leads to a weak localization. Quantum interference between alternative trajectories linking entry and exit openings of open dots determines the quantum mechanical transmission and hence the conductance through the dot. At low temperatures, the magnetoconductance of circular and stadium-shaped QDs with quantum point contacts show conductance fluctuations due to the interference of electron waves traveling between the contacts by different paths[25], and a coherent backscattering peak at zero magnetic field due to the interference of time-reversed pairs of backscattered trajectories[26,27,28]. Quantum interference phenomena in ballistic microstructures are produced by scattering from the walls of the device rather than by randomly located impurities and are thus inherently shape dependent. For example, a circular billiard differs from a stadium in that an ideal circle has integrable trajectories that conserve angular momentum, while an ideal stadium produces chaos.

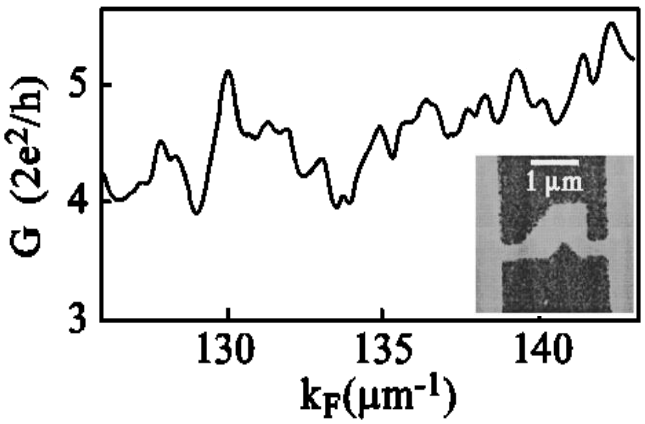

Fig 1.13: Conductance fluctuations as a function of the Fermi momentum of a ballistic open dot at zero magnetic field, measured by Keller et al[29].

Interference effects in the conductance can be observed by changing a phase-sensitive parameter in the system, for example external magnetic field or the electron's Fermi momentum, k_F. By sweeping V_g one can change the phase difference between the electronic trajectories via $\Delta k_F \cdot l$. Here l is the path length difference between a couple of electronic trajectories dominating the transport through the dot. Many groups have measured the conductance through ballistic open dots[24-27]. One example is conductance measurement of ballistic open cavity studied by Keller et al.[27], shown in Fig. 1.13. They measured the conductance as a function of the Fermi momentum and observed aperiodic but reproducible fluctuations.

1.5 Varieties of QDs

The confinement of electrons in a small region can be obtained in several different ways and, in addition, the QD itself can have a peculiar arrangement with respect to its surrounding: it can be embedded into a matrix or grown onto a substrate or it can be a "free" nanoparticle. Different techniques lead to different topologies of QDs[30]. In this section we will give a short survey of the two most popular types of QDs: Two dimensional electron gas (2DEG) in lithography defined nanostructures (section (1.5.1)) and colloidal QDs (section (1.5.2)).

1.5.1 Lithographically Defined QDs

Lithographically defined QDs are formed by isolating a small region of a two-dimensional electron system via tunneling barriers from its environment. Such two-dimensional electron system or 2DEG can be found in metal-oxide-semiconductor field effect transistors (MOSFET) or in the so-called semiconductor heterostructures. Heterostructures are composed of several thin layers of different semiconductor materials grown on top of each other as shown in Fig. 1.14. The layer sequence can be chosen in such a way that all free charge carriers are confined to a thin slice of the crystal forming essentially a two-dimensional electron system. A superstructure derived from the periodic repetition of this sequence of layers is also called a "multiple quantum well".

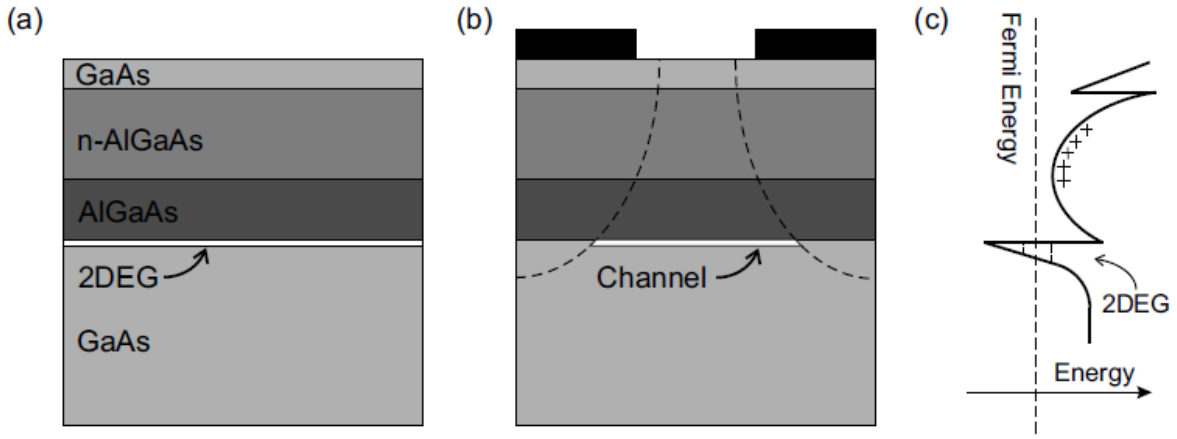

Figure 1.14: **(a)** Semiconductor heterostructure containing a 2DEG. **(b)** Electrons can be confined by applying negative voltages to gates on top of the wafer surface. The underlying 2DEG can then be fully depleted. **(c)** Energy band diagram for the conduction band of the heterostructure.

One of the most widely investigated systems is aluminum gallium arsenide/gallium arsenide (AlGaAs/GaAs) quantum well. AlGaAs has the same lattice constant as GaAs but a wider band gap whose exact value depends on the aluminum content of the layer. Under these conditions a dip in the conduction band at the interface is created and the electrons in the GaAs layer are confined to this layer and form a 2DEG.

In semiconductor heterostructures the 2DEG is locally electrostatically depleted by applying negative voltages to electrodes deposited on top of the crystal, called back gate electrodes. When a negative voltage is applied to the metal back gate electrodes above the 2DEG, due to electrostatic repulsion, electrons are repelled by the electric field of the electrodes and the region of the 2DEG below the electrodes is depleted of electrons. A charge-depleted region behaves like an insulator. Therefore by applying an electric field on metal electrodes with an appropriate shape it is possible to create an island of charges insulated from the rest of the 2DEG which serves as the source and drain electrodes. If the island within the 2DEG is small enough, it behaves as a QD. An example of such a QD is shown in Fig. 1.15.

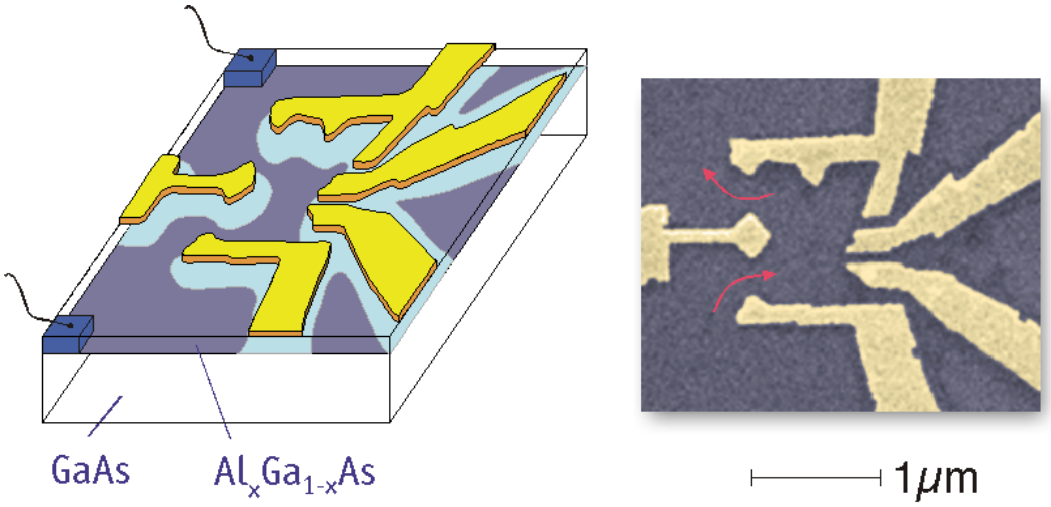

Figure 1.15: A typical micro-scale QD schematically on the left and actual electron micrograph on the right.

A remarkable advantage of lithographically defined QDs is that their electrical connection to the "macro-world" is straightforward. The technique of applying shaped back gate voltages in used to vary easily the opening between the dot and the leads. The degree of coupling can be tuned by applying specifically shaped back gate voltages on top of the hetreostructure. However, as the geometry of these QD is determined lithographically, it is limited to the usual size and resolution limits of lithographic techniques. Even by using electron beam lithography for the fabrication of the

QD, it is not possible to tailor their size with nanometer precision. Moreover, the distance of the gates to the 2DEG limits the size of the QD even more. Lithographically fabricated QDs are typically larger than 10 nm, and therefore only relatively low lateral confining energies can be achieved.

1.5.2 Colloidal QDs

Colloidal QDs are different from QDs formed by the systems mentioned above, as they are chemically synthesized using wet chemistry and are free-standing nanoparticles or nanocrystals grown in solution. In the fabrication of colloidal nanocrystals, the reaction chamber contains a liquid mixture of compounds that control the nucleation and the growth[31]. In a general synthesis of QDs in solution, each of the atomic species that are part of the nanocrystals is introduced into the reactor in the form of a precursor. A precursor is a molecule or a complex containing one or more atomic species required for growing the nanocrystals. Once the precursors are introduced into the reaction flask they decompose forming new reactive species (the monomers) that cause the nucleation and growth of nanocrystals. The energy required to decompose the precursors is provided by the liquid in the reactor, either by thermal collisions or by a chemical reaction between the liquid medium and the precursors, or by a combination of these two mechanisms.

A key parameter in the controlled growth of colloidal nanocrystals is the presence of one or more molecular species in the reactor, broadly termed “surfactants”. A surfactant is a molecule that is dynamically adsorbed to the surface of the growing QD under the reaction conditions. It must be mobile enough to provide access for the addition of monomer units, while stable enough to prevent the aggregation of nanocrystals. The choice of surfactants varies from case to case: a molecule that binds too strongly to the surface of the QD is not suitable, as it would not allow the nanocrystal to grow. On the other hand a weakly coordinating molecule would yield large particles or aggregates. Some examples of suitable surfactants include, for instance, alkyl thiols, phosphines, phosphine oxides, phosphates, phosphonates, amides or amines and carboxylic acid. Colloidal QDs can be either metallic or semiconductor. Their size could be as small as few nanometers.

In contrast to lithographically defined semiconductor QDs, electrically connecting a colloid to external leads is not a trivial task. There are two technical challenges. One is fabricating two electrodes separated by a spacing of a few nm and the second is stably bridging this gap by the conducting colloid. In recent years there have been few techniques that have been used to achieve this goal but none of them provide perfect solutions. The success rate for producing this device is relatively low. Moreover, there has been no technique, analogous to the one applied to lithography

defined semiconductor QD, for altering the coupling strength between the colloid and the external lead. This will be a major focus of this thesis.

There are clear differences between metallic colloidal QDs and lithography defined semiconductor QDs. A typical diameter of a metallic QD is 5-30 nm and contains 10^3 to 10^5 electrons leading to very small Δ which could be few μV. Since a metallic QD can be prepared to be very small, its charging energy could be very large. For instance, for a gold colloid having diameter of 10 nm, the energy-level spacing is about 5 μV and it's charging energy is about 30 meV. Due to very small value of energy level spacing in metallic QD the most achievable regime is the classical regime, and one needs Dilution refrigerator temperatures to reach the quantum regime. Moreover due to the technical difficulty to control its coupling to external leads, the realistic experimental regime is the weak coupling regime.
The situation is different in lithography defined semiconductor QDs. Resonant tunneling studies in these systems have demonstrated energy-level spacing $\Delta \geq 0.1\, meV$ while the charging energy is $E_C \leq 1meV$. Hence, one can easily achieve the quantum regime. Furthermore, in these QDs one can vary easily the opening between the dot and the leads and the strong coupling regime is easily achievable.

1.6 ZBA in low dimensional systems

Electron-electron interactions have a dramatic influence on the electronic properties of low dimensional systems. Since the dawn of the solid state physics it is customary to identify two distinct contributions of interactions in solids: The Exchange and Hartree terms. All phenomana related to the CB model discussed in the previous sections are in fact a manifestation of the Hartree term. This term dominates when the single electron tunneling processes are very strong and hence in this case only the number of electrons in the dot plays a role and quantum processes are not relevant. In the tunneling conductance the Exchange term manifests itself in the ZBA effect, a suppression of the tunneling DOS at the Fermi level. An example to ZBA is the tunneling into low dimensional weakly disordered metals which exhibits a pronounced ZBA phenomenon in two dimensional (2D) disordered metallic films[32] and 1D wires[33]. In the following we will review the ZBA anomaly in 2D systems (section (1.6.1)) and in zero dimensional (0D) systems (section (1.6.3)).

1.6.1 ZBA in 2D weakly disordered metals

The correction to the classic DOS for a 2D diffusive film exhibiting strong e-e interactions was calculated by Altshuler & Aronov[34]. In their work they predicted renormalization of the tunneling DOS by quantum processes resulting from e-e interactions in the dot, leading to suppression in the conductance at small energies. This suppression of the tunneling DOS is perturbative and applicable in a weakly metallic transport conductivity where the Drude model is relevent, meaning when $\upsilon_0 \cdot D >> 1$ where υ_0 is the energy states density and D is the diffusion constant. Moreover, this correction is applicable in the regime where $\varepsilon \cdot \tau << 1$, where ε is the energy of the conduction electrons and τ is the elastic scattering time. The correction is given by,

$$\delta\upsilon(\varepsilon, T) = -\frac{1}{8\pi^2 \hbar D} \ln\left(\frac{\max\{\varepsilon, T\}}{D^2 \kappa^4 \hbar \tau}\right) \cdot \ln\left(\frac{\tau}{\hbar} \max\{\varepsilon, T\}\right) \quad (1.6.1)$$

where $\kappa = 2\pi e^2 \upsilon_0$. These calculations predict that the amplitude of the conductance dip is inversely proportional to the dimensionless conductance of the disordered metal, g, where $g = \frac{hG}{e^2}$.

This expression can be written in this form:

$$\delta\upsilon(\varepsilon, T) = \frac{-1}{8\pi^2 \hbar D} \cdot [\ln^2(\max\{\varepsilon, T\} \cdot \tau) - \ln(D^2 \kappa^4 \hbar \tau^2) \cdot \ln(\max\{\varepsilon, T\} \cdot \tau)] \quad (1.6.2)$$

Since this is a perturbative treatment, this term is applicable only if $\frac{\delta\upsilon}{\upsilon_0} << 1$, meaning under the condition:

$$(1.6.3) \quad \frac{1}{8\pi^2 \upsilon_0 \hbar D} \cdot \ln^2(\max\{\varepsilon, T\} \cdot \tau) << 1$$

This leads to the regime of energy in which Altshuler & Aronov approach is applicable:

$$(1.6.4) \quad \tau^{-1} \exp(-\sqrt{8\pi^2 \hbar \upsilon_0 D}) \quad < \quad \varepsilon \quad < \quad \tau^{-1}$$

For energies which are smaller than the lower limit in the regime (1.6.4), the above correction is not applicable since the term $\frac{\delta\upsilon}{\upsilon_0}$ is not smaller than 1. In case where $\frac{\delta\upsilon}{\upsilon_0} << 1$ we can consider the term $\upsilon = \upsilon_0(1 - \frac{\delta\upsilon}{\upsilon_0})$ as a series expansion of the exponent function and rewrite the DOS by the term $\upsilon = \upsilon_0 \cdot \exp(-\frac{\delta\upsilon}{\upsilon_0})$.

Finkelstein[35]extended Altshuler & Aronov calculations for very small values of energies. Finkelstein claimed that the correction for the DOS can be formulated as a series expansion of exponent function. Hence, for $\varepsilon << \tau^{-1}$ the normalized correction to density of stated is:

$$(1.6.5) \quad \frac{\upsilon}{\upsilon_0} = \exp(-\frac{1}{8\pi^2 \upsilon_0 \hbar D} \cdot \ln(\frac{\max\{\varepsilon, T\}}{D^2 \kappa^4 \hbar \tau}) \cdot \ln\left(\frac{\tau}{\hbar} \cdot \max\{\varepsilon, T\}\right))$$

For small energies it can be written as:

$$(1.6.6) \quad \frac{\upsilon}{\upsilon_0} = \exp(-\frac{1}{8\pi^2 \upsilon_0 \hbar D} \cdot \ln^2(\max\{\varepsilon, T\} \cdot \tau))$$

1.6.2 ZBA in strongly coupled metallic QD

Golubev and Zaikin[36] described electron transport through metallic grains with CB effects beyond the perturbative regime. They proposed a theoretical approach which allows to obtain a quantitative description of electron transport through mesoscopic metallic grains in the strong

tunneling regime. They defined $\alpha_t \equiv \frac{R_K}{4\pi^2 R_t} = \frac{h}{4\pi^2 e^2 R_t}$ to be the dimensionless conductance of the tunnel junctions between the dot and the lead electrodes, where R_K is the quantum resistance and $\frac{1}{R_t} = \frac{1}{R_D} + \frac{1}{R_S}$ where R_D and R_S are the resistances between the dot and the drain (left) and source (right) leads respectively. In the limit of strong tunneling they reformulated the problem in terms of phase, which is canonically conjugated to the charge. When the fluctuations of the electronic tunneling current are strong, fluctuations of the conjugate phase variable φ are weak, and therefore the phase dynamics can be well described in terms of a quasiclassical Langevin equation for the phase variable φ with a state-dependent stochastic force[37,38]. They analyzed quantum dynamics of the phase variable in a semiclassical (saddle-point) approximation and obtained an expression for the system conductance valid for all values of the gate charge and at not too low temperatures $T \geq \frac{e^2}{2C_{eff}}$. The expression for the current is the following:

(1.6.7) $$I(V) = G_{as} \cdot V - I_0(V) - e^{-F(T,V)}[[I_1(V) - 2I_0(V)] \times \cos(\frac{2\pi Q_{av}(V)}{e}) + I_2(V)\sin(\frac{2\pi Q_{av}(V)}{e})]$$

Here, $G_{as} = \frac{1}{R_D + R_S}$ and $Q_{av} = \left\langle e(\hat{n} - n_g) \right\rangle_c = \frac{C_D R_D - C_S R_S}{R_D + R_S} \cdot V + C_g V_g$ is the average charge of the metallic dot and D and S denote the drain (left) and source (right) junction respectively.

(1.6.8) $$I_0(V) = \frac{2e}{\pi(R_S + R_D)} \int_0^\infty dt (\frac{\pi T}{\sinh(\pi T t)})^2 e^{-W(t,V)} K(t) \times \cos(\frac{e(R_S - R_D)Vt}{2(R_S + R_D)}) \sin(\frac{eVt}{2})$$

where $K(t) = R_t \theta(t)[1 - \exp(-t / R_t C)]$

(1.6.9)

$$I_1(V) = \frac{4e}{\pi(R_S + R_D)} \int_0^\infty dt \left(\frac{\pi T}{\sinh(\pi T t)} \right)^2 \times e^{-W(t,V)} [K(t)\cosh[u(t,V)] + 4\pi C \dot{K}(t)\sinh[u(t,V)]] \cos(\frac{e(R_S - R_D)Vt}{2(R_S + R_D)}) \times \sin(\frac{eVt}{2})$$

$$I_2(V) = \frac{4e}{\pi(R_S + R_D)} \int_0^\infty dt \left(\frac{\pi T}{\sinh(\pi T t)} \right)^2 \times e^{-W(t,V)} [K(t)\sinh[u(t,V)] + 4\pi C \dot{K}(t)\cosh[u(t,V)]] \sin(\frac{e(R_S - R_D)Vt}{2(R_S + R_D)}) \times \sin(\frac{eVt}{2})$$

where

(1.6.10) $$W(t,V) = -\frac{e^2}{2\pi}\int_{-\infty}^{\infty} dt_1 \int_{-\infty}^{\infty} dt_2 \left(\frac{\pi T}{\sinh(\pi T(t_1 - t_2))}\right)^2 \times K(t_1,t)K(t_2,t) \sum_{r=D,S} \frac{1}{R_r} \cos\left(\frac{eR_r V(t_1 - t_2)}{R_D + R_S}\right)$$

With $K(t^{'} - t) \equiv K(t^{'}) - K(t^{'} - t)$. The function $F(T,V) = 2\pi^2 \left\langle \delta n^2 \right\rangle$ determines the temperature and voltage dependence of the charge fluctuations. $F(T,V)$ is given by an expression similar to $W(t,V)$ with the substitution $K(t_1,t)K(t_2,t) \to (4\pi^2 C^2 / e^4)\dot{K}(t_1)\dot{K}(t_2)$. Analogously $u(t,V)$ is defined by Eq. (1.6.10) after the substitution $K(t_1,t) \to -(4\pi C^2 / e^2)\dot{K}(t_1)$.

In the limit of sufficiently high temperatures and/or voltages:

$\max\{eV,T\} >> \omega_0 = \frac{2\tilde{\alpha}_t E_C}{\pi^2} \cdot \exp(-2\tilde{\alpha}_t + \gamma)$, here $\gamma = 0.5772...$ is the Euler constant and $\tilde{\alpha}_t = \frac{h}{4e^2 R_t} = \pi^2 \alpha_t$, the above integrals can be evaluated analytically and get the form,

(1.6.11)

$$I_0(V) = \frac{eR_0}{R_L + R_R} \sum_{r=L,R} \left\{ \frac{eR_r V}{\pi(R_L + R_R)} \left[\mathrm{Re}\,\psi\left(1 + \frac{1}{2\pi T R_0 C} - i\frac{eR_r V}{2\pi T(R_L + R_R)}\right)\right] - \mathrm{Re}\,\psi\left(1 - i\frac{eR_r V}{2\pi T(R_L + R_R)}\right)\right\} - \frac{1}{\pi R_0 C} \sum_{r=R,L} \mathrm{Im}\,\psi\left(1 + \frac{1}{2\pi T R_0 C} - i\frac{eR_r V}{2\pi T(R_L + R_R)}\right)$$

(1.6.12)

$$F(T,V) = F(0,0) + \frac{2\pi^2 CT}{e^2} + \frac{2\pi}{e^2 R_0} \ln\left(\frac{1}{2\pi T R_0 C}\right) - \frac{2\pi}{e^2} \sum_{r=L,R} \mathrm{Re}\left[\frac{1}{R_L}\left(1 - i\frac{eR_r R_0 C}{R_L + R_R} V\right) \times \psi\left(1 + \frac{1}{2\pi T R_0 C} - i\frac{eR_r V}{2\pi T(R_L + R_R)}\right)\right]$$

Here $\psi(x) = \frac{\Gamma^{'}(x)}{\Gamma(x)}$ is the digamma function. $F(0,0)$ which determines the charge fluctuations at $T = 0$ and $V = 0$ can be calculated analytically[39] and gets the form $F(0,0) \approx 2\tilde{\alpha}_t$ where $\tilde{\alpha}_t \equiv \pi^2 \alpha_t$. The functions $I_1(V)$ and $I_2(V)$ cannot be evaluated analytically even in the limit above. Due to a fast decay of the exponential factor $\exp[-F(T,V)]$ in Eq. (1.6.7) with increasing V and T it is sufficient to evaluate I_1 and I_2 in the low-voltage and –temperature limit. In this limit the integrals above reduce to

(1.6.13) $I_1(V) - 2I_0(V) \approx gG_{as}V \qquad g = \frac{1.22}{\tilde{\alpha}_t} + 11.29$

whereas $I_2(V)$ turns out to be small at low voltages, $I_2(V) \sim V^2 \approx 0$.

Hence they arrive at the following result for the current characteristics of a SET transistor:

(1.6.14) $$I(V) = G_{as}V - I_0(V) - gG_{as}Ve^{-F(T,V)}\cos(\frac{2\pi Q_{av}(V)}{e})$$

The current is reduced below the classical result $G_{as}V$ by an amount $I_0(V)$ and is modulated in a periodic way by the gate voltage. The second term, $I_0(V)$, reflects a conductance dip at $V_{sd} = 0$ and is related to the ZBA effect. This term is pinned to the Fermi energy and is V_g independent. The last term is a pure $\cos$ modulation and describes the oscillatory behavior of the current as a function of the transport voltage and is associated with the CS. In contrast to the second term, this term is V_g dependent.

This result shows that electron interaction induced DOS suppression, known as ZBA, and the classic CB can co-exist in a strongly coupled 0D system. While the ZBA is a suppression of the tunneling conductivity at the Fermi level the CB effect is an oscillating feature which shifts with the gate voltage.

CHAPTER 2

AIM OF THE STUDY

The main goal of our research is to study electronic properties of a QD in a regime which was relatively unexplored up to now. To date, two extreme physical regimes were explored intensively, the weak coupling regime (closed dot regime) in which $\Gamma << \Delta$, and the strong coupling regime in which $\Gamma \geq \Delta$ (open dot regime). The crossover from closed to open dots has received much less attention. Our motivation is to focus on the crossover regime, or, in other words, covering the coupling regime from $\Gamma << \Delta$ to $\Gamma \geq \Delta$. This crossover between closed to open dots has inspired a lot of theoretical activity[40,41,42,43] but has not been studied much experimentally. The crossover regime is of special interest for many reasons. For instance, when the level broadening and the energy level spacing are at the same order of magnitude, interactions between different levels might occur. In this case the orthodox picture fails and a dynamical behavior of the occupations of the levels emerges.

The two extreme physical regimes are characterized by different transport properties. For a closed dot the main effect for electronic interactions is the classic CB which prevents tunneling conductivity except at the degeneracy point. The CB effect overshadows any other electron-electron contribution. In the case of asymmetric QD in which the dot is coupled more strongly to one of the leads than the other, the I-V curve exhibits a series of differential conductance plateaus termed the CS. For an open dot, CB effects are expected to be suppressed. Tunneling into a strongly coupled asymmetrically coupled QD (open dot) is expected to be similar to tunneling into a dirty metal which exhibits a suppression of the DOS at the Fermi level as a consequence of electron-electron interactions. Experimentally, this manifests itself as a dip in the tunneling conductivity at low bias known as zero bias anomaly (ZBA) effect. Moreover, open dots are expected to be dominated by mesoscopic quantum phenomena like universal conductance fluctuations (UCF) resulting from interference effects. What happens between these two extreme physical regimes? Can CB effects and mesoscopic effects (like ZBA) be observed simultaneously? Can both effects be separated in the intermediate coupling regime? In our study we will try to answer these questions.

Most studies on QDs were performed on low-density 2DEG, in which the degree of coupling could be controlled by applying specifically shaped back gate voltages to vary the opening between the dot and leads. However, applying gate voltages affects other properties such as the geometry of

the dot and the number of electronic channels coupled to the leads. Moreover, in lithography defined QDs in semiconductor hetreostructure the energy level spacing, Δ, is not much smaller than the charging energy, E_C ($\Delta \approx 0.1E_C$). Since the range between Δ and E_C is relative small, by increasing Γ through Δ one can easily lose the charging effects. For this reason we decided to use metallic colloid as QDs. We use 30nm gold colloids for which $\Delta \approx 10\mu V$ and $E_C = 25meV$. The many orders of magnitude separating Δ and E_C make it possible to achieve the condition $\Delta << k_B T << E_C$ and provides a large range for varying Γ through Δ while still keeping it much smaller than E_C.

Although the intermediate and strong coupling regime $\Delta \approx \Gamma < E_C$ is most achievable in metallic QDs, trapping a very small colloid in between two electrodes and controlling its coupling to the leads is not a trivial task. The technique of applying shaped back gate voltages to vary the opening between the dot and the leads is limited to low electron density semiconductor. Metals and heavily doped semiconductors that have a high charge carrier density are much less affected by accessible gate voltages. Despite the great incentive to study metallic systems, to date there has been no technique, analogous to the one applied for low density semiconductors, for altering the coupling strength between the outside world and a metallic dot. We are not aware of any existing technique with the capability of controlling the coupling between metallic QD and external leads. The major challenge in utilizing metallic nanoparticles as QDs is electrically connecting them to leads in a reliable way. In recent years there has been much advance in the field of "molecular electronics" in which the aim is to connect a single nano-object (a few nm large) to two large electric leads in order to enable driving electric current through the nano-element and to study the transport properties of the system or its electronic spectroscopy. This goal presents two major technical challenges. The first is to fabricate two electrodes separated by a spacing of a few nm and the second is to stably bridge this gap by a conducting nanoparticle or molecule. Some of the techniques that have been used to solve these problems are the following:

1. **Scanning Tunneling Microscope (STM)** - Using a STM tip as one electrode and measuring the I-V characteristics through a nanoparticle placed on a conductive layer acting as the second electrode[44,45].
2. **Discontinuous films** – Evaporating a discontinuous metal film on top of a membrane punctured by a hole. The transport through a metallic grain can be investigated if one of the metal grains happens to be placed on top of the hole[46].
3. **Mechanical break junctions** – A suspended metallic wire is broken in a controllable way so that the distance between the two parts can be made to be a few nm[47,48].
4. **Electromigration** – Driving high current through a narrow constriction in a wire can evaporate atoms thus creating two closely spaced electrodes[49].

5. **Angle evaporation** - Using advanced e- beam lithography combined with evaporation at various angles allows the fabrication of closely spaced electrodes[50].
6. **Electrostatic trapping** – Once two electrodes are closely spaced, applying voltage between the electrodes can attract nanoparticles to the gap[51].
7. **Linker molecules** – Growing an adhesive layer of linker molecules on the substrate allows the bonding of the nano-objects to the surface. One would then spread the particles on the surface with the hope that one would bridge the gap between the electrodes[52].

There are several crucial limitations in the above listed techniques: The success rate for producing devices is relatively low (typically about 10%), they rely on chance and there is large variation between samples. In addition, there is only limited knowledge of the exact geometry of the system. Even when conductivity through the nano-object is measured, there is uncertainty on the number of particles that connect the leads[53,54]. It is also very difficult to determine the role of the contact resistance on the total system resistivity. Furthermore, the systems are usually unstable and the conductivity largely drifts over time. Finally, these techniques don't allow any flexibility and control over the conductivity of the system or the dot-lead coupling. Depending on the microscopic, the system resistance can vary by orders of magnitude from one system to another. All these disadvantages motivated us to search a unique method to connect a metallic nanoparticle to macroscopic leads and control its coupling to the leads. In this study we describe a unique technique by which we connect a metallic QD to external leads and control the dot-lead coupling in a very controllable way which enables us to study the conductance behavior from the closed dot regime to the open dot regime.

CHAPTER 3

EXPERIMENTAL

3.1 Sample Fabrication

We use SPI-MARK™ Unconjugated Colloidal Gold Probes as QDs in our system. Their size ranges from 15nm to 60nm. Colloidal particles in this size range, including gold, are inherently unstable. Usually, by using different types of surfactants in the fabrication process the nanoparticles are more stable. However, any type of surfactant covering the shell of the colloid is usually not conductive and therefore can interfere with experimental results and might affect the transport properties. Hence, we were looking for gold colloids which are free from organic materials on the surface. For this reason we decided to purchase the gold colloids from SPI-MARK company. By using proprietary technology, SPI-MARK colloidal gold unconjugated particles have no protein whatsoever and are free of surfactants. There are still trace amounts of sodium citrate, tannic acid and potassium carbonate present and without them the suspension would become unstable and the gold would precipitate out. The basic ingredient for the technology that permits the manufacture of stable suspensions (e.g. one in which the particles don't clump up) without a stabilization coating is that the overall net charge on the colloidal particle surfaces is negative, and this provides the mechanism by which particles repel one another and the suspension remains stable. However, excessive washing of the colloid can remove or destroy this charge and the stable suspension collapses. High Resolution Transmission Electron Microscope (HRTEM) images, shown in Fig. 3.1, confirm that the colloids are crystalline. Moreover, the colloids are not a perfect sphere and have some irregular shapes.

In this section we describe our technique for fabricating a nano-transistor composed of a metallic dot coupled to metallic electrodes. The fabrication technique combines lithographic and electrochemical methods and enables very fine dot-lead coupling control.

The fabrication involves the following steps:

1. Fabrication of metallic electrodes on insulating substrate with a separation of a few tens of nanometers.
2. Gold nanoparticles deposition.
3. Trapping a nano-particle between the electrodes.
4. Electrodepositing metal on the electrodes from an electrolyte solution to control the separation.

In the following paragraphs we describe in details each of these steps.

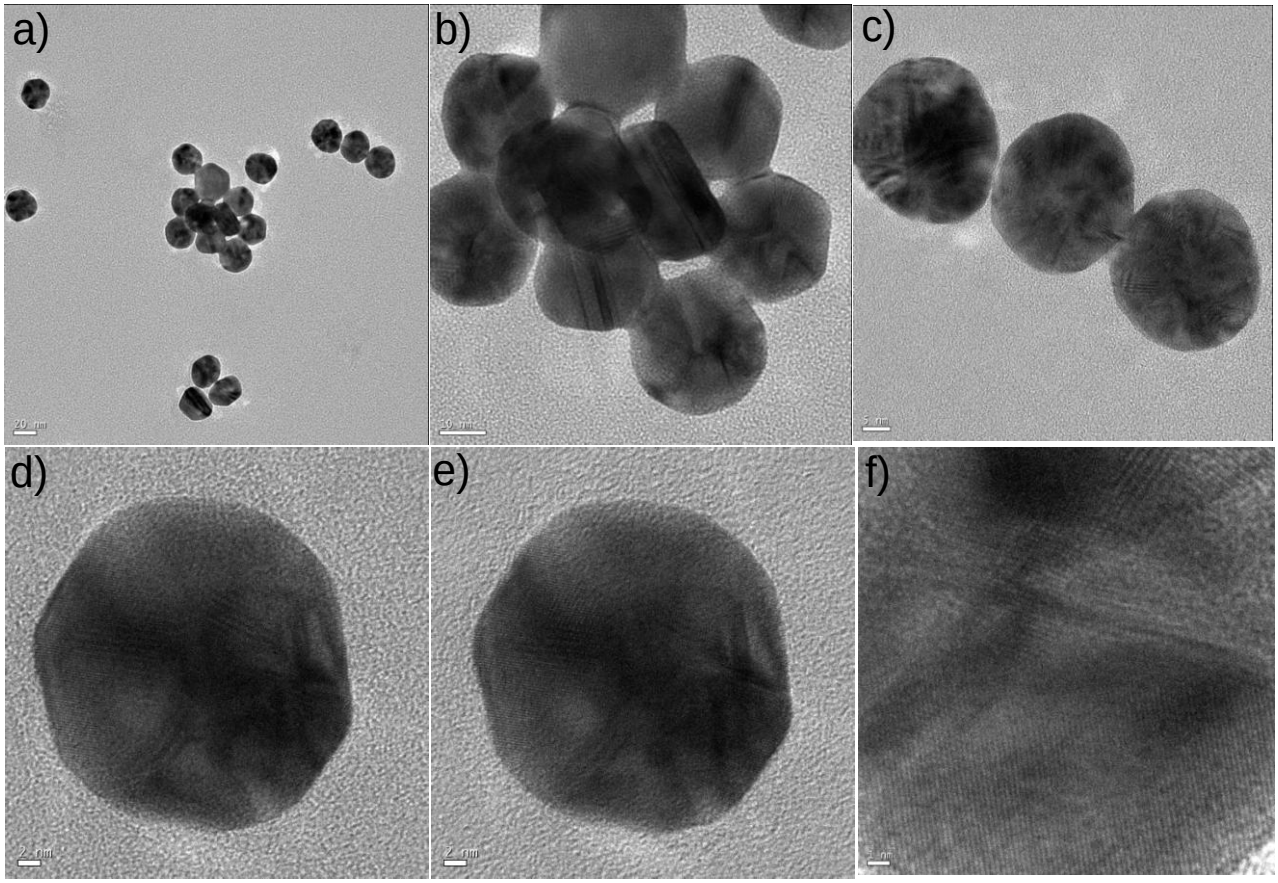

Figure 3.1: HRTEM images of the measured gold colloids.

3.1.1. Metallic electrodes

The size of the nano-transistor we fabricate is very small and reaches the nanometer scale. However, for measuring the transport we need to connect the metallic leads to the "out-side" world, i.e. the measurement equipment. Since the fabrication process involves electro-deposition in which we immerse the sample in a solution, we use for our facility very large metallic electrodes of the scale of a cm. The fabrication of such large metallic electrodes separated by few tens of nanometers is a great challenge and we used two techniques for achieving this. One is a combination of photo lithography and AFM nanomachining (section 3.1.1.1). This technique is a quick technique but effective only for achieving wide gaps of 40-100 nm. The other technique is the combination of photo lithography and e-beam lithography (EBL) (section 3.1.1.2) and is more efficient for achieving better resolution and smaller gaps.

For both techniques the first step is the conventional photolithography for creating very large electrodes. We use a **Kurl-Suss MJB4** mask aligner. The **MJB4** Mask Aligner allows different types of contact exposures (vacuum, hard, soft proximity contact) for different size sample (up to 4 inch in diameter). The achievable adjustment accuracy X, Y and θ is very high. Masks and wafer/substrates to a total thickness of 9.00 mm can be processed. The **MJB4** is equipped with 400 nm exposure optics and lamps that allow a sub-micro exposure in vacuum contact. In our lab we achieved features with size of 0.5 µm. The basic configuration of the **MJB4** achieves its performance with the unfiltered spectrum of a 200W high pressure mercury arc lamp and its associated exposure system with diffraction reduced light path. The 200W lamp provides an intensity of more than 40 mW/cm^{2}at broadband and more than 20mW/cm^2 at i-line. A photo of the **MJB4** Mask Aligner used in our lab is shown in Fig. 3.2.

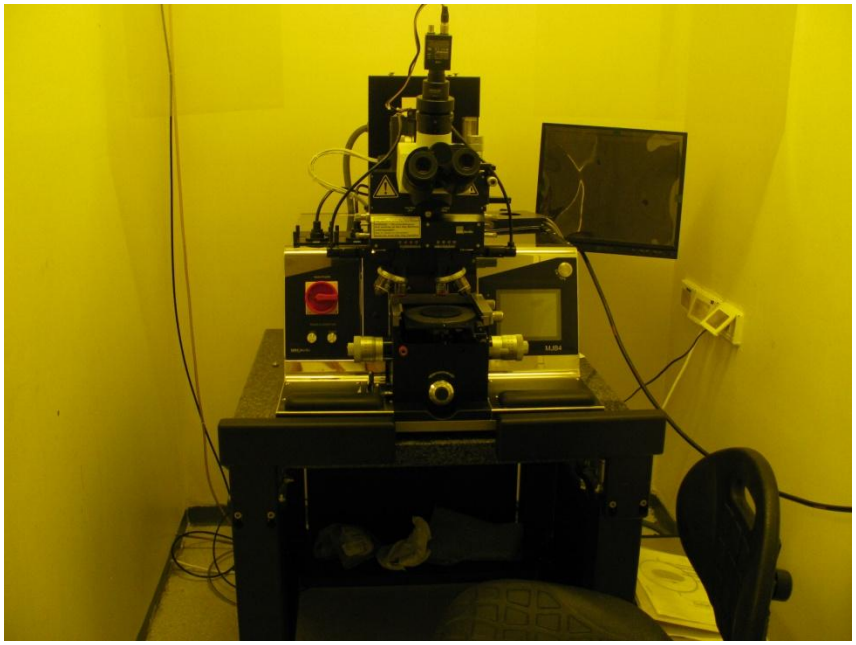

Figure 3.2: Kurl-Suss MJB4 mask aligner used in our lab.

We decided that the electrodes should be made of gold for several reasons. First, we preferred that the electrodes were made of the same material as the nanoparticle. Second, gold is very "soft" material making it easy to utilize the mechanical nanomanipulation method we use for fabricating two electrodes as will be explained in the following (section 3.1.1.1).

In all of the fabrication stages we evaporated 15 nm Au on top of 5 nm Cr. In principle, Cr and Ti are the metals that are most common to use as adhesion layers to gold. However we decided to use Cr

as an adhesion layer. The reason for that is that Titanium oxidizes and breaks the sequence of the electrodes conductivity when using two lithography steps.

In our lab we use **VST** Thin Film Deposition System **TFDS 2537**. The **VST TFDS 2537** consists of a number of elements: 2 **MDC TEPS-2000** thermal vapor deposition **(PVD)** power supplies and sources, an **MDC CVS-3** e-beam **PVD** source, Commonwealth Scientific **IBS-250** 3 cm Ar Ion Beam Source and **Maxtek MDC-360** deposition controller. All above elements are placed in a vacuum chamber, having base pressure of $1 \cdot 10^{-8}$ Torr. A photo of the **TFDS** we use in our lab is shown Fig. 3.3.

Figure 3.3: VST Thin Deposition System **TFDS 2537** used in our lab.

3.1.1.1 AFM Nanomachining

First we fabricate large electrodes using conventional photolithography. For this purpose we prepared a photomask using EBL and Chromium etching. The photomask is shown in Fig. 3.4. The pattern in the photomask is composed of three electrodes. Two electrodes (right and left electrodes) are connected by a strip of 1 μm width and a few μm length. The gate electrode (middle electrode) is at a distance of <1 μm from the middle of the wire.

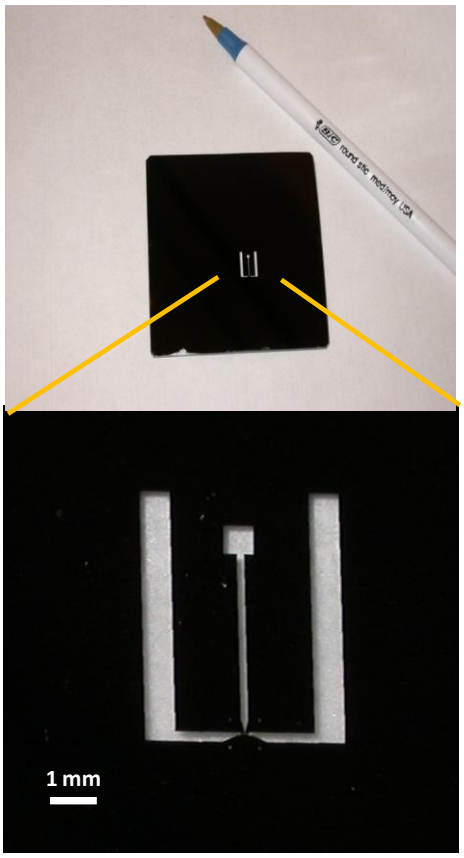

Figure 3.4: Photomask prepared in our lab.

The next step is scratching the strip to perform two separated gold electrodes. For this we use an AFM tip as a scratching tool. We use **DI/Veeco DIMENSION 3100 Scanning Probe Microscope (SPM)** as is shown in Fig. 3.5. It's 90X90 µm piezo scanner allows standard AFM imaging, contact mode and tapping mode. The microscope head is connected to a **Nanoscope IV** controller. This SPM system incorporates the sophisticated Hybrid XYZ scanner which enables high definition nanolithography and direct mechanical nanoscale manipulation using the Nanoman system. The **Nanoman** system is composed of three hardware components, the SPM which provides the basic imaging platform, the Dimension Closed Loop XY Scanning head and the Nanoscope IV Controller which supports the XY Closed Loop Head. By this **Nanoman** system one can manipulate the nanoworld, for instance, creating nanoscale structures, performing direct manipulation of particles and localizing charged placement or oxidizing a substrate.

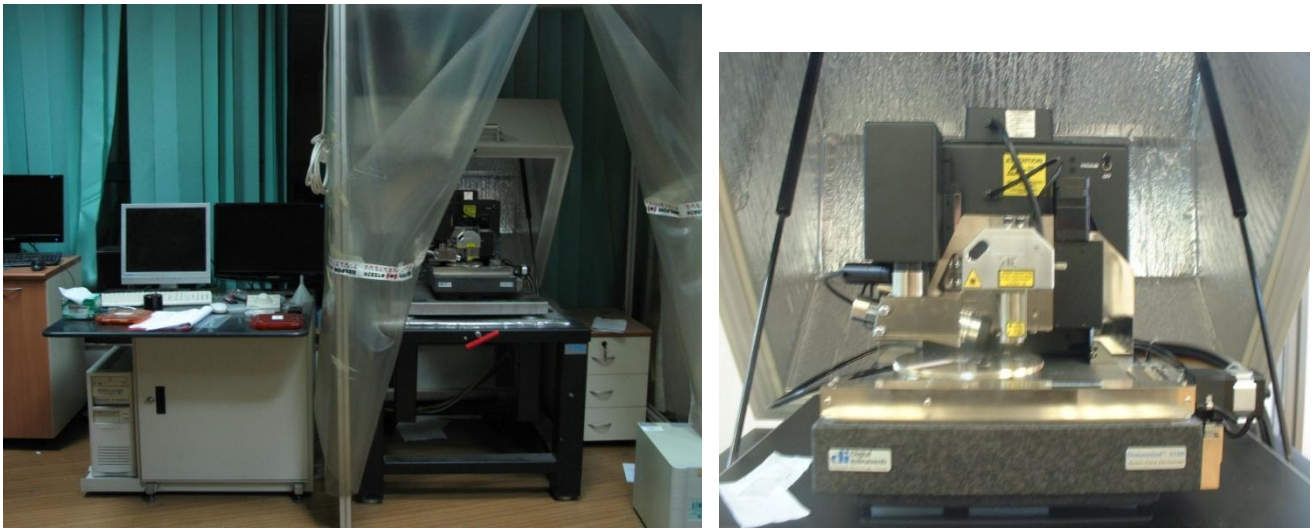

Figure 3.5: DI/Veeco DIMENSION 3100 AFM used in our lab.

The scratching procedure is done by switching off the AFM feedback loop and applying a large force to scribe the Au wire. While the AFM tip scans through the metallic strip until electrical insulation is obtained, the resistance increases from initially $200\,\Omega$ to greater than $1\mathrm{G}\Omega$. This leads to an opening of 40-100 nm in the Au strip. The two sides of the Au strip can now be used as two electrodes. Scratching the Au wire to achieve a narrow gap is a very challenging task. On the one hand by the AFM tip one has to deeply groove the film and totally remove the material to achieve electrical disconnection. In our case the film depth is 20 nm composed of 5 nm Cr and 15 nm Au. The Cr is less soft than the Au material, hence a large force is needed to be applied by the tip on the surface. On the other hand the gap should be narrow, much less than 100 nm. For achieving this, the distance the tip is pushed into the surface should be very precise so that it would be low enough to remove all material but not too low to prevent fracturing the tip which results in a very wide gap. We used a commercial available diamond coated tip with stainless steel cantilever (**MICROSCOPES, MODEL: #ULNC-DCB0**) since it is hard enough to machine most materials.

For this procedure we contact mode. In contact mode the tip is brought in contact with the surface of the sample. The force between the tip and the sample causes the cantilever to deflect in accordance with Hook's Law, exhibiting a spring constant that typically ranges between 0.001 to 100 N/m. The ability to monitor this deflection allows the AFM to create an image of the sample non-destructively even if the tip is continuously in contact with the sample. In non-contact modes the tip doesn't touch the surface and since the scratching operation is relatively rough and the tip needs to apply a large force on the surface we found the contact mode more suitable for this operation. To optimize this nano-machining process, the effects of different machining parameters on fabricated wires were investigated. In the following we will mention some of the important parameters. Words in **bold** are the names of the parameters appearing in our software.

The tip is tuned to about 1V before engagement. The voltage which is applied to the tip while moving along path segments (**Tip voltage**) is tuned to zero. The interval of time during which the voltage applied to the tip changes linearly from the initial value to the Tip voltage value (**Tip voltage ramp**) is tuned to 0.1s. After the path is complete the voltage is ramped down linearly over this time period. **Z distance** is the distance the tip is lifted above the sample surface or pushed into it for negative values. When **Z move** button is pressed the tip is pushed to **Z distance** before traversing path and feedback loops are turned off. It is important to note that the parameter **Z distance** is actually proportional to the load force the tip applies to the surface and not always the actual distance the tip is pushed down into the surface. The higher is the **Z distance**, the larger is the force the tip applies to the surface. Different values of Z distance are used to scratch the sample in order to fabricate single grooves. Grooves with different dimension were fabricated. Then the depth of the machined groove was measured by HRSEM imaging. HRSEM imaging for this purpose is more reliable since the image resolution in the AFM is limited by the radius of the AFM tip which is about 10nm. We found that the scratching depth increases linearly with the **Z distance**. The wire is totally penetrated only if the tip is pushed into the surface by an amount of 500 nm. In this case the width of the generated gap is 70 nm. If the applied force exceeds this value the gap becomes wider and applying even larger force results in damaging the tip or breaking it. **Z velocity** is the vertical speed of tip in retracting from or pressing into the sample surface and is tuned to 50 nm/s. **XY velocity** is the tip lateral speed when moving along a selected path. We found that the groove depth didn't depend on the machining velocity.

During the scratching process, the material pilled up on the edge of the shallow groove and did not pill up on the side of the groove. This is very important issue since the scratch results in clean and sharp walls. An AFM image of a typical gap between two Au electrodes is shown in Fig. 3.6.

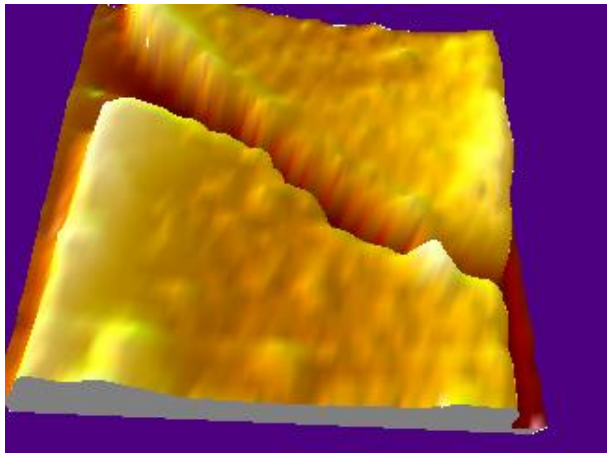

Figure 3.6: AFM image of 1 μm Au wire scratched by the AFM tip.

3.1.1.2 E-beam Lithography (EBL)

For achieving smaller gaps (8 – 40 nm) we use EBL. In our lab we have two EBL systems, **Elphy Quantum (Raith)** and **CABL 9000C (Crestec)** shown in Fig. 3.7. The **Elphy Quantum** is a universal lithography system which consists of a scan generator electronic (hardware) and a PC-based operating software. The **Elphy Quanum** hardware and software are installed at **JEOL 7000P** HRSEM. The system has the control in three major areas of HRSEM: Beam Blanker control, Scan & Signal control and Stage control. Editing and pattern design is made simple with a GDSII internal editor. This allows users to build hierarchy patterns on different levels and designs with any dose level.

Figure 3.7: a) EBL system **CABL 9000** used in our lab. **b) JEOL 7000P** SEM + **Elphy Quantum** EBL system used in our lab.

Since **JEOL 7000P** SEM + **Elphy Quantum** is not a dedicated EBL system, we decided to use the point beam EBL system **CABL 9000C** for the advanced nano fabrication**.** There are several advantages in using this system, and here we would like to list some of them.

Among EBL systems, there are basically two major system styles, shaped beam EBL system and point beam EBL system. The beam in shaped beam EBL system is shaped (square) to achieve faster writing like thick bold pen. The step movement is continuous and not “step & repeat”. By using shaped beam it is hard to achieve <20nm features. Hence it is used mostly for mask writing. In point beam EBL system the beam is round (Gaussian) with spot size of <2nm. Hence this is the finest lithography tool for drawing thinnest patterns with size smaller than 10nm. The beam movement is of “step & repeat” type.

The **CABL 9000C** system is a point beam EBL system. The beam is precise but slower than shaped beam. The e-beam is accelerated at a constant voltage of 50KV so that the wavelength of the e-beam is 0.00535 nm. Since it is a step & repeat stage move style and the beam scans inside of a "field" (the size of the field is the maximum distance the beam can be shifted at a specific magnification) and stage movement stitches such "fields" to create a complete pattern, two main conditions are needed to be fulfilled in order to get high accuracy, (a) Accurate writing inside of a field and (b) Accurate stitching of those "fields". In order to achieve accurate writing inside of a field six important conditions should be fulfilled:

1. Small beam spot and the capability to draw feature with size <10nm. About 7nm of isolated line was achieved in our laboratory using the **CABL 9000C** system, while 10 nm line width is guaranteed.

2. Long term stability in beam current. **CABL 9000C** achieves <+/-0.05% of beam current shift in 10 hours.

3. Long term stability in beam position. **CABL 9000C** achieves <+/-10nm (Point to Point) of beam position shift in 10 hours**.**

4. Noise reduction internally and externally to avoid sudden error. **CABL 9000C** has double magnetic shields made of permalloy so that the external noise (stray magnetic field) becomes only 1% of what is outside of the permalloy chamber. The temperature fluctuations also become 10% of what is outside. This issue is a great advantage since the system can operate in regular environment and not only in extreme clean environment.

5. Writing **uniformly** inside of a "field" by uniformity of current & stigmatism correction. Since the beam scans from a point, astigmatism occurs and it needs to be corrected. Initial corrections were performed prior the shipment. **CABL 9000C** achieves very good beam current uniformity <0.2% (Point to Point) and very good beam size uniformity <+/-8.8% in a "field".

6. By using electrostatic beam deflection and not electromagnetic beam deflection there is no mutual interference between the X and Y deflector due to induces charge. Therefore the accurate beam positioning is realized. Moreover when using electromagnetic deflections overshoots (beam spikes) happen when the beam is scanned. However when we use electrostatic deflections overshoots are not likely to happen.

In order to achieve good stitching of those fields two additional conditions are needed:

7. In order to keep the field size proper the system has to maintain the working distance (WD) constant. If the WD is changed the beam is out of focus and the size of the "field" is changed as well. **CABL 9000C** has a height sensor to keep the WD the same all the time so that gaps between "fields" (bad stitching) will not occur.

8. Accurate measurement of stage positioning. Stage position accuracy depends upon the Laser Interferometer Measurement system. The optic components of the laser interferometer are mounted in a metal chamber. It is known that temperature of metal (iron) piece of 200 m"m long changes 0.1 ^{0}C, the expansion of the metal is about 230 nm. Temperature fluctuations can then lead to a stage position measurement error in range of hundreds nanometers. **CABL 9000C** does two things in order to minimize the metal expansion. First, the chamber is designed in a special way so that the error is minimized to <10nm at 0.1 degree change. Second, this system has a thermal controller which reduces the temperature fluctuations to 10% of room temperature fluctuations.

For the EBL procedure we use standard positive e-beam resist Polymethyl methacrylate (PMMA), usually purchased in two high molecular weight forms (495K or 950K) in a casting solvent such as chlorobenzene or anisole. We make use of 950K PMMA, 2% in anisole. By using this resist the finest patterns can be achieved. We dissolve in a 1:1 MIBK:IPA developer (MIBK is Methyl Isobutyl Ketone and IPA is Isopropyl Alcohol).

The fabrication of the metallic electrodes combines two lithography processes, photo-lithography and EBL. By photolithography we fabricate large electrodes separated by few µm and by EBL we fabricate smaller electrodes on top of the existing electrodes using an overlay process. Here, we use a different photolithography mask shown in Fig. 3.8. This mask was purchased from **Photo-Sciences** company. The mask contains a matrix consisting of 6x6 sample features as is shown in Fig. 3.8a. The size of each sample is ~1x2 cm. The source and drain electrodes are 3µm in width and separated by 4µm. The gate electrode is located at distance of 4µm from them as is shown in Fig. 3.1.7c. Three sets of alignment marks are fabricated as well. Each set is composed of four marks placed at corners of a square centered in the gap and with a size of 10µm, 75µm and 450µm. These marks are used to align the e-beam with the existing structure prepared by the photolithography process.

After the photolithography process, metal depositing and lift-off, the sample is ready for the EBL. For fabricating the smaller features aligned on the large electrodes we used the overlay procedure in **Crestec CABL 9000C.** The overlay procedure begins with the definition of a first reference system. By using two **global alignment marks A** and **B** which were patterned by photolithography, we define the origin and the Y axis. The alignment mark A is positioned on the bottom feature in the second column in the matrix, while mark B is positioned in the top feature in the same column. The large distance between the global marks A and B enables high accuracy in the definition of the stage reference system. This global alignment is used for the correction of the wafer rotation and also allows to blindly move the stage to the relative positions where EBL is to be done. There, mark recognition is performed using **local alignment marks** to finely match positions and dimensions of photolithography and EBL.

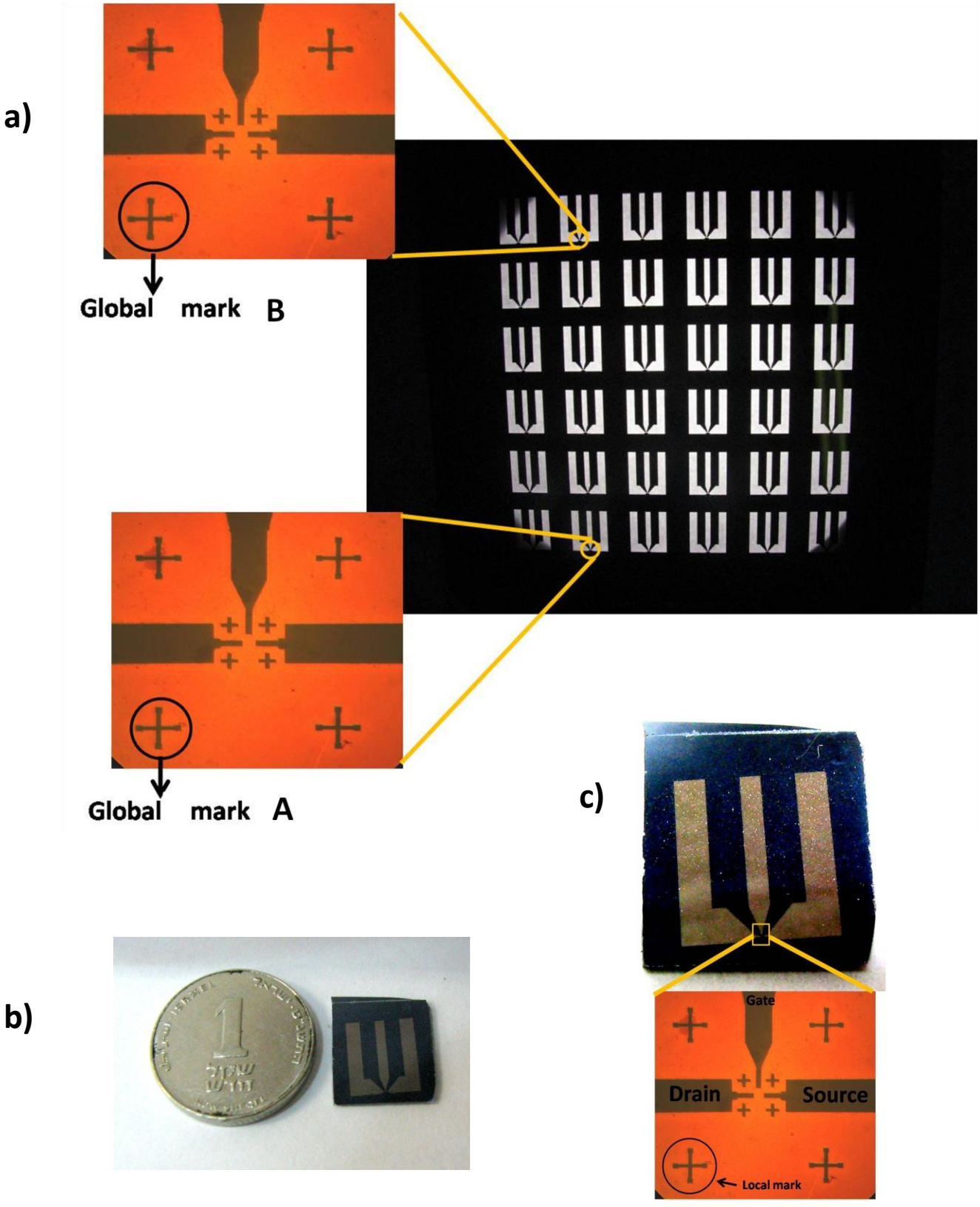

Figure 3.8: a) Mask image taken by an optical microscope. Global marks are indicated by arrows. **b,c)** Samples after the lithography process and lift-off process. Local mark is indicated by arrow.

For the writing procedure we used a Write Field size of 60 x 60 µm and e-beam current of 50 pA. Using these parameter and the alignment process we succeeded to achieve fine electrodes separated by a very small gap of 8-40nm. Fig. 3.9 shows HRSEM images of the sample after EBL process at relatively low magnification. The centered small electrodes (made by EBL) are aligned to large electrodes (made by photolithography).

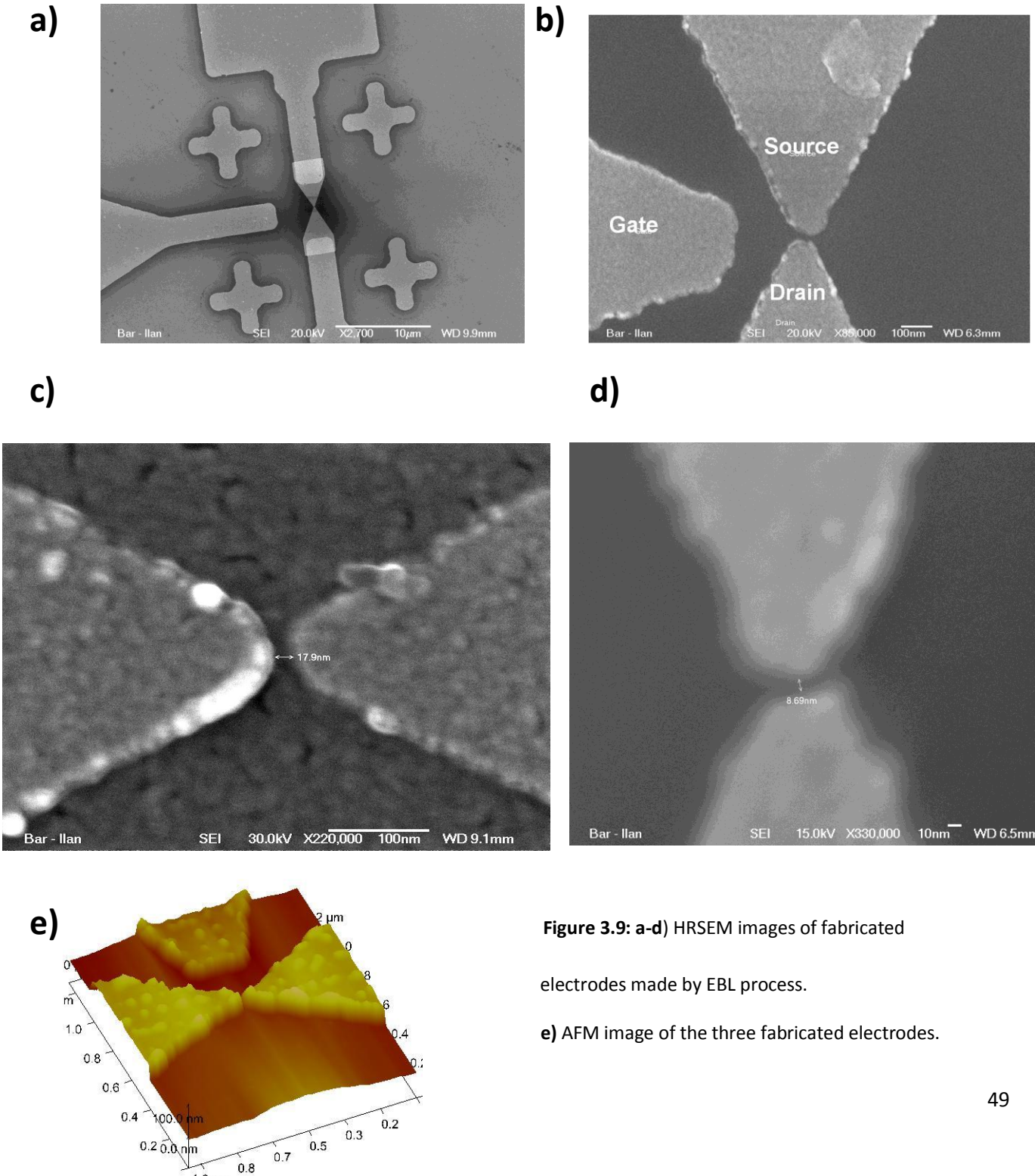

Figure 3.9: a-d) HRSEM images of fabricated electrodes made by EBL process.

e) AFM image of the three fabricated electrodes.

In sections 3.1.1.1 and 3.1.1.2 we described two ways for fabricating gold electrodes separated by a very small gap. One way is scratching Au wire by an AFM tip (section 3.1.1.1) and the other way is fabricating separated gold electrodes by EBL. We found the second way more efficient to us, since by EBL we could achieve smaller gaps (< 20 nm). Moreover by using EBL the tips of the electrodes are very sharp while by scratching a wire of 1 μm one creates wide leads which results in high number of channels between the dot and the leads. Using AFM nanomachining could be an alternative method for measuring colloids with larger size. Using this method can save time since there is no need of an additional evaporation stage and lift-off.

3.1.2 Gold Nanoparticles Deposition

The nanoparticles we use are gold colloids having diameter of 10-60 nm. As was mentioned above we use colloidal particles in solution which are stabilized by negatively charged ions that prevent agglomeration of the particles in solution. We use this negative shell as a means to stick the particles to the surface by an adhesive layer. By using an organic layer that is terminated with amino groups, it is possible to adsorb the negative shell of the particles to the substrate by electrostatic interaction. We chose Poly-L-Lysine (P.L.L) as an adhesive layer. The chemical structure of the P.L.L is shown in Fig. 3.10a.

The sample should be freshly cleaned prior to the P.L.L deposition. Usually after the EBL process the sample might have residues of organic contaminations. We use organic solvents to remove these contaminations. First, we sonicate the sample for 15 minutes in each of the following solvents: acetone, methanol and iso-propyl alcohol. Then we dry blow the sample using ultra pure nitrogen. At this stage the sample is ready for P.L.L deposition. The interaction between the P.L.L and the substrate is electrostatic and based on the interaction between the hydroxyl groups on oxide surfaces which are negatively charged and the amino groups of the polymer which are positively charged. The P.L.L deposition is a general procedure to be used with every oxide layer sample. We place a 5-20 μl drop of 0.1 % P.L.L solution on the sample. The cleaned sample is hydrophilic as a result of the cleaning procedure, hence the P.L.L drop spreads over the substrate. After a 5 minutes deposition, we rinse the sample with a few drops of ultra pure water and then we dry blow the sample using a weak nitrogen stream. The sample is then dried in the oven at 120 ^{0}C for half an hour. As a result the P.L.L deposition the substrate becomes hydrophobic.

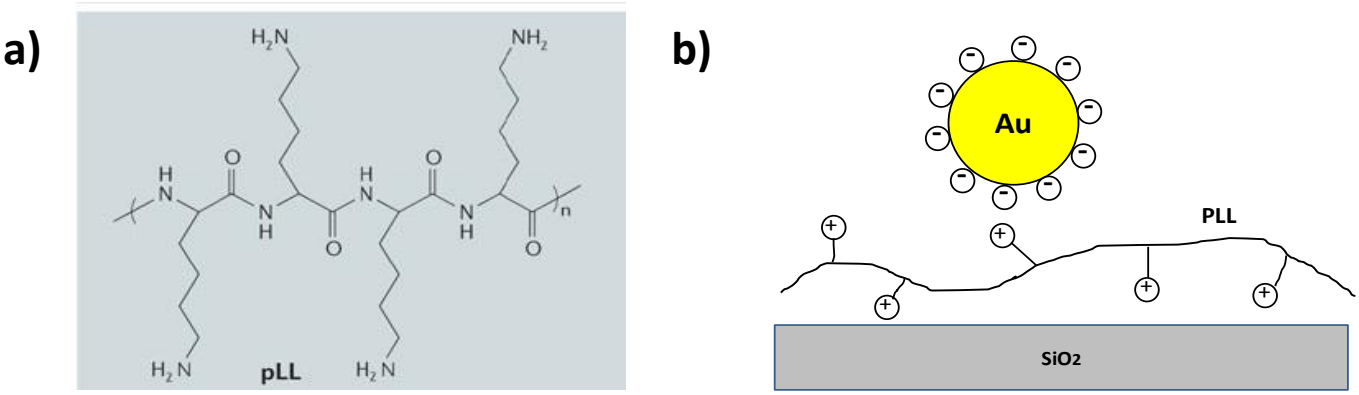

Figure 3.10: a) Chemical structure of the P.L.L. **b)** Schematic picture of a gold colloid electrostatically connected to the SiO2 surface through the P.L.L.

After the deposition of the adhesive layer the sample is ready for the deposition of the particles. The particles deposition takes place by adding a 10-20 µl drop of the solution on the modified substrate for a specific time period. During the deposition process the negative charge on the colloid is electrically connected to the positive charge in the P.L.L. A schematic picture of a gold colloid electrically connected to a P.L.L is shown in Fig. 3.10b. Then, we carefully rinse the sample with a small amount of water and dry blow using a delicate nitrogen stream. Each colloidal particle solution has different particle concentration depending on the particle size. Therefore, the deposition time differs with the particle size. The rule of thumb is: the smaller the particles, the shorter the deposition time. For our sample in which we manipulate and study single particles, it is advantageous to use low density. For instance, for medium density (~20-30 particle per 1 µm X 1 µm) we use a 15 minutes deposition of 15nm particles and 45 minutes of 30nm particles. HRSEM image of gold colloids randomly connected to the SiO_2 wafer with three metallic leads is shown in Fig. 3.11.

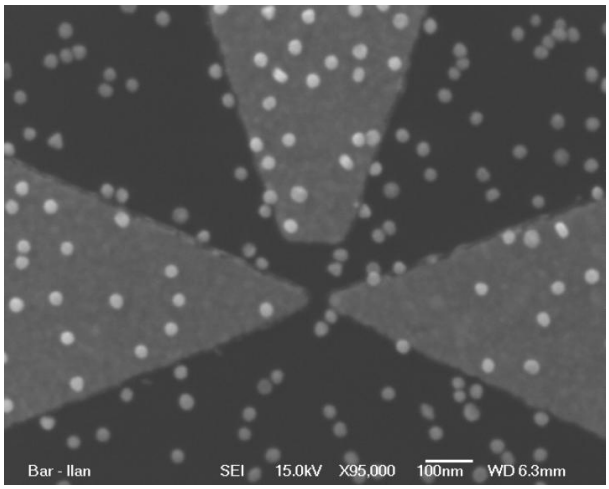

Figure 3.11: HRSEM image of the sample after deposition of gold colloids on the surface.

It is important to mention that after the nanoparticles are electrostatically connected to the surface they are very stable and do not move unless a very high electric or mechanical force is applied to the nanoparticles even after leaving the sample for days or lifting the sample from one place to another, AFM scanning confirms that all the nanoparticles are placed at the same position.

3.1.3 Trapping a nanoparticle between the electrodes

For placing the nano-particle in a desired location we utilize the AFM Nanoman tool which enables mechanical nanomanipulation. The nano-particle is moved between the electrodes using the AFM tip, by "kicking" the particle to the right position. A schematic illustration of an AFM tip pushing a colloid into a gap is shown in Fig. 3.12b. This procedure was performed by using the tapping mode in contrast to the scratch operation described above. The reason for this is that tapping mode inherently prevents the tip from sticking to the surface. This property is very important for this gentle operation of manipulating nanoparticles. When using contact mode for manipulating nanoparticles, the nanoparticles could be detached from the surface and stick to the tip. In tapping mode during scanning over the surface the tip assembly with a normal stiffness of 20-100 N/m is sinusoidally vibrated at its resonance frequency by a piezo mounted above of it and the oscillating tip slightly taps the surface. The amplitude of the oscillation, known as the **Amplitude Setpoint**, is about 20-100 nm. During the scanning the piezo is adjusted using feedback control in the Z direction to maintain a constant (20-100 nm) oscillating amplitude. It means that when the feedback loop is turned-on a constant minimum tip height above the substrate is maintained. The feedback signal to the Z direction sample piezo (to keep the setpoint constant) is a measure of surface roughness. Unlike contact mode, in tapping mode the tip has sufficient oscillation amplitude to overcome the tip-sample adhesion forces when it contacts the surface. A schematic illustration of a tip scanning by tapping mode is shown in Fig. 3.12c. In order to displace a particle, the tip is pushed into the surface adjacent to the nano-particle as is shown in Fig. 3.12d. Then the feedback loop is turned-off so that the tip can drag the nanoparticle forward to a new position. We follow the particle movement by scanning the area between one “kicking” to another.

The most difficult aspect of manipulation is finding a sample with the right adhesion properties. The nanoparticles to be manipulated must be adhered to a substrate strongly enough so that they are stable during tapping mode imaging, but bound loosely enough so that they can be moved by the lateral force of the tip. Sample preparation and choice of adhesion layer between the wafer and the nanoparticles become critical due to these constraints. Moreover the type of the tip and its mechanical parameters become critical as well. In the following we mention the best conditions we found for achieving the most easy-going procedure. As was described above the nanoparticles are connected electrostatically to the surface. We found the electrostatic connection is best for

mechanical nanomanipulation since the nanoparticles are strongly connected to the surface in a sense that they are stable and not move at all unless we apply a lateral force by the tip. Success of nanomanipulation depends on the tip geometry. In general, blunt tips work better for manipulation. Hence, for mechanical manipulation it is preferable to use coated tips, such as **MESP**'s, because these tips are wider than uncoated Si probes. The down side being that this compromises the resolution of the imaging. However we find the image resolution as a necessary condition in this manipulation. The reason for this is that the tip should be placed adjacent to the centered axis of the nanoparticle. If the tip was not placed on the centered axis the nanoparticle would not reach the desired position but just would be turned around and moved only a small segment of the path. Since the size of the nanoparticles is 30 nm we cannot use tip with resolution smaller than the standard resolution which is <10 nm otherwise in most of the cases we might miss the center axis of the colloid. Therefore we decided to use uncoated tips. We used **FESP** tips **(Force modulation etched Si probe, Veeco Company)** made of the material: 0.01-0.025 Ohm-cm Antimony (n) doped Si. The cantilever properties are: Frequency-60-100 kHz, Long- 200-250 µm, Spring constant- 1-5 N/m. The **FESP** tip is shaped like a polygon based pyramid as is shown in Fig. 3.12a. The radius of the tip can be as small as 5 nm. Although the resolution is satisfying, a lot of trial and error experience was required in order to guess rightly the exact position the tip should be placed at in order to drag the nanoparticle the whole desired path. The most crucial condition for achieving successful nanomanipulation is electrical force parameters applied to the tip. Finding the exact parameters was very challenging and we worked hard for achieving them. Here we mention some of the parameters and the considerations for choosing them. The tip is tuned to about 1V before engagement. **Tip voltage** is tuned to be zero and the **Tip voltage ramp** is tuned to 0.1s. After the path is complete the voltage is ramped down linearly over this time period. **Z distance** crucially depends on the **Amplitude Setpoint** parameter which is set before scanning by tapping mode and on the tip type. The reason for this is that the **Amplitude Setpoint** which is the oscillating amplitude of the tip during scanning determines the exact distance of the tip above the surface. The distance we need to push the tip into the surface to drag an object definitely depends on its height above the surface. For mechanical manipulation the tip should be close to the surface and the Amplitude Setpoint must be then set to a very low value. The best results were obtained when the **Amplitude Setpoint** was tuned to 0.4V and the **Z distance** was tuned to -30nm. **Z velocity** is tuned to 50 nm/s. In this case we found that **XY velocity** is important for the success of this operation and we found that when the tip's speed is too fast the nanoparticle doesn't arrive easily to the desired position. Hence **XY velocity** is tuned to 2 µm/s.

Playing around with the above parameters and choosing the right values of these parameters result in very nice manipulations. Pushing a nanoparticle along a distance of ~0.5 µm requires not more than "three" shots and lasts only few minutes. AFM images recording the particle positions are shown in Fig. 3.12e.

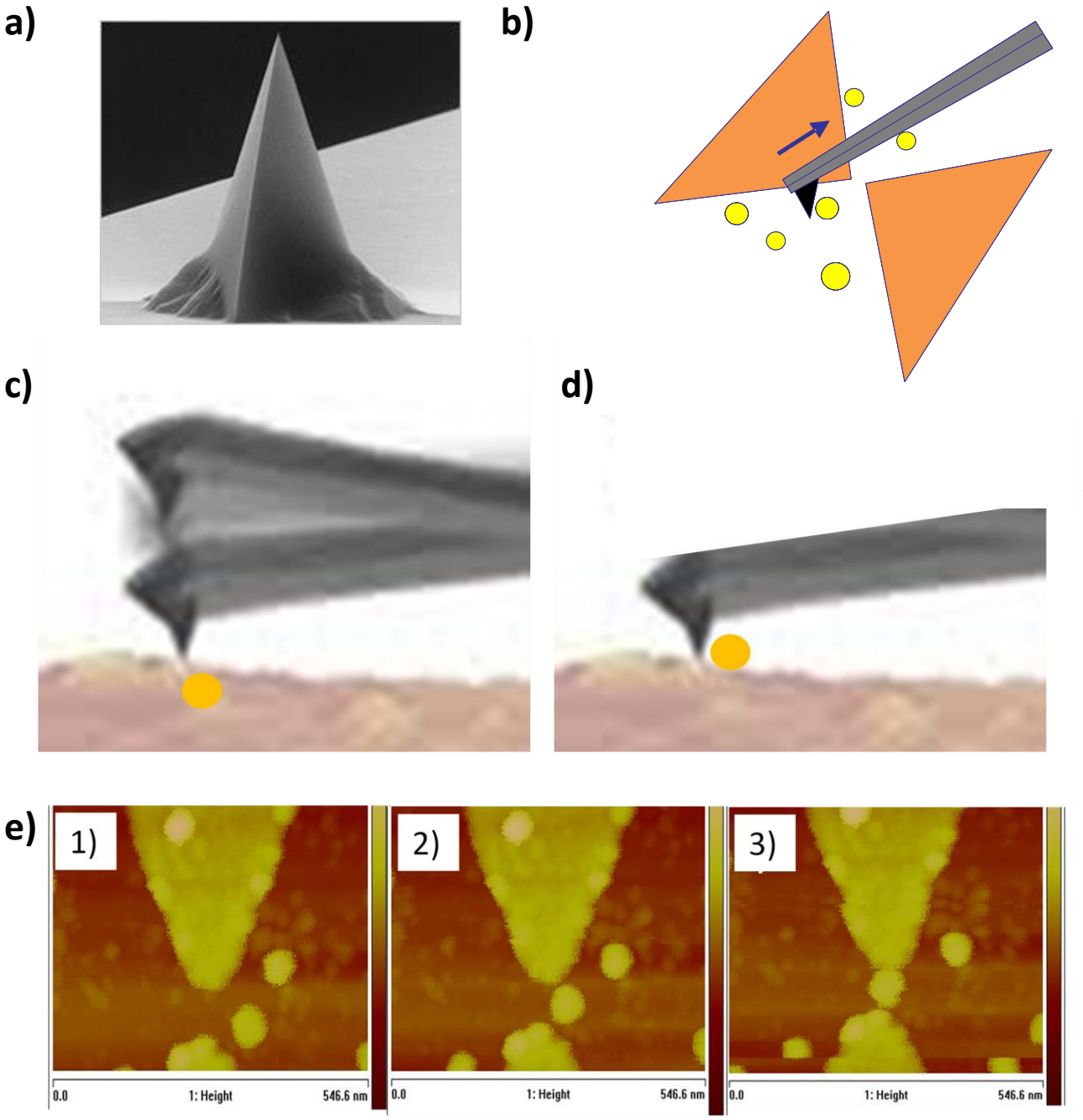

Figure 3.12: a) HRSEM image of **FESP** (**Veeco**) tip used in nanoparticles manipulation. **b)** Schematic picture of an AFM tip pushing a colloid into the gap. **c)** Schematic picture (side view) of a tip scanning a nanoparticle by tapping mode. **d)** Schematic picture (side view) of a tip after it was pushed to the surface and placed adjacent to the tip for the nanomanipulation procedure. **e)** AFM images of the sample at three stages (1-3) of the nanomanipulation process by which the nanoparticle is "pushed" by the AFM tip into the gap.

Figure 3.13 shows HRSEM and AFM images of a nano-particle that has been placed between the electrodes.

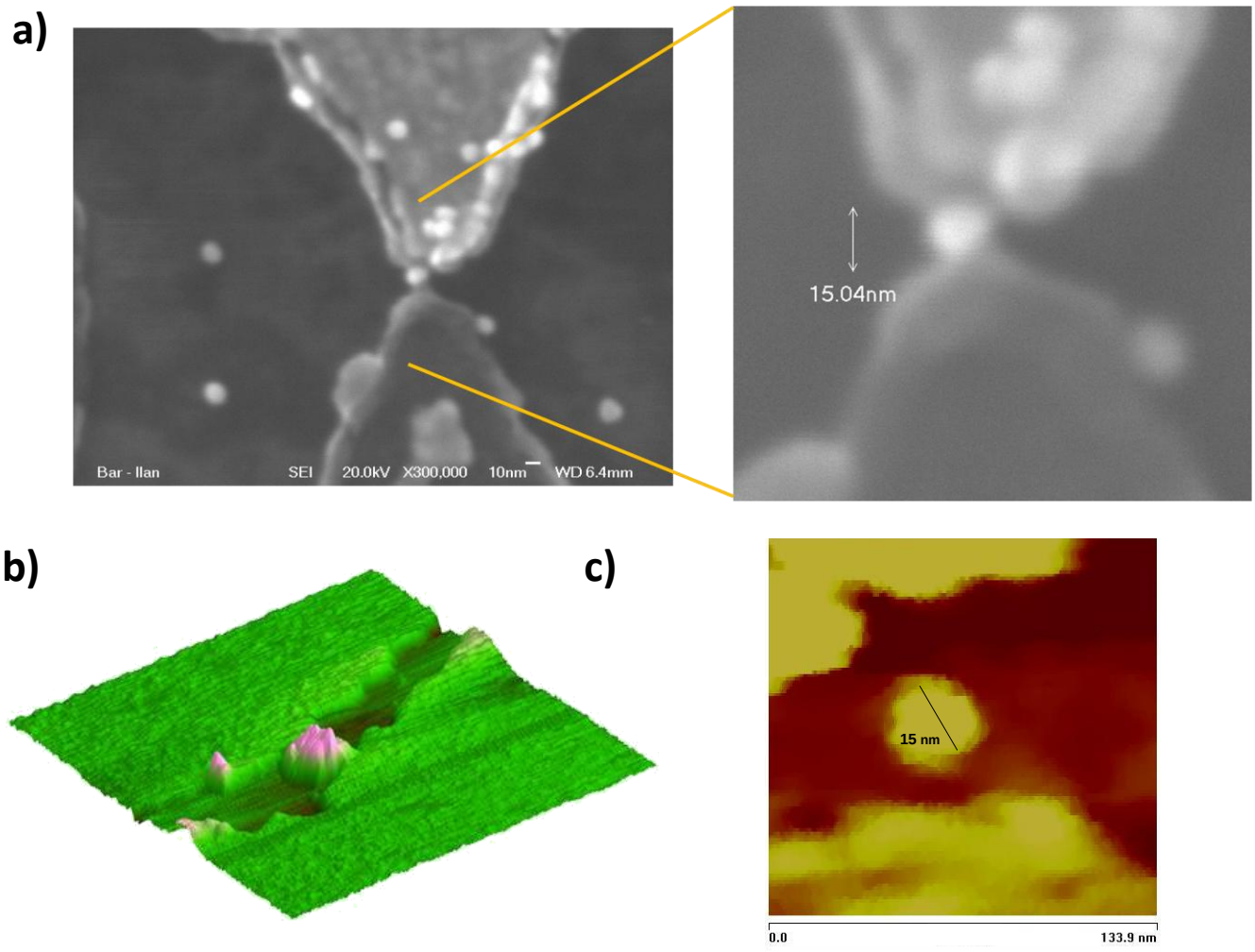

Figure 3.13: a) HRSEM image of a nano-particle trapped between two electrodes after the nano-manipulation process. The electrodes were fabricated by EBL**. b)- c)** AFM images of samples in which both the gap and the particle trapping were performed by the AFM tip.

3.1.4 Metal electrodeposition

At this stage of the fabrication process the nanoparticle is not electrically connected to the leads. For minimizing the gap between the nanoparticle and the leads we use an electrodeposition process by which we grow atoms on the leads until current can be measured. Before the electrodeposition process we place the sample on a glass holder which is connected to a Teflon (Polytetrafluoroethylene) holder. The holder consists of glass and Teflon in order to prevent any metal dissolution reaction in the solution. After placing the sample we connect three electric wires to the wafer by pressing Indium on the metallic strip edges and soldering a Cu wire to these pads. A photo of a sample placed on the holder is shown in Fig. 3.14.

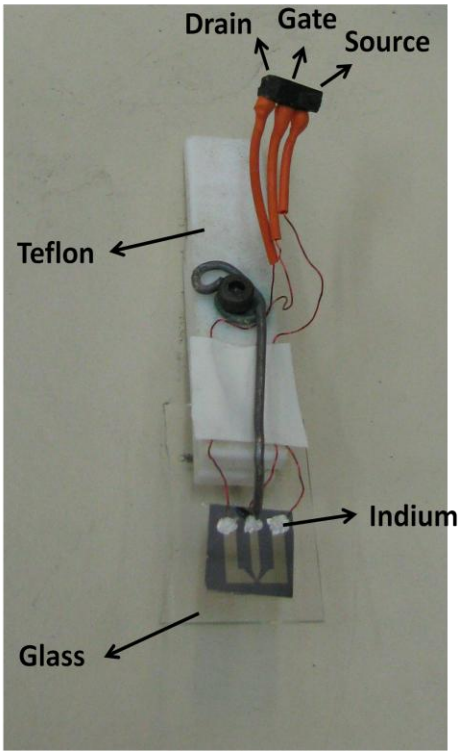

Figure 3.14: A photo of a sample placed on a glass/Teflon holder and connected to three electric wires: source, drain and gate.

Metal is electrodeposited on the top of the existing electrodes from an electrolyte solution[55.] This process results in closing the gap between the electrodes. Our electrodeposition setup consists of solution, counter electrode, reference electrode and working electrodes. The electrolyte is aqueous solution consists of 0.01M of potassium cyanaurate ($KAuCN_2$) and a buffer (PH 10) composed of

1M potassium bicarbonate ($KHCO_3$) and 0.2 M potassium hydroxide (KOH). Au wire of 0.25 mm in diameter with 99.9985% purity is used for the counter electrode and the reference electrode. The two separated gold electrodes are the working electrodes. When applying electrochemical DC voltage between the working electrodes and the counter electrode, the cyanaurate ion accepts an electron from the working electrodes and liberates the cyanide ligands, leaving a neutral gold atom at the surface. Hence, Au islands form on the two gold electrodes, thus closing the gap between the leads and the dot.

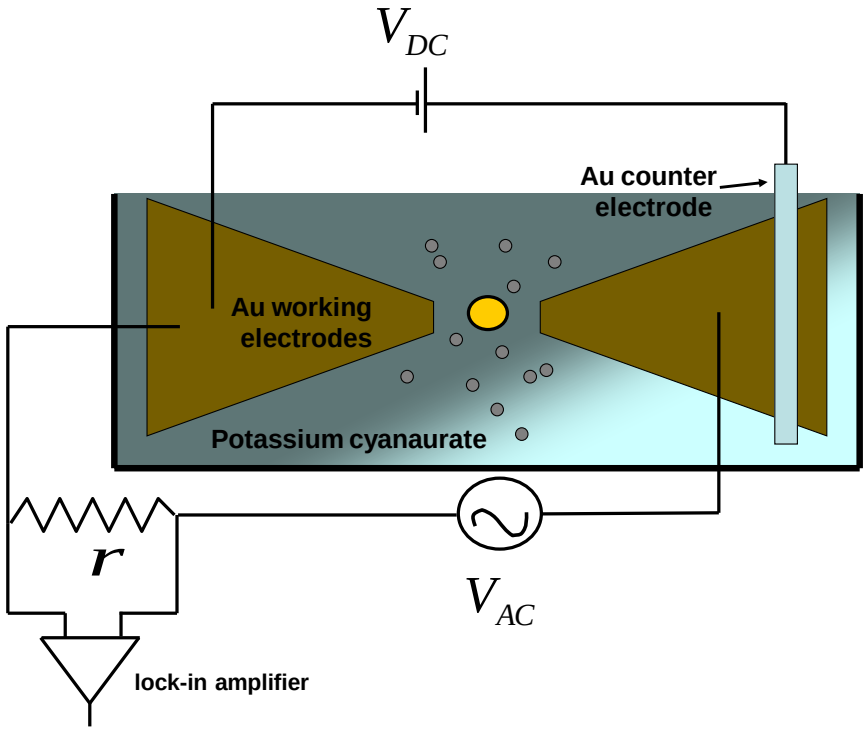

Figure 3.15: Schematic picture of a sample immersed in an aqueous solution for the electrodeposition process.

For measuring the conductance between the working electrodes during the electrodeposition process we use AC conductivity measurement which ensures equal deposition on both the electrodes. An AC voltage of 2mV is applied between the two working gold electrodes. The complete circuit is shown in Fig. 3.15. We are able to monitor the separation between the electrodes once the distance becomes very small. As the initial resistance between the electrodes is infinite the resistance measurement is carried by two terminal method. Fig. 3.16 shows the conductance as a function of time during the deposition process. Jumps in the current are observed implying that atoms might bridge the barriers and connect electrically the particle to the leads. We can control the rate of the growth by changing the DC voltage value (5mV-20mV) between the working electrodes and the counter electrode. If the rate is slow enough, we are able to stop the

process at different degrees of couplings and study the properties continuously from a closed to an open dot. This process is reversible, so that we can control the degree of coupling back and forth by changing the polarity of the voltage.

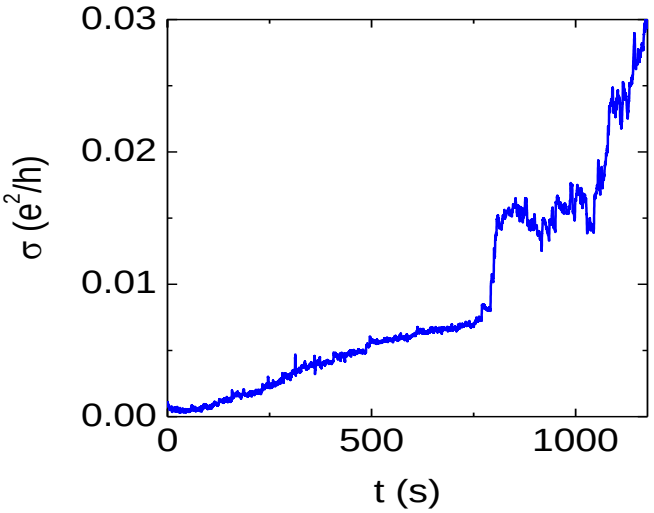

Figure 3.16: Conductance as a function of time during the electrodeposition process.

After electric contact is achieved the sample is taken out of the aqueous solution and transferred to a measurement probe for the electrical measurements. HRSEM image of a sample after applying the electrodeposition process is shown in Fig. 3.17. Very nice and uniform growth is observed.

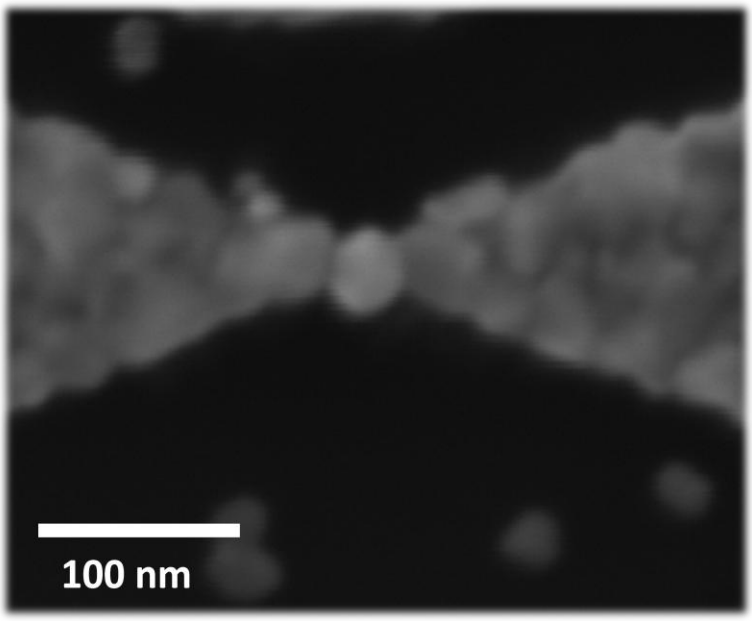

Figure 3.17: HRSEM image of a sample after applying the electrodeposition process.

3.2 Experimental Setup

3.2.1 Probe Setup

For the electrical measurements the sample is mounted on a probe. The pump connector and the measuring port are placed on the top part of the probe while the sample is connected to the lower part of the probe. A photo of the probe is shown in Fig. 3.18.

Figure 3.18: The probe we use for the measurements.

A larger view of the bottom part of the probe is shown in Fig. 3.19. The holder carrying the sample is connected mechanically to a base (by a screw) as is shown in Fig. 3.19b. The sample is located at the same level height of a thermometer which monitors the temperature. Two electric wires are connected through the measuring port to a resistor which serves as a heater. An Aluminum wire (not shown in the figure) connects the probe body to the fabricated gold pads on the sample in order to increase thermal contact.

a)

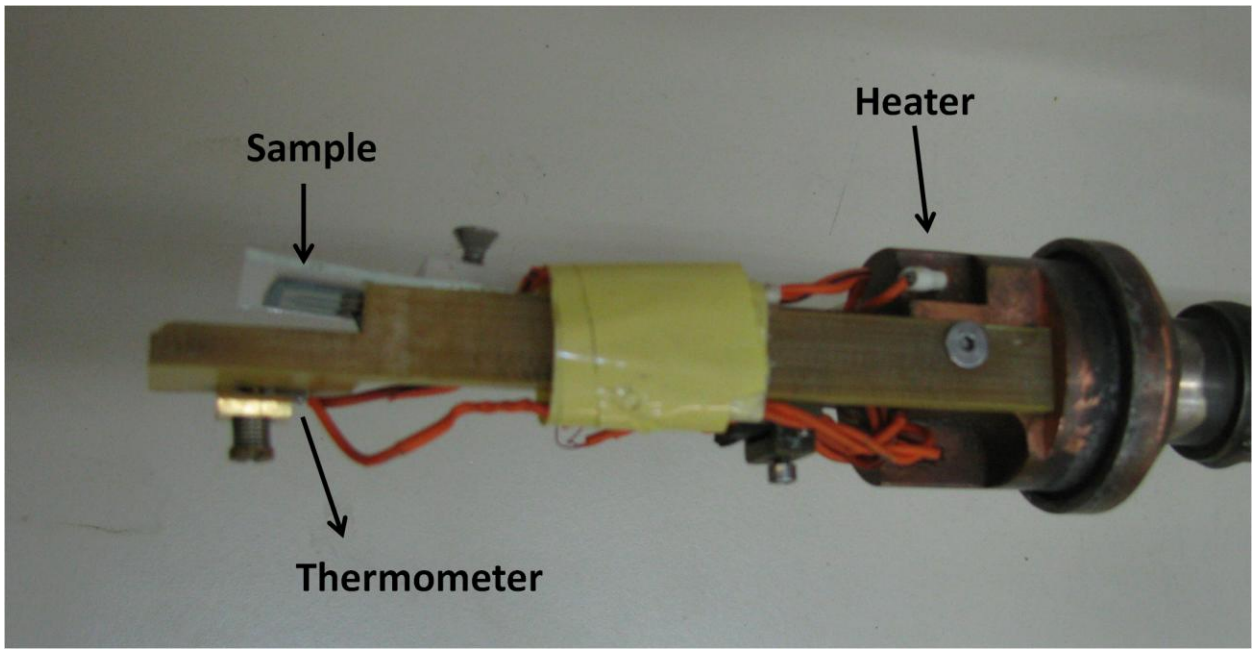

b)

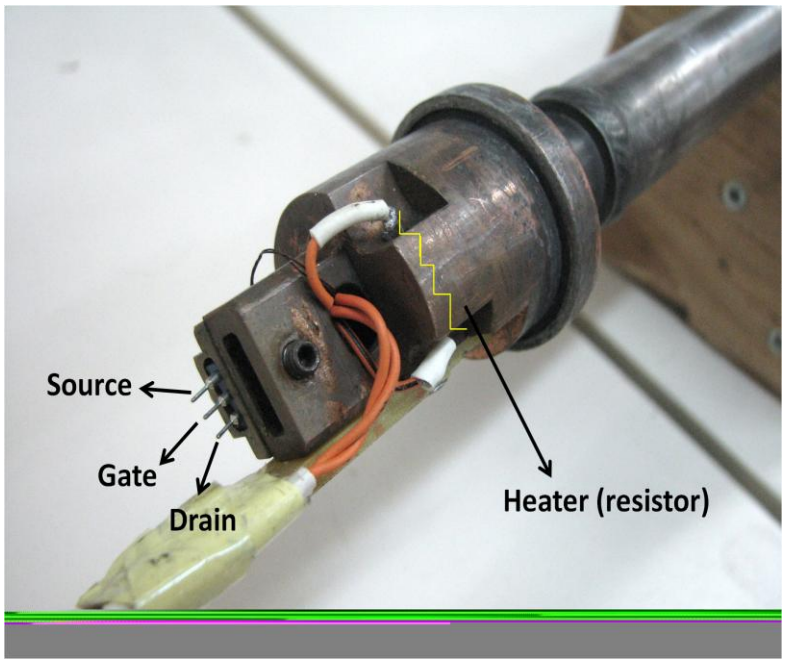

Figure 3.19: a) and **b)** Different views of the bottom part of the probe to which the sample holder is connected.

3.2.2 Measurements

High resistive samples are measured using a two terminal conductance measurements. A known small resistor r, is placed in series with the sample, so that $r << R_{sample}$. The voltage drop across r is measured in order to obtain the current in the circuit. Dividing the source voltage by the measured current provides the resistance of the sample, R_{sample}. AC conductivity measurements were executed using an **AG&G 7265 DSP lock-in amplifier**. Low noise DC conductivity measurements were executed using a **Keithley 2400** digital source meter and **Keithley 2000** digital multimeter.

The temperature was controlled by a heater. **Cernox** and **PT100** thermistors were used to monitor the temperature, with typical currents in the range of 1-10 μA. Home-made Lab-View application was used to control the temperature changes, utilizing a thermostat algorithm.

Magneto-Resistance (MR) measurements were performed using a Cryomagnetics superconducting magnet system. The system includes a custom made solenoid, He cooled, Niobium Titanium superconducting magnet reaching up to 6T, **CS-4-50** power supply, cryostat, helium level sensor and **LM-500** helium level monitor.

All the measurements apparatus used for the measurement techniques described above were connected via GPIB interface to computer Lab-View applications, providing data acquisition and further analysis.

CHAPTER 4

RESULTS AND ANALYSIS

In this chapter we present experimental results of electric transport through a gold colloid connected to two gold electrodes. As was described in detail in the experimental chapter we prepare our samples as follows: On a Si-SiO substrate we fabricate two gold electrodes separated by a gap of 10-30 nm and a perpendicular side gate electrode at a distance of 150 nm. We then spread gold colloids on the surface and use AFM nanomanipulation to push one of the colloids into the gap. At this stage the dot is usually electrically disconnected from the leads. We vary the dot-lead coupling by using electro-deposition process by which we deposit gold atoms on top of the gold electrodes to decrease the dot-lead distance. During the deposition process we measure the conductance between the source and drain and stop the process at any desired resistance. We then cool the system down to 4.2K and measure the conductance as a function of the gate voltage, V_g , and source-drain voltage, V_{sd} . We then further applied the electro-deposition process at room temperature to continue increasing the coupling strength, and measured the conductance as a function of coupling. The measured gold colloids have a diameter of 30nm. The energy level spacing of these colloids is $\Delta \approx 10\mu V$ with charging energy of $E_C = 25meV$. The measurements were performed at $T = 4.2K$. In this system the charging energy is three orders of magnitude larger than the energy level spacing. This energy difference between E_C and Δ enabled us to increase the coupling Γ through Δ and still keep it smaller than E_C thus not losing the charging effects. Considering these energy scales the following results describe system in the classical regime,

$$\Delta << k_\beta T << E_C$$

where the energy scale Γ is varied continuously.

This chapter is divided to two main parts relating to two different types of measurements. One type of measurements is the differential conductance as a function of the bias voltage, $\frac{dI}{dV_{sd}}$ versus V_{sd} which manifests the conductance behavior in the non-equilibrium regime. An example of such a curve is shown in Fig. 4.1a. In section (4.1) we will discuss in details the characteristics of this measurement in our system. In section (4.2) we will discuss the second type of measurement

which is the conductance as a function of gate voltage, $\sigma(V_g)$. An example of this type of measurement is shown in Fig. 4.1b. This curve shows $\sigma(V_g)$ of one of our samples taken at $V_{sd} = 1mv$. A continuous change of the gate voltage leads to typical CB oscillations. Each conductance peak indicates that the charge on the QD increases by 1 and is observed every time the gate voltage is increased by an amount of the charging energy $\frac{e^2}{C}$. Throughout section (4.2) we will show the dependence of $\sigma(V_g)$ on different energy scales: coupling, bias voltage and temperature.

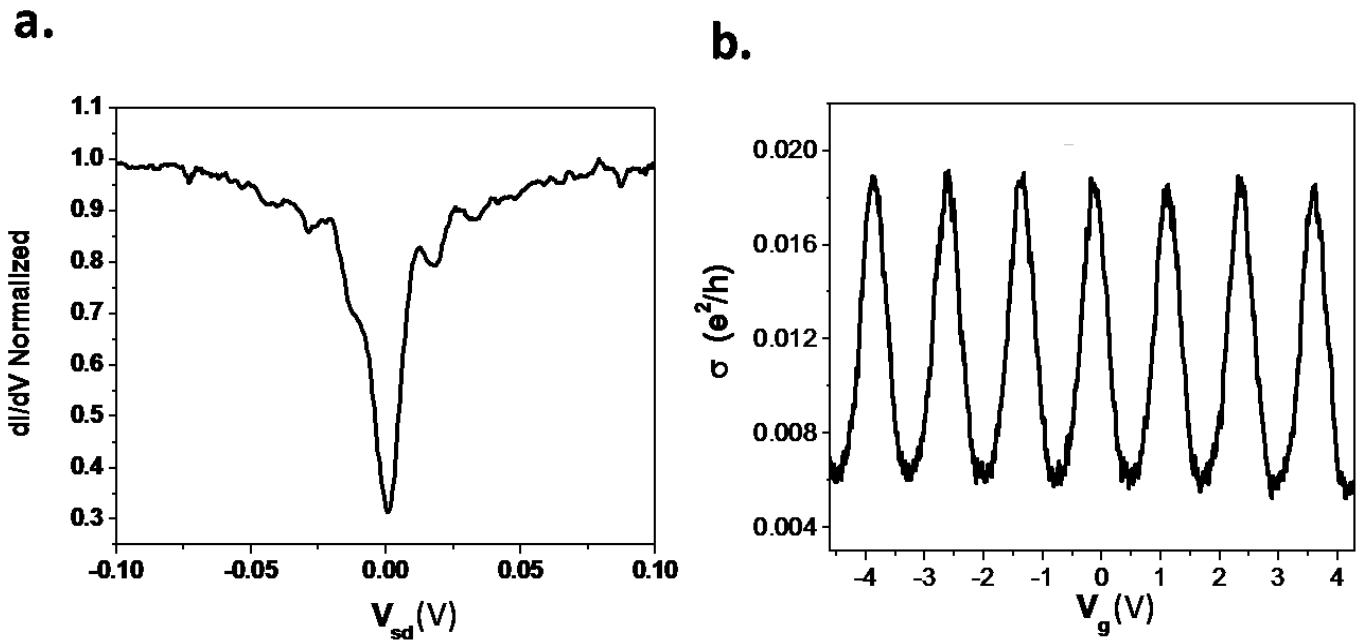

Figure 4.1: Two types of measurements taken in our system**: a)** Differential conductance as a function of bias voltage, normalized to $\frac{dI}{dV_{SD}}(V_{SD} = 50mv)$ **b)** Conductance as a function of gate voltage, $\sigma(V_g)$. CB peaks are observed.

4.1 Bias voltage dependence

4.1.1 Results

A typical $\frac{dI}{dV_{sd}}$ versus V_{sd} curve of a 30nm gold colloid at $T = 4.2K$ is shown in Fig. 4.1a. A very large dip is observed at zero bias. In addition, small oscillations are observed. It seems that as the bias voltage is increased the amplitude of these oscillations is reduced so that at value of $V_{sd} > 45mv$ they are not observable. In order to characterize the dip and the oscillations in the $\frac{dI}{dV_{sd}}$ versus V_{sd} we measured such curves at different values of gate voltage, V_g. The results are shown in Fig. 4.2.

The centered blue curve in Fig. 4.2 shows the conductance as a function of gate voltage of one of our samples taken at $V_{sd} = 1mv$. Two CB peaks are observed with a periodicity of $V_g \approx 1.1V$. The black curves are $\frac{dI}{dV_{sd}}$ curves taken at different values of gate voltage within the range $0V < V_g < 1.1V$ of a typical CB oscillation observed in the centered blue curve. Looking carefully on the $\frac{dI}{dV_{sd}}$ curves, one can see that all the curves exhibit a conductance dip centered at $V_{sd} = 0$. This dip in conductance is pinned to zero bias in all of the curves which means that the conductance dip is V_g independent. Beyond this, one can see an oscillating feature which is superimposed on each curve. Interestingly, it seems that, in contrast to the conductance dip, this oscillating feature is V_g dependent and shifts with the application of the gate voltage.

.’

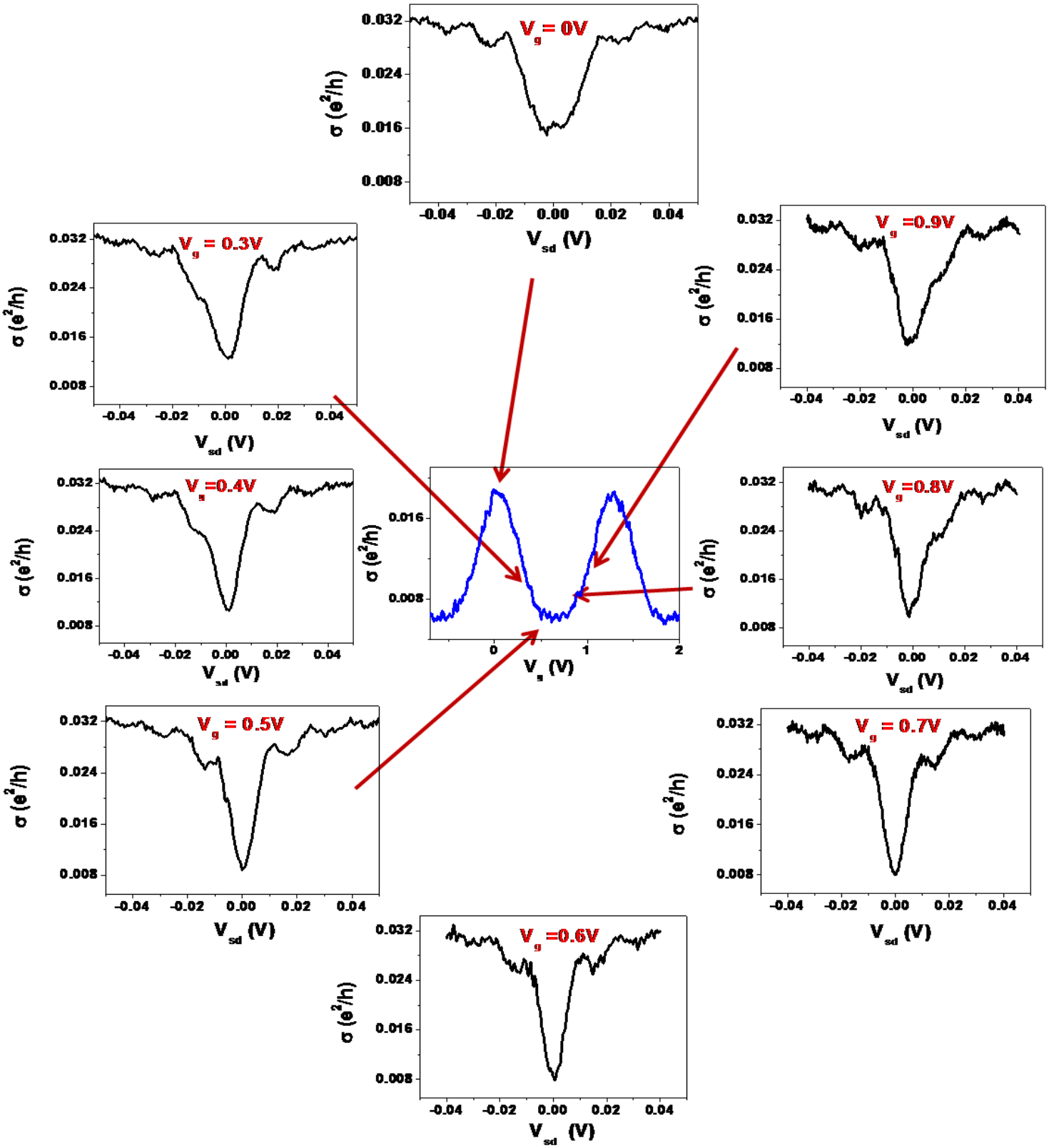

Figure 4.2: The centered blue curve is σ(Vg) measurement of one of our QDs representing the CB conductance peaks. The black curves are differential conductance as a function of bias voltage at different values of gate voltage along the CB conductance peak.

A different presentation which better shows the shift of the oscillatory part with the gate voltage is shown in Fig. 4.3. Many $\frac{dI}{dV_{sd}}$ versus V_{sd} curves are presented where each curve is taken at different values of gate voltage. The curves are shifted one from each other for clarity. One can clearly see that all the curves exhibit a large suppression in the conductance at $V_{sd}=0$ no matter what is the value of the gate voltage. In addition, each curve demonstrates oscillating features which move when changing the gate voltage. This movement can be seen very nicely when following a specific oscillating feature in Fig. 4.3. For example, let's focus on the oscillating feature on the right side of the dip, indicated by arrow pointing on the black curve. When increasing the gate voltage this oscillating feature starts to disappear while at the same time starts to develop on the other side of the conductance dip. When completing a full periodicity of the gate voltage it seems that the oscillating feature moved totally from the right side of the conductance dip (indicated by the arrow on the black curve) to its left side (indicated by an arrow on the yellow curve).

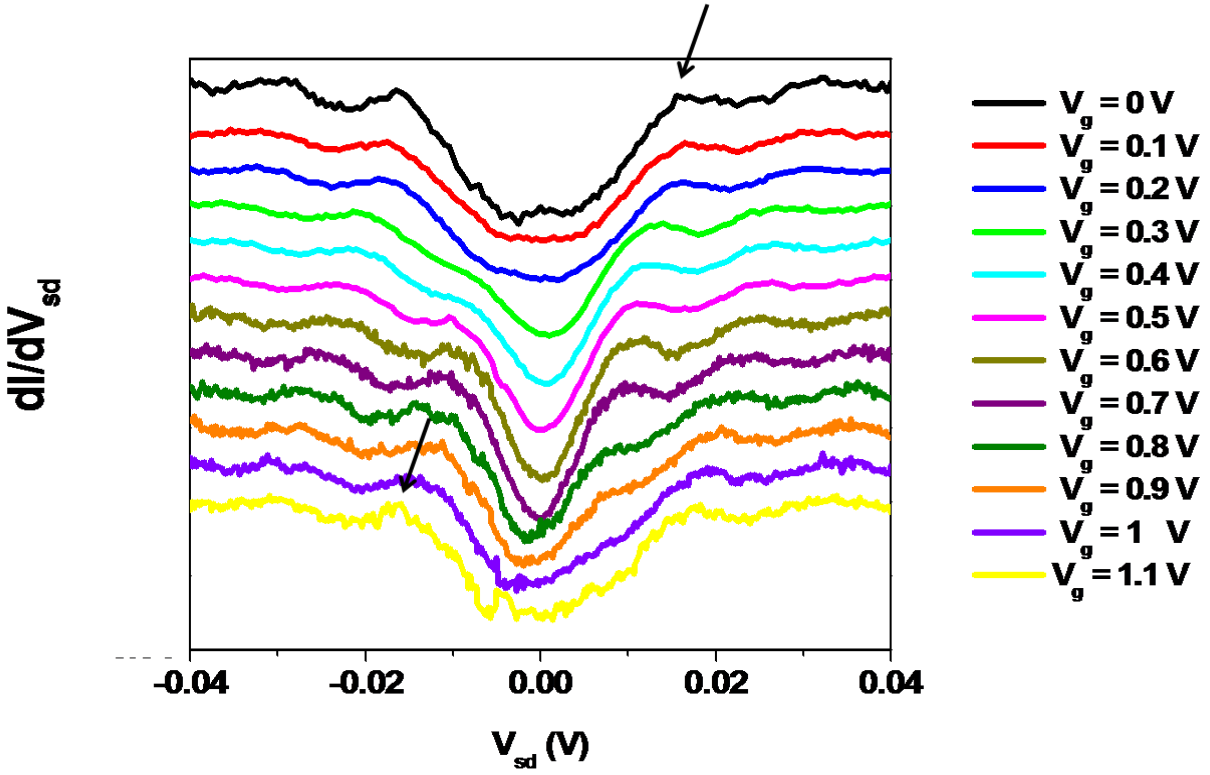

Figure 4.3: The dependence of $\frac{dI}{dV_{sd}} - V_{sd}$ curve on the gate voltage, V_g. Different $\frac{dI}{dV_{sd}}$ versus V_{sd} curves are presented where each of them is taken at different value of the gate voltage. The curves are shifted vertically for clarity.

To summarize, we find that the $\frac{dI}{dV_{sd}}$ curves are composed of two parts, one is a conductance dip centered at zero bias and V_g independent and the other is oscillatory with the bias voltage and shifts with the application of the gate voltage.

4.1.2 Analysis

We analyzed our measured $\frac{dI}{dV_{sd}} - V_{sd}$ curves according to the work done by Golubev and Zaikin[56], which proposes a quantitative description of electron transport through mesoscopic metallic grains in the strong tunneling regime (see introduction section (1.6.3)). The electric current through the dot, as was described in Eq. (1.6.14) was found to be:

$$I(V) = G_{as} \cdot V_{sd} - I_0(T, V_{sd}) - \tilde{G} \cdot e^{-F(T,V)} \cdot V_{sd} \cdot \cos(2\pi N) \qquad (4.1)$$

Here the first term describes an ohmic current, characterized by linear conductance $G_{as} = \frac{1}{R_S + R_D}$ where R_S and R_D are the resistances between the dot and the left and right electrodes respectively. $\tilde{G}$ is a parameter which depends on the dimensionless conductance between the tunnel junctions. The current is reduced below the classical result $G_{as} \cdot V_{sd}$ by an amount I_0 and is modulated periodically with average number of electrons in the dot:

$$N = \frac{C_S \cdot R_S - C_D \cdot R_D}{e(R_S + R_D)} \cdot V_{sd} + \frac{C_g}{e} \cdot V_g \qquad (4.2)$$

The general expressions for the functions $I_0(T,V)$ and $F(T,V)$ are quite cumbersome and are not very transparent. However they can be considerably simplified for the experimentally relevant situation. Since we assume that the dot is asymmetrically coupled and is better coupled to the left electrode (the drain), one can expect that $R_D << R_S$. Thus, the situation of asymmetrically coupled dot is taken into account in the calculation. Also, we present the calculation for the low

temperature limit $T << \frac{\hbar}{2\pi R_D C}$. In appendix A we show our detailed calculation for the $I_0(T,V)$ and $F(T,V)$. The final result for the conductance of a strongly asymmetrically coupled metallic dot is given by Eq. (4.3)

(4.3)

$$\frac{G(V)}{G_{as}} = 1 - \frac{1}{g_D} \cdot (\ln[1 + \frac{\hbar^2}{(t_c \varepsilon)^2}] + \frac{2}{1 + (\frac{t_c \varepsilon}{\hbar})^2}) + \exp(-\frac{g_D}{2} - \frac{2\pi^2}{\tilde{E}_c}(T + \frac{R_D}{R_S} \cdot eV_{sd})) \cdot \cos(\frac{2\pi V_{sd}}{E_c} + \phi)$$

Where $g_D = \frac{h}{e^2 R_D}$ is the dimensionless conductance between the dot and the drain (the well connected electrode), t_c is the charging time of the dot, $E_c = \frac{e^2}{C_s}$ is the charging energy determining the staircase period derived from Eq. 4.2 , $\tilde{E}_c = \frac{e^2}{C}$ determines the amplitude of the CB oscillations, and $\phi = \frac{C_g V_g}{e}$ is the phase of the CS, determined by the applied gate voltage, and $\varepsilon = ((eV_{sd})^2 + (2\pi T)^2)^{\frac{1}{2}}$ is the energy of the system. Eq. (4.3) includes two distinct parts. The first term is a conductance dip centered at $V_{sd} = 0$ which we interpret as a 0D version of the ZBA for the well connected dot. The second term is oscillatory with V_{sd} with a period corresponding to the charging energy of the dot, E_c. The latter corresponds to the CB and is suppressed exponentially with g_D as predicted for the CB phenomena (see Eq. 1.4.23) and with the temperature and source-drain voltage with a typical energy $\tilde{E}_c$, an effective charging energy which determines the amplitude of the CB phenomena and decays exponentially with coupling. Moreover, this term is sensitive to the gate voltage via the phase ϕ. Fig. 4.4 (a-f) shows the same $\frac{dI}{dV_{sd}}$ curves presented at Fig. 4.2 but here a fit to Eq. (4.3) is presented for each curve. The black curve is the experimental measurement while the red curve is a fit to Eq. (4.3). The gate voltage at which each $\frac{dI}{dV_{sd}}$ curve was taken is marked by arrow in the $\sigma(V_g)$ curve (top panel). It is seen that the fits are very good.

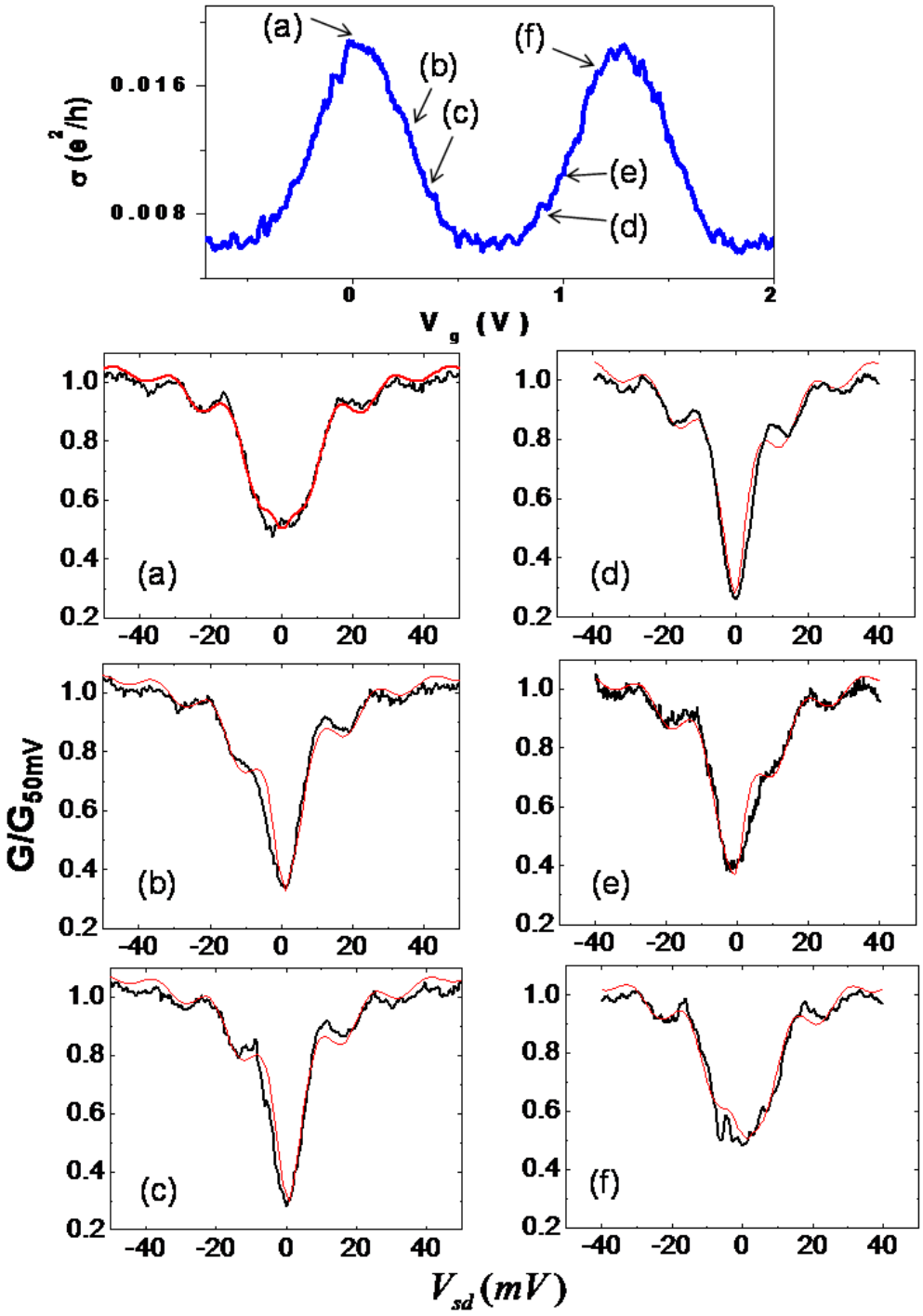

Figure 4.4: a-f: $\frac{dI}{dV_{sd}}$ versus V_{sd} curves of the sample presented at Fig. 4.2 with theoretical fits (red curve) to Eq. (4.3). The value of gate voltage at which each curve was taken is marked by arrow in the top figure.

We emphasize that the same fitting parameters were used for all cases with only ϕ varying between the different curves a-f, thus "sliding" the CS along the voltage axis. Moreover, we note

that we use the same g_D for both terms of Eq. (4.3) thus increasing our confidence in the fitting procedure.

These fits yield g_D=3.5 or $R_D = 7.4K\Omega$. The extracted fitting parameter g_D is found to be larger than 1, while the measured dimensionless conductance is σ(peak)=0.018 as is shown in Fig. 4.4 (top). This finding implies two important things related to our system: First, our system is in the strong coupling regime where the dimensionless conductance between the dot and drain is larger than 1. Second, it turns out that the dot is strongly asymmetrically coupled to the leads. In the example shown in Fig. 4.4 g_D is more than two orders of magnitude larger than g_S where g_S is the dimensionless conductance between the dot and the source.

The fit also yields $\tilde{E}_c = 6.5meV$. This value is smaller than the oscillation's period in the $\frac{dI}{dV_{sd}} - V_{sd}$ curve. The fact that the effective charging energy is relatively small indicates that the CB is decreased due to large effective capacitance. This suppression of the CB effect is consistent with the fact that we are measuring the strong coupling regime.

An important reinforcement to the validity of the conductance form given by Eq. (4.3) is the term $\frac{R_D}{R_S}$ which is in our case equivalent to $\frac{G_{as}}{g_D}$. The best fits were obtained for $\frac{R_D}{R_S} = 0.008$. Indeed $\frac{G_{as}}{g_D} = 0.006$ when substituting the value for g_D as a fitting parameter and the measure conductance peak for G_{as}.

The oscillatory feature is dramatically suppressed as the dot is increasingly coupled to the lead or as the temperature or V_{sd} is raised. However, the CB term shows a different suppression as a function of temperature and source-drain voltage. While the temperature scale is determined by $\tilde{E}_c$, the voltage suppression is determined by $\frac{R_S}{R_D} \cdot \tilde{E}_c >> \tilde{E}_c$, which means that higher voltage is needed in order to erase the CB oscillations. This explains why CB oscillations can be seen in the $\frac{dI}{dV_{sd}}$ curve for $V_{sd} \approx 50mV$ while for $T = 77K$ they are completely suppressed as seen in Fig. 4.5b.

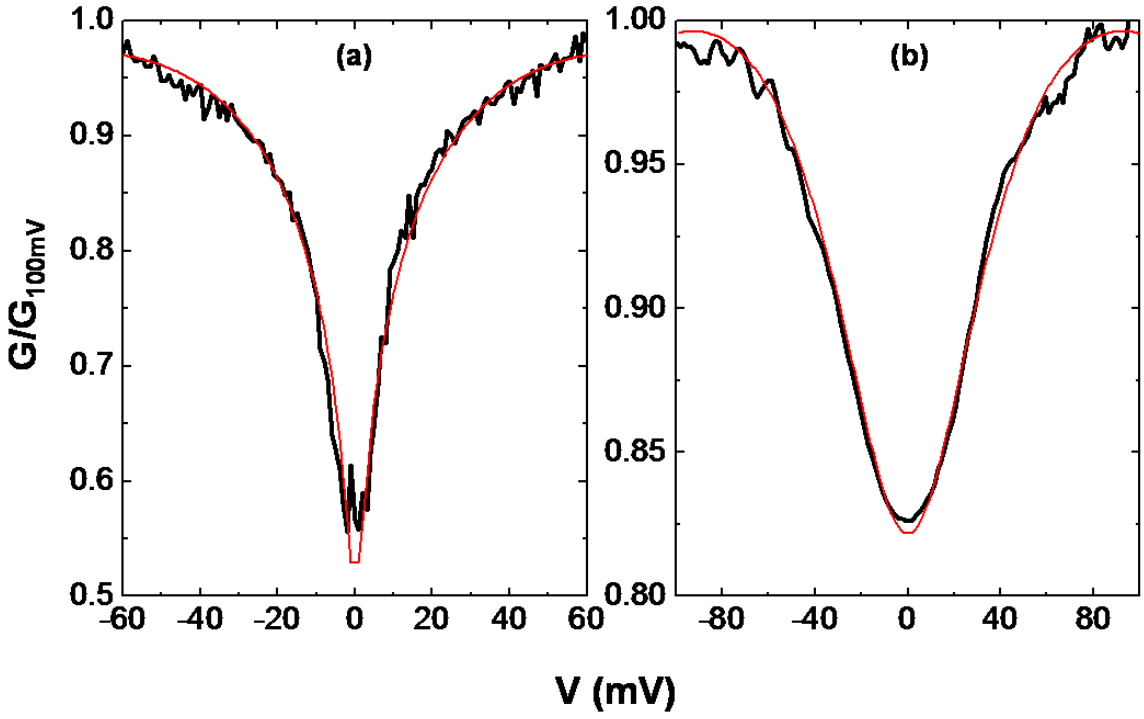

Figure 4.5: **(a)** $\frac{dI}{dV_{sd}}$ versus V_{sd} curve for the case where the dot is coupled more strongly than the case of Fig. 4.2. The light solid red line is the fit to Eq. (4.3). **(b)** $\frac{dI}{dV_{sd}}$ versus V_{sd} curve for the dot of Fig. 4.2 at $T = 77K$ with the fit (red line) to Eq. (4.3).In both cases only a dip around $V_{sd} = 0$ appears with no measurable superimposed oscillatory feature.

The physical origin of the different behavior of the temperature and source-drain voltage stems from their different influence on inelastic processes of electrons in the dot. While temperature affects the occupation of all the electrons in the dot, the source-drain voltage influences only electrons tunneling in or out of it. Since the vast majority of electrons enter (or leave) the dot through the low resistance connection to the lead the relevant voltage scale is proportional to the voltage drop on it, i.e., to $\frac{R_S}{R_D} \cdot V_{sd}$.

As the coupling between the dot and the drain is increased all non-ohmic features in the current are suppressed. However, the oscillatory feature is exponentially suppressed as g_D increases. Fig. 4.5a shows the $\frac{dI}{dV_{sd}}$ versus V_{sd} curve for the same dot depicted in Fig. 4.4 in which the coupling to the drain has been increased. The $\frac{dI}{dV_{sd}}$ curve in this case exhibits only a ZBA like feature with no

signs for CS effects. For this coupling the fit to Eq. (4.3) is achieved for $g_D = 5.5$, (and $\tilde{E_c} = 5meV$). This result indicates that the CB effect is much more sensitive to coupling than the ZBA feature, as expected from Eq. (4.3).

A similar suppression is seen when the temperature is increased. Fig. 4.5b shows the $\frac{dI}{dV_{sd}}$ curve at $T = 77k$. It is seen that at this temperature only a ZBA-like feature is observed and the CS has vanished. Indeed, CB effects are expected to decay with temperature exponentially while the ZBA should be smeared only logarithmically with T (see Eq. 4.3).

The fitting procedure described above was applied for all our measured QDs. In all cases we extracted the parameters g_D and g_S which usually cannot be separated in regular transport measurements. The results are very surprising. For all samples the values of g_D are found to be between 2 and 8. The measured dimensionless conductance, however, is relative small, g<0.1. We conclude that all the measured dots are very asymmetrically coupled to the leads, where the dimensional conductance to the well connected leads is larger than 1.

In conclusion, in this section we have analyzed the $\frac{dI}{dV_{sd}}$ characteristics. The results are interpreted as a superposition of two terms, the ZBA effect and the classical CB oscillations. These two terms show a different dependence on the strong coupling of the grain to the lead g_D, temperature, gate and source-drain voltage.

4.2 σ(V_g) curve

Up to now we have shown the conductance as a function of the bias voltage, $V_{sd.}$ In this section we describe the conductance behavior as a function of the gate voltage, V_g.

Conductance in units of $\frac{e^2}{h}$ versus gate voltage of a typical 30 nm gold colloid is shown in Fig. 4.6. Clear periodic peaks are observed. Dip to peak values are $6\cdot 10^{-4}\cdot\frac{e^2}{h} < \sigma < 5\cdot 10^{-3}\cdot\frac{e^2}{h}$. These values of conductance are typical for the relatively weakly connected dots we measured in our system. In our setup we could not obtain conductance values lower than these.

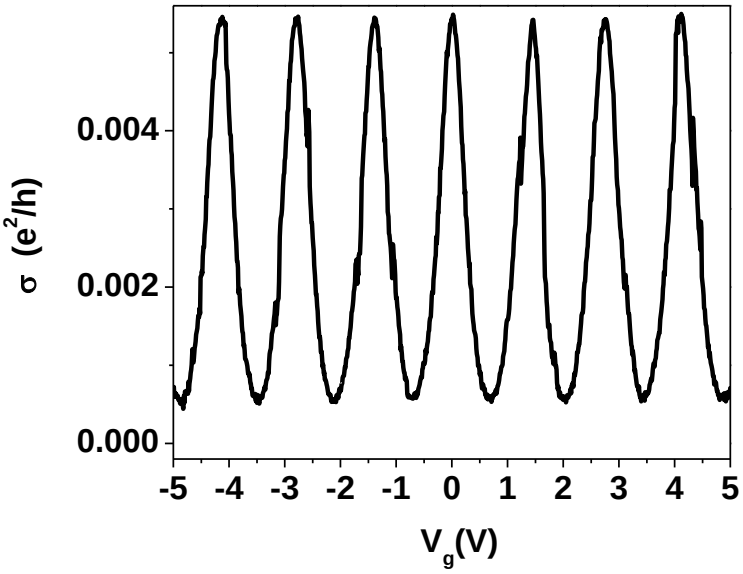

Figure 4.6: $\sigma(V_g)$ of a relatively weakly coupled dot having diameter of 30 nm. The measurement were performed at $T = 4.2k$.

The periodic peaks shown in Fig. 4.6 are attributed to the CB phenomenon, where the periodicity of the conductance peak refers to the charging energy, $\frac{e^2}{C}$. Two points should be noted. First, the width of the peaks is close to the value of the period, E_C. Second, the minima of the peaks (value of the dip) doesn't reach zero. Actually the structure is very close to a sinusoidal shape. It is well known that the theoretical prediction for σ(V_g) in the strong coupling regime is a weak periodic

modulation as shown in Eq. (1.4.24) in the introduction chapter. These imply, again, that the dot in our system is in the strong coupling regime. A good way to check this claim is to see whether the width of the peaks depends on temperature and bias voltage. Fig. 4.7 shows $\sigma(V_g)$ curves, all taken at V_{sd}=0.3mV but at different values of temperatures ranging from 5K-20K. It is seen that the $\sigma(V_g)$ curve raises with the temperature but the width of the peaks is temperature independent. This indicates that the width of the peaks is not governed by temperature.

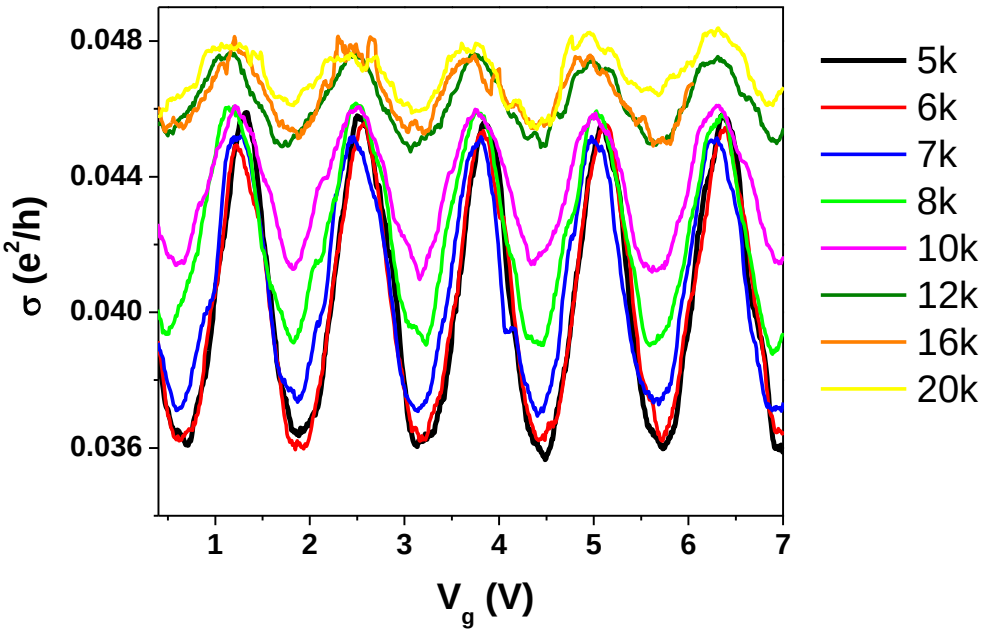

Figure 4.7: $\sigma(V_g)$ of one of our dots at different values of temperatures.

The Orthodox model which describes the weak coupling regime predicts that in the case of $V_{sd} > k_BT$, the bias voltage is expected to determine the width of the peak. This can be observed in the charge stability diagram of a QD as is shown in Fig. 1.10. When increasing the bias voltage the conductance peaks in $\sigma(V_g)$ curve broaden. $\sigma(V_g)$ measurements of the same sample presented at Fig. 4.7 taken at different bias voltages are shown in Fig. 4.8. These measurements show that the width of the peak does not depend on bias voltage either.

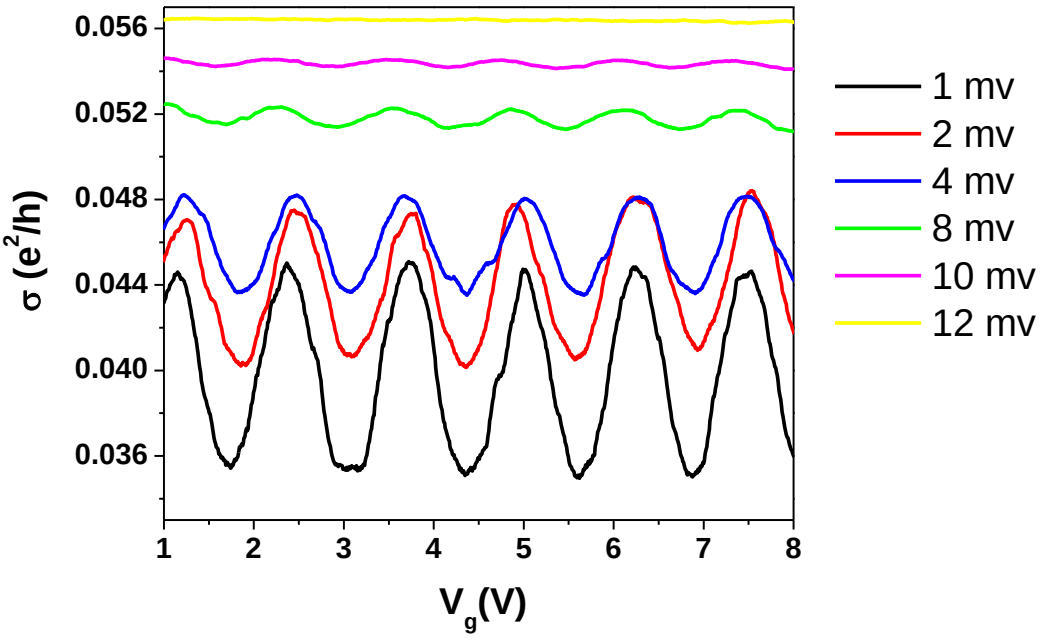

Figure 4.8: $\sigma(V_g)$ of one of our dots at different values of bias voltage.

Since the peaks broadening is temperature independent and do not change when increasing the bias voltage as expected from the weak coupling regime, we conclude that the width of the peaks is governed by the coupling Γ. This is consistent with the high values of the extracted fitting parameter g_D in Eq. (4.3) as was mentioned in section (4.1.2).

All the above considerations lead us to conclude that we are measuring the intermediate/strong coupling regime.

4.2.1 The appearance of a second period in $\sigma(V_g)$ curve

After measuring a set of measurements at specific degree of coupling to the leads, we took out the sample from the probe station to room-temperature environment and immersed the sample in the electro-deposition system in order to grow more atoms on the leads to continue increasing the dot-lead coupling. After few seconds of deposition the resistance of the barriers was reduced and we stopped the deposition process. Then, we loaded the sample again in the probe station to start measuring the conductance in the new degree of coupling. By running this process few times, we could take conductance measurements at different coupling degrees. In Fig. 4.9 we present conductance measurement versus gate voltage of the same sample presented in Fig. 4.6 at two additional degrees of coupling. The black curve is identical to that of Fig. 4.9 and represents the most weakly coupled stage, the red curve represents the intermediate degree of coupling and the blue curve represents the strongest coupling degree. As coupling is increased two trends become apparent. First, the amplitude of the CB peaks decreases with coupling, as expected from a strongly coupled dot (see introduction section (1.4.2)). The second trend is that additional features appear in conductance peaks. At the less connected stage the conductance exhibits symmetric peaks, as can be seen in the black curve. When we increase the coupling the peaks become asymmetric, as is shown in the red curve, where the right side of the peak is much steeper than the left side. When we increase the coupling even further the conductance curve develops into a double peak structure, as can be seen in the blue curve. For characterizing the additional feature we Fourier transformed the three curves. The Fourier transform (FT) is presented in Fig. 4.9b. Very surprisingly the FT reveals two periods which are the same for all of the coupling strengths. However the relative strength between the periods is different for each coupling degree. The FT is normalized to the amplitude of the slow period. It is seen then that as the coupling is increased the relative amplitude of the fast period increases.

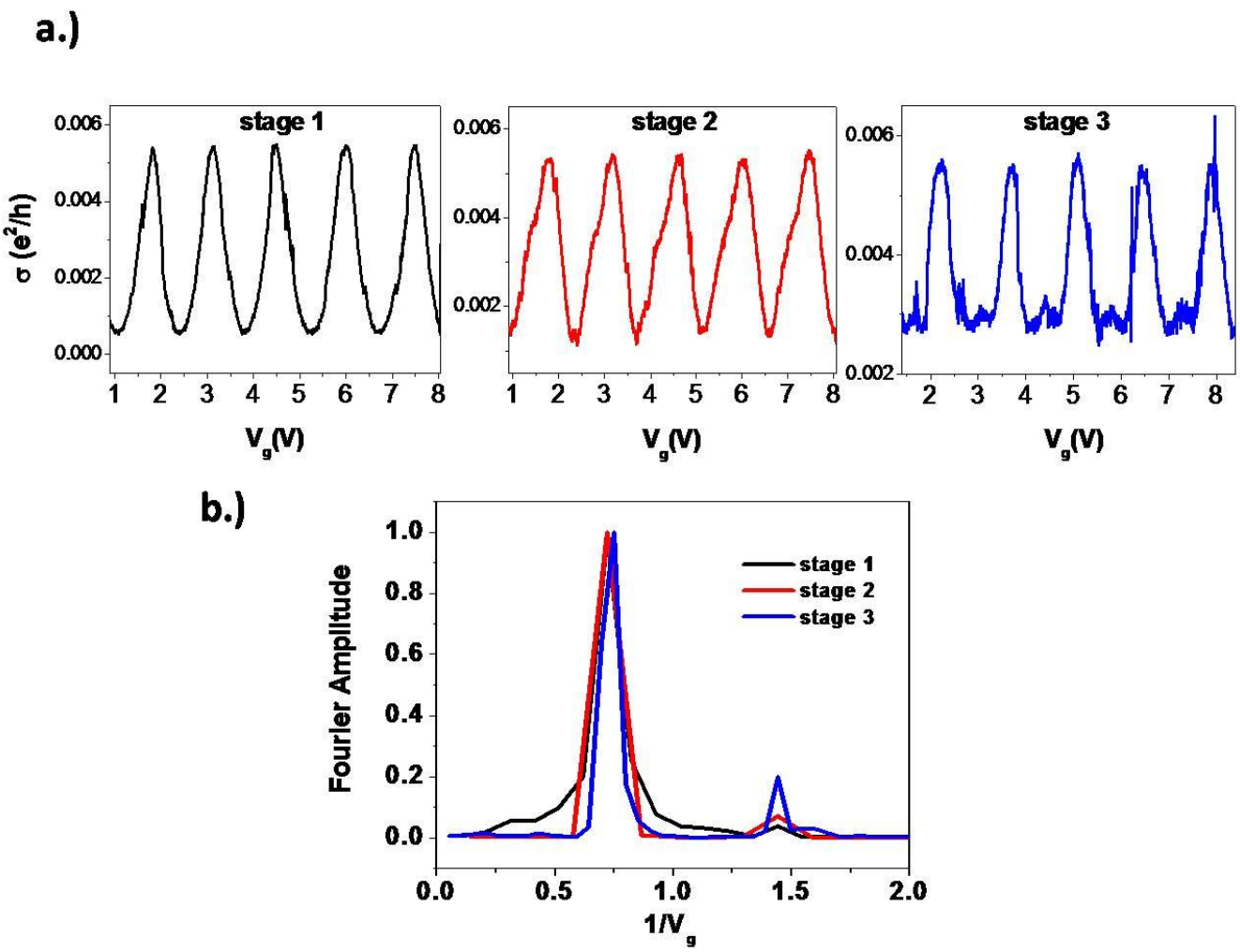

Figure 4.9: a) $\sigma(V_g)$ at three different coupling degrees of the same sample. The black curve represents the most weakly coupled stage (stage 1). The red curve represents the intermediate regime (stage 2) and the blue curve represents the most strongly coupled stage (stage 3). **b)** FT of all the curves present at **a).**

The existence of two periods in $\sigma(V_g)$ curve is not expected at all but this phenomenon was observed in over 15 samples. In most of the samples the frequency of the fast period was twice larger than the frequency of the slow period. However, few samples showed larger ratios between the two frequencies ranging between 2 and 6. Fig. 4.10 shows $\sigma(V_g)$ curves of different samples having different ratio between the slow and fast frequencies.

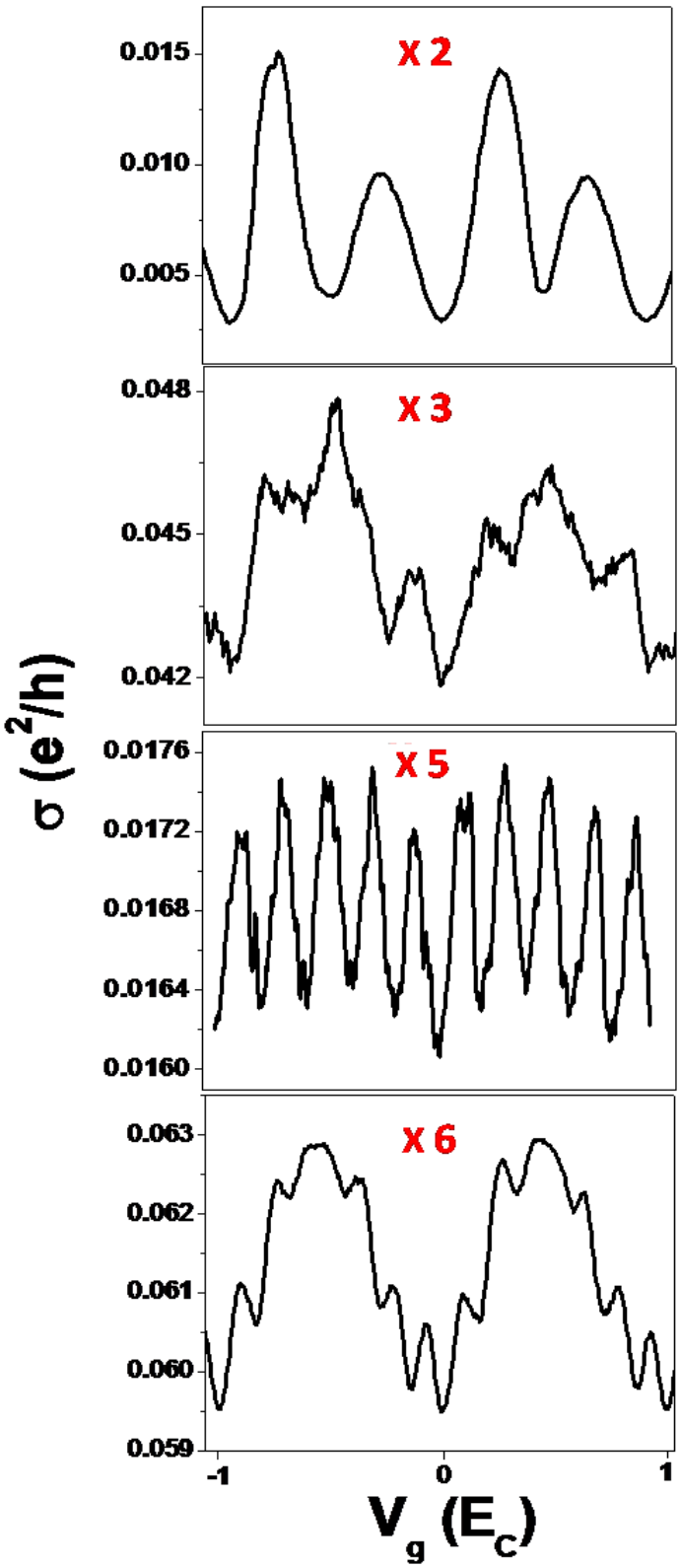

Figure 4.10: $\sigma(V_g)$ curves of different dots showing different ratio between the two frequencies. The ratio, denoted by red text (top to down) is: 2, 3, 5, 6.

In the following sections we describe in details the dependence of the two periods on different energy scale: bias voltage (section (4.2.2)), coupling (section (4.2.3)) and temperature (section (4.2.4)).

4.2.2 The dependence of the two periods on bias voltage

In this section we show how the conductance develops when changing the bias voltage, V_{sd}, and how this change affects the appearance of the two periods. For each sample we took several $\sigma(V_g)$ curves at different bias voltage. An Example for such $\sigma(V_g)$ curves is presented in Fig. 4.11.

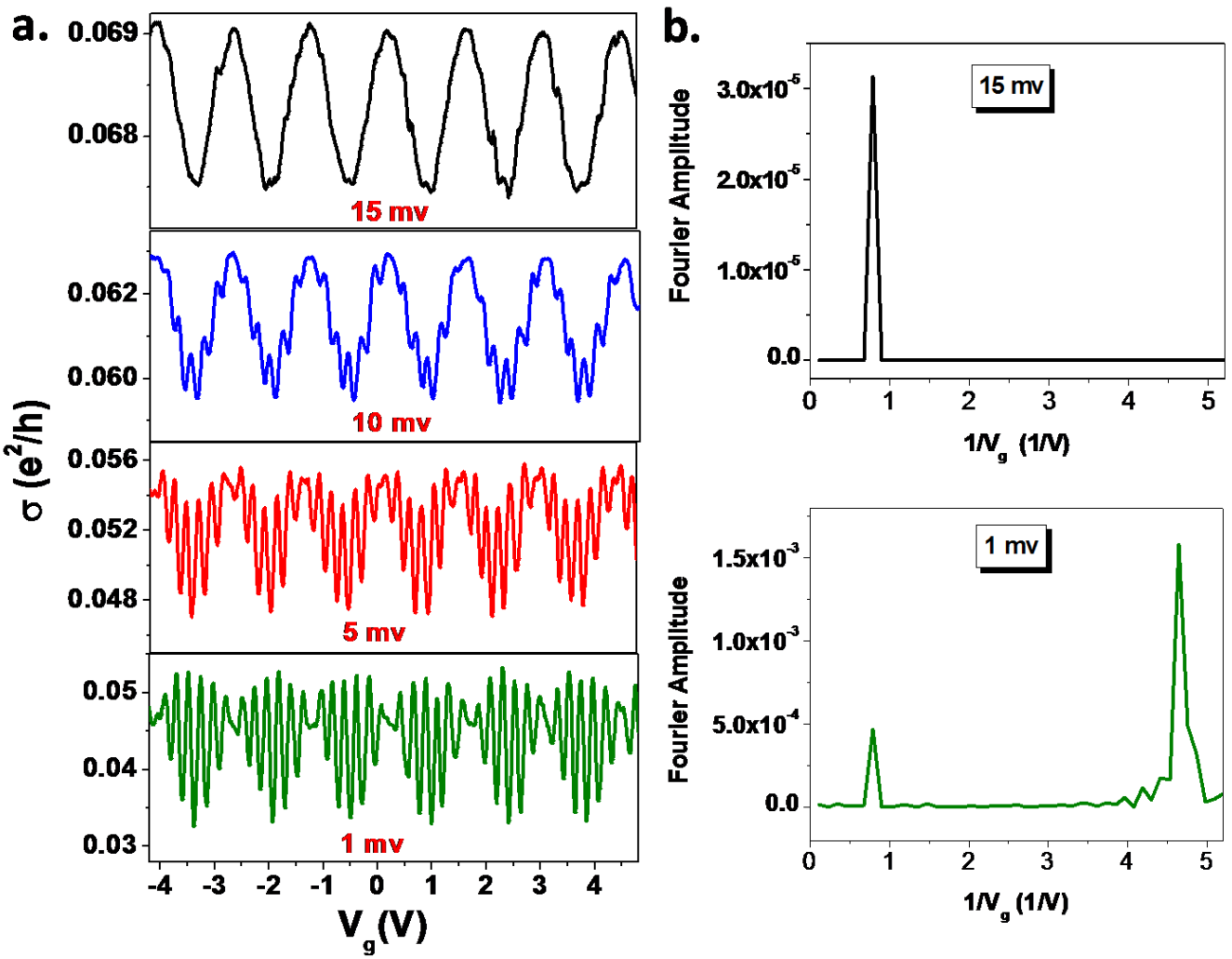

Figure 4.11: a) $\sigma(V_g)$ curves at different values of bias voltage. **b)** The FT for the curves measured at $V_{sd} = 1mV$ (green curve) and $V_{sd} = 15mV$ (black curve).

The conductance curve taken at bias voltage of 15mv exhibits clear periodic peaks with a single periodicity. Indeed the FT shows that one period governs the conductance (Fig. 4.11b). One can easily see that when decreasing the bias voltage an additional period appears in conductance as is shown for $V_{sd} = 10mv$. When we further decrease the bias voltage the faster period becomes more dominant so that two clear periods are observed in the conductance. At low enough bias of 1mv the conductance exhibits a very nice beat structure. Here the FT shows two well defined periods, where the amplitude of the fast period is even larger than the original slow period. Hence, by decreasing the bias voltage we are crossing over from a slow period to a faster period.

An additional example is shown in Fig. 4.12. In this case the coupling is weaker and the measured resistance is higher. In contrast to the previous example, here, the transition from slow period to fast period occurs at lower values of bias voltage, $V_{sd} \approx 0.5mv$. It is seen that for large bias voltage, $V_{sd} \approx 1mV$, which is well below the charging energy, the conductance is dominated by a slow period. When decreasing the bias voltage the peaks line-shape become asymmetric then they change to double peak structure. Eventually, at low enough voltage ($V_{sd} \approx 0.1mv$) the conductance is dominated by a different period which seems to be around twice the original period. This crossover from slow period to fast period can be observed in the FT shown in Fig. 4.12b. The Fourier amplitudes are normalized to the amplitude of the slow period. At $V_{sd} \approx 1mV$ only one slow period is revealed (green curve). When decreasing the bias voltage, a faster period emerges and at low bias voltage, $V_{sd} \approx 0.1mv$, the amplitude of the fast period exceeds the amplitude of the original period (see black curve).

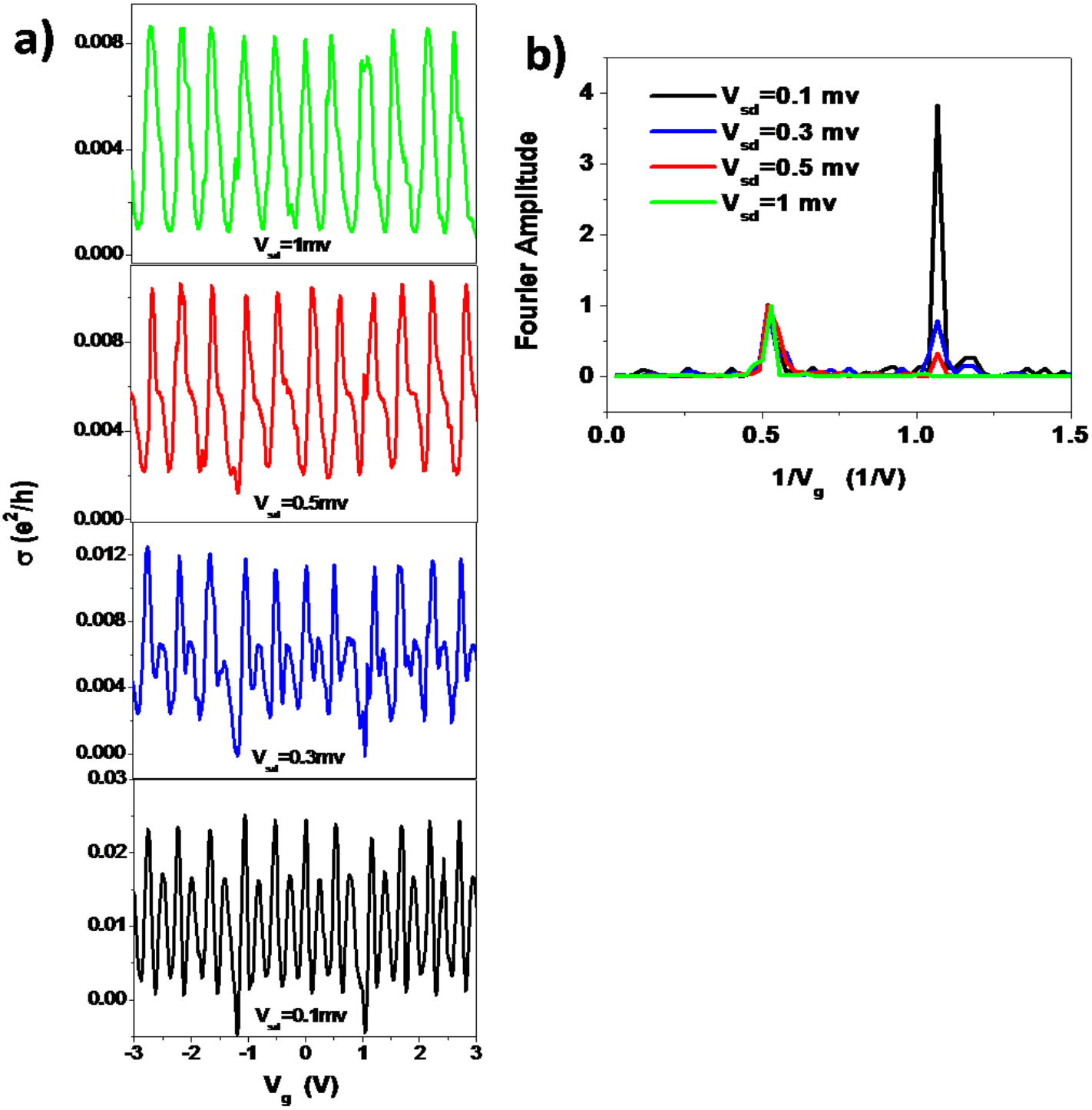

Figure 4.12: a) conductance as a function of gate voltage at different values of source-drain voltage. **b)** FT of the conductance curves presented at **a).**

In order to understand how both periods behave with decreasing the bias voltage we plotted in Fig. 4.13 the FT amplitudes of the two periods as a function of the bias voltage. One can clearly see that when bias voltage is increased both periods decrease but with different rate. The fast period decreases exponentially with increasing bias voltage while the slow period decreases much slower.

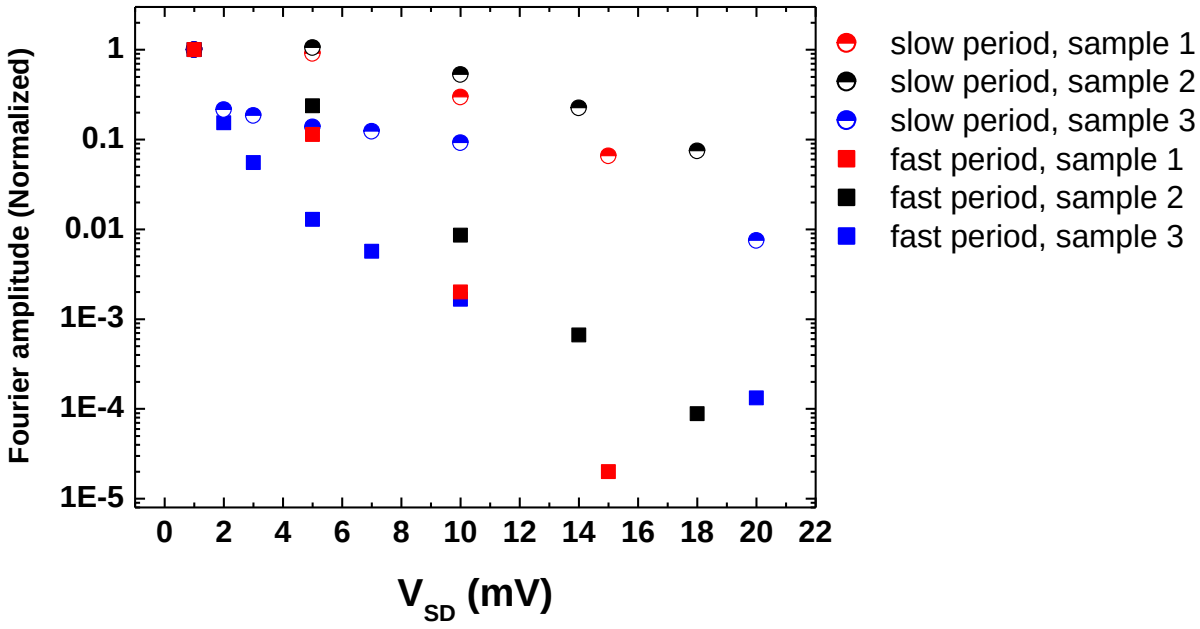

Figure 4.13: The Fourier amplitudes of the conductance periods as a function of bias voltage.

4.2.3 The dependence of the two periods on Coupling

Next we discuss the dependence of $\sigma(V_g)$ on coupling on the sample presented in Fig. 4.11. In this sample the frequency of the fast period is six times larger the frequency of the slow period. Two conductance curves of this sample at two coupling degrees are presented in Fig. 4.14a. At the weaker coupled stage (stage 1) the conductance shows very nice beat structure where two clear periods are observed. Here the FT shown in Fig. 4.14b reveals two main periods and confirms that the frequency of the fast period is indeed six times larger than the frequency of the slow period. At the stronger coupling stage (stage 2) the slow period disappears and only the fast period survives. This can be seen also in the FT. Here, the FT is not normalized to the value of the slow period, therefore, we can easily see that both periods decrease with the coupling but the slow period seems to decrease faster so that for the strongest coupled stage only the fast period survives.

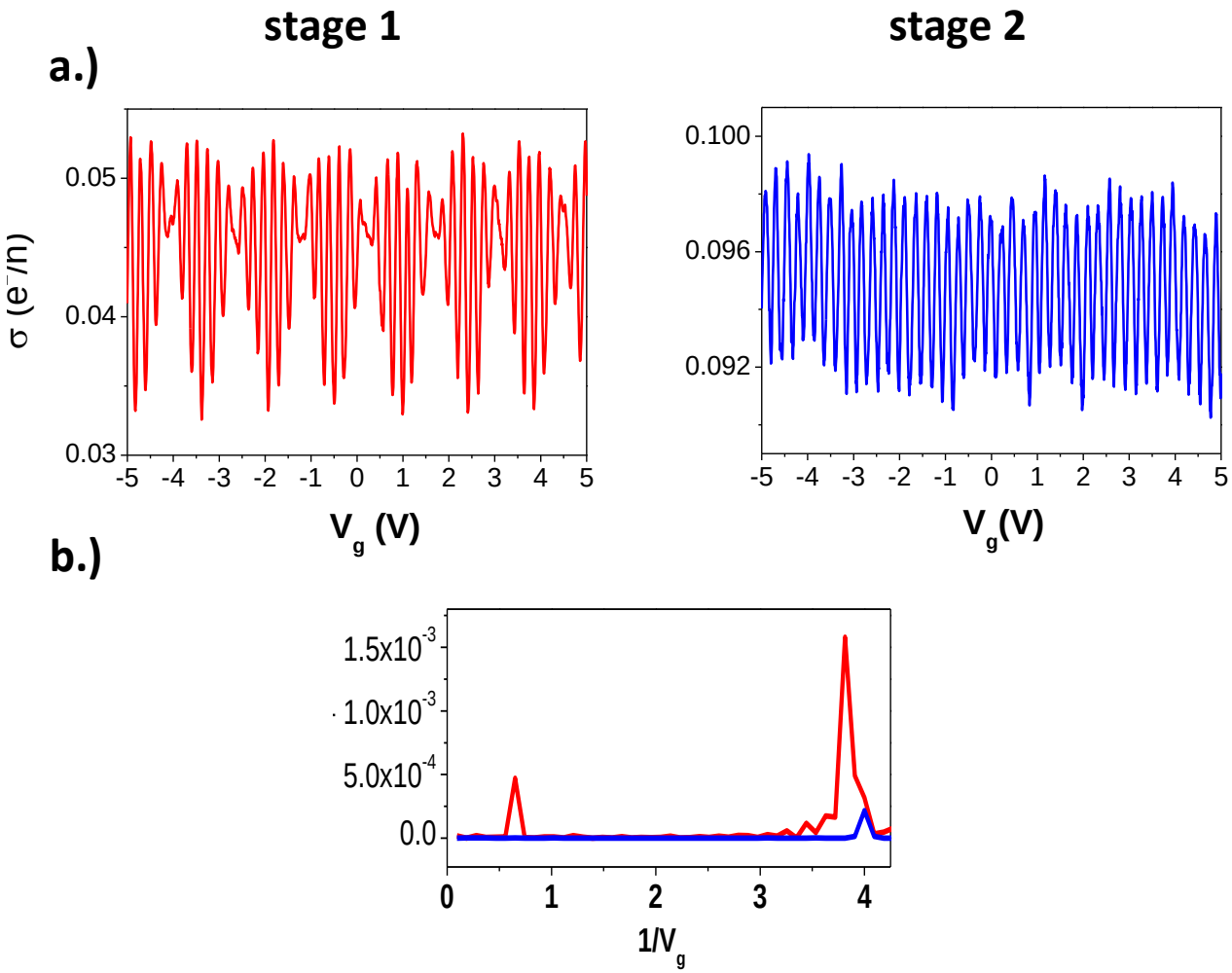

Figure 4.14: a) $\sigma(V_g)$ at two different coupling degrees of the same sample. The red curve represents the more weakly coupled stage (stage 1). The blue curve represents the more coupled stage (stage 2). **b)** FT of the curves presented at a).

In Fig. 4.15 we summarize the dependence on both the coupling and the bias voltage for the sample of Fig. 4.14 in a 3D presentation. Two graphs are for two different coupling strengths. Y axis represents the log of the source-drain voltage, X axis represents the gate voltage. The color represents the height of the conductance, yellow for high conductance value and red for low conductance value. The cuts in the graphs are due to discrete values of the bias voltage. Looking at stage 1 in the Y direction, top to bottom (decreasing the bias voltage), it is clearly seen that the period changes from a relatively slow period to a fast period which is six times larger. When the coupling is increased the fast period becomes dominant so that in the more coupled stage (stage 2) only the fast period is observed. At stage 2 the slow period is not observed for any value of bias voltage.

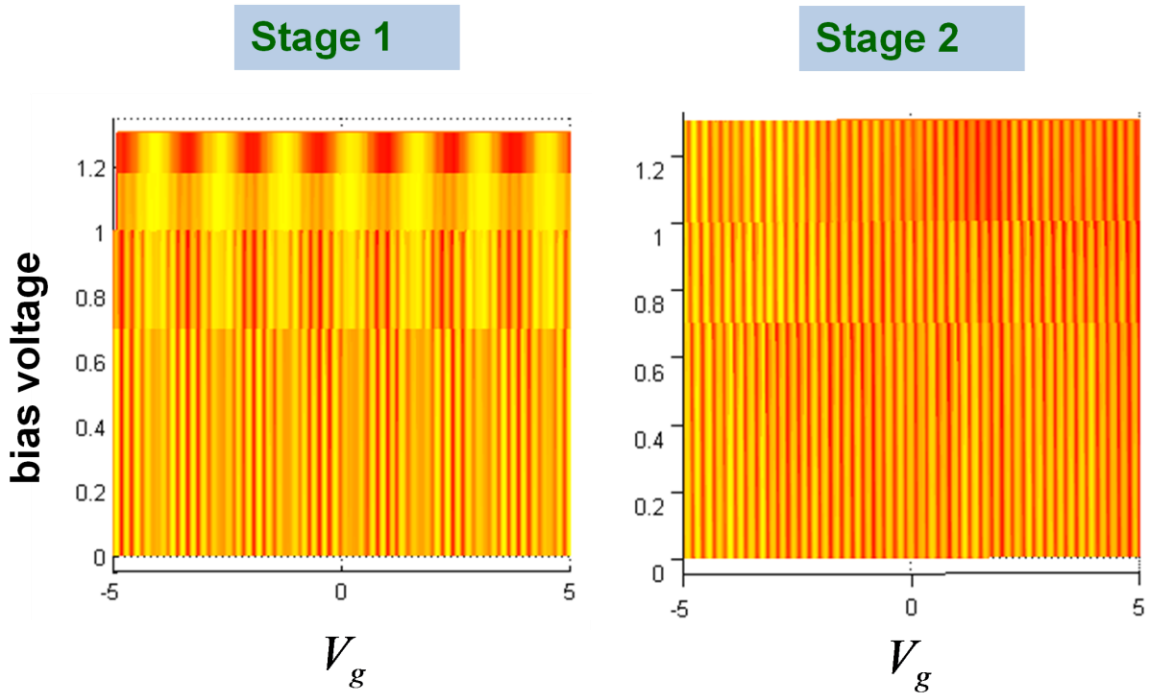

Figure 4.15: The dependence of $\sigma(V_g)$ on bias voltage and gate voltage in 3D presentation at two coupling degrees.

Thus, we conclude that the slow period is more sensitive to the coupling and decreases with the coupling more rapidly than the fast period.

Let us we examine the dependence of each of the two periods on the coupling to the well connected lead, g_D. Here g_D is the fitting parameter extracted from Eq. (4.3) (see section (4.1.2)).

In Fig. 4.2.11 we plot the FT amplitude of the slow period of 11 different dots as a function of g_D. The FT amplitude is extracted from $\sigma(V_g)$ curve taken at V_{sd}=1mV and is defined as $\frac{g_{\max} - g_{\min}}{g_{\max}}$.

One can clearly see a sharp decrease of the slow period amplitude as g_D increases. As we mentioned in section 4.2 the slow period is attributed to the CB oscillations. The exponential decay shown in Fig. 4.16 fits very well the explicit expression for strongly coupled dot appearing in Eq. (4.3), i.e. the CB amplitude decreases as exp(-g_D). This reinforces our confidence in the analysis based on Golubev and Zaikin describing conductance of a strongly asymmetrically coupled metallic dot and given by Eq. (4.3).

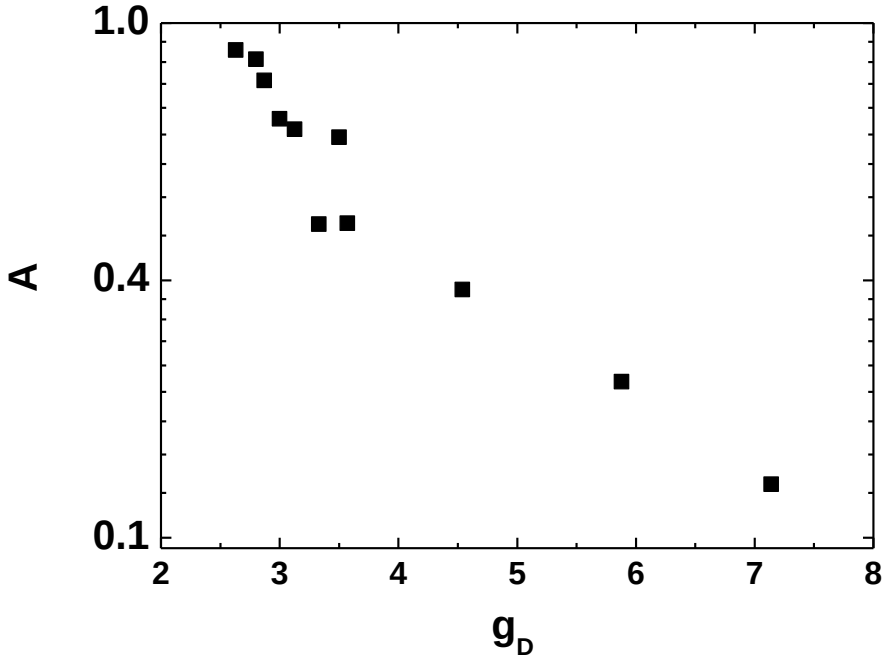

Figure 4.16: Amplitude of the CB oscillations at small V_{sd} defined as $\frac{g_{\max} - g_{\min}}{g_{\max}}$ as a function of g_D extracted from the fits to Eq. (4.3) for 11 different dots.

In Fig. 4.17 we plot the FT amplitude of the fast period for all samples, for which $V_{sd} = 1mV$, as a function of g_D.

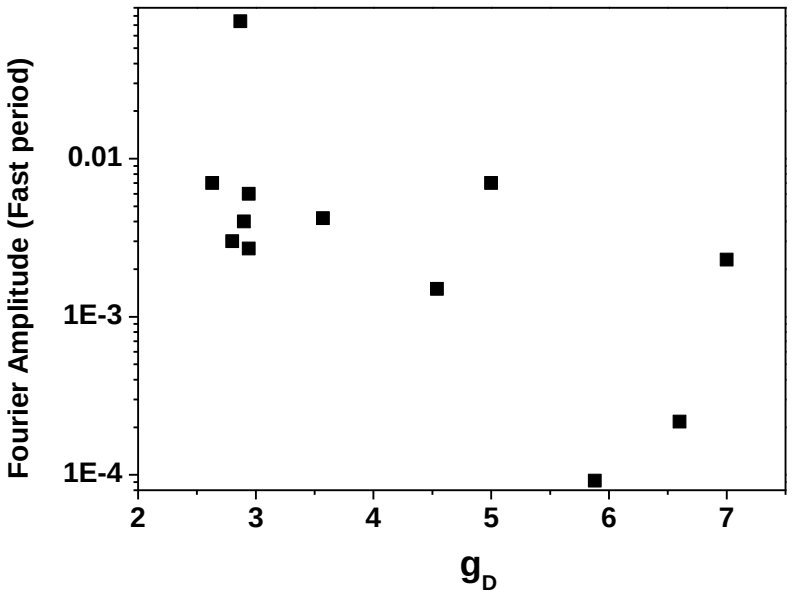

4.17: Fourier amplitude of the fast period of different samples for which the supplied V_{sd} is 1mv as a function of g_D.

One can see that the scattering is very large, and one cannot derive any clear conclusion based on this representation. The reason for this large scattering could be the following:

The voltage below which the fast period is observed is sample dependent. For example, in the sample presented at Fig. 4.11 the fast period is observed for bias voltage smaller than 10mv while in the sample presented at Fig. 4.12 the fast period is observed only for bias voltage smaller than 1mv. In Fig. 4.18 we plot the value of V_{sd} above which the relative amplitude of the fast period is smaller than 0.1 (in other words the amplitude of the fast period is smaller than 10% from the slow period).

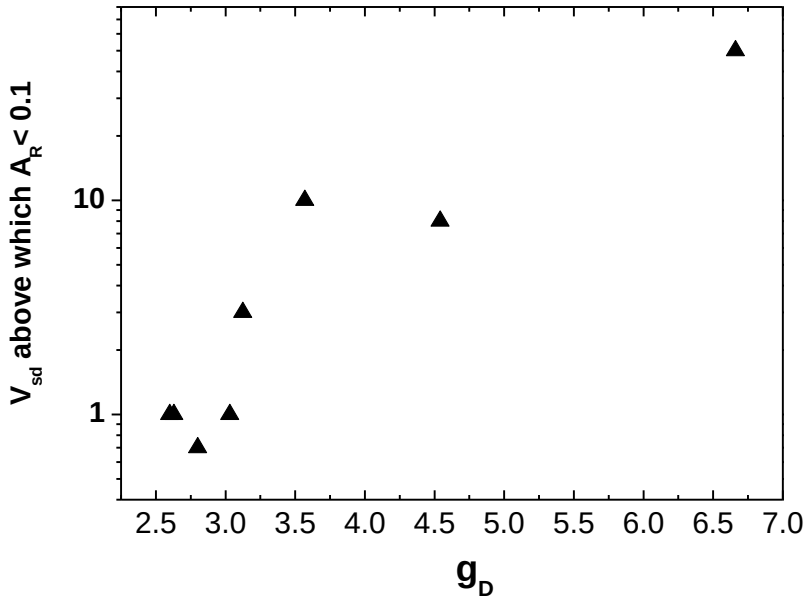

Figure 4.18: The value of V_{sd} of different samples above which the relative amplitude of the fast period is smaller than 0.1.

Fig. 4.18 shows a clear trend. As g_D becomes larger, the value of V_{sd} below which the relative amplitude of the fast period is observed is larger. This trend can result from the difference of the voltage drops on the drain and source barrier. The larger is the asymmetry, the smaller is the voltage drop on dot-drain barrier. Hence, sample in which asymmetry is large, larger supplied voltage is required for achieving a certain voltage drop on dot-drain barrier. Due to this effect it might be not correct to compare between different samples for which the applied bias voltage is identical but one needs to take into account the voltage drops on the each barrier. One can ask if it is justified to plot in Fig. 4.16 the CB oscillation (slow period) of different samples for which the applied voltage is V_{sd}=1mv without considering the voltage drop on the dot-drain barrier. This can be explained from Fig. 4.13 which shows that the slow period does not change much as a function of bias voltage at small values of bias voltage.

For the reasoning above, we compared samples for which the voltage drops on the dot-drain barrier is equivalent. The extracted g_D is very large, $2 < g_D < 8$, while the measured conductance is much smaller, $g < 0.1$. Therefore, $g_{S,}$ which is the conductance between the dot and the source, is

found to be more than two orders of magnitude smaller than g_D and most of the voltage must drop on the dot-source barrier. The values of the voltage drops on the dot-drain barrier are as small as few μV.

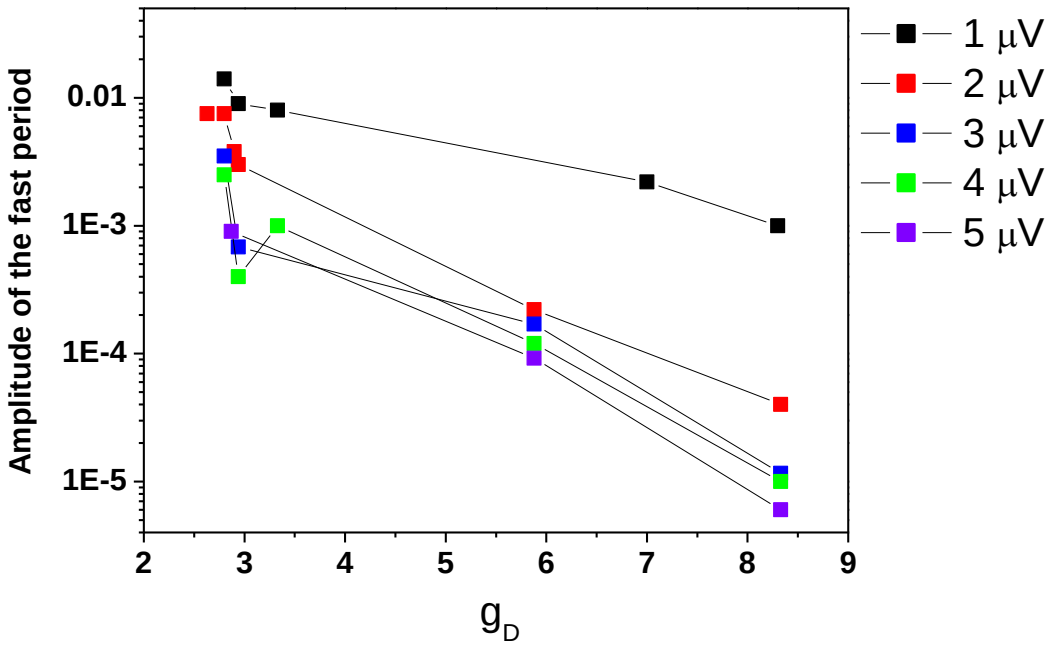

Figure 4.19: FT amplitude of the fast period as a function of g_D. Different curves are for different voltage drops on the dot-drain barrier.

Fig. 4.19 shows the FT amplitude of the fast period of samples for which the voltage drop on dot-drain barrier is identical, as a function of g_D. The five presented curves are for five different voltage drops on the dot-drain barrier. A clear trend is observed. As coupling is increased the amplitude decreases exponentially.

Fig. 4.19 manifests additional trend. It is seen that as the voltage-drop on the dot-drain barrier becomes larger, the curves exhibit lower values of the fast period amplitude. This trend is consistent with what we have already shown in Fig. 4.13 where the fast period decreases exponentially with the bias voltage. However, the voltage dependence in this case is not expected since the temperature (333 μV) exceeds the voltage drops (1-5 μV) by two orders of magnitude. Observing clear voltage dependence in the regime $k_B T >> eV$ is very surprising and will discussed in the next chapter.

4.2.4 The dependence of the two periods on temperature

Conductance measurements were taken at different values of temperatures. In Fig. 4.20 we plot the FT amplitudes of the two periods as a function of temperature for different samples. It is seen that both periods decrease exponentially with temperature and no clear difference of the affect of T on the period amplitude is observed.

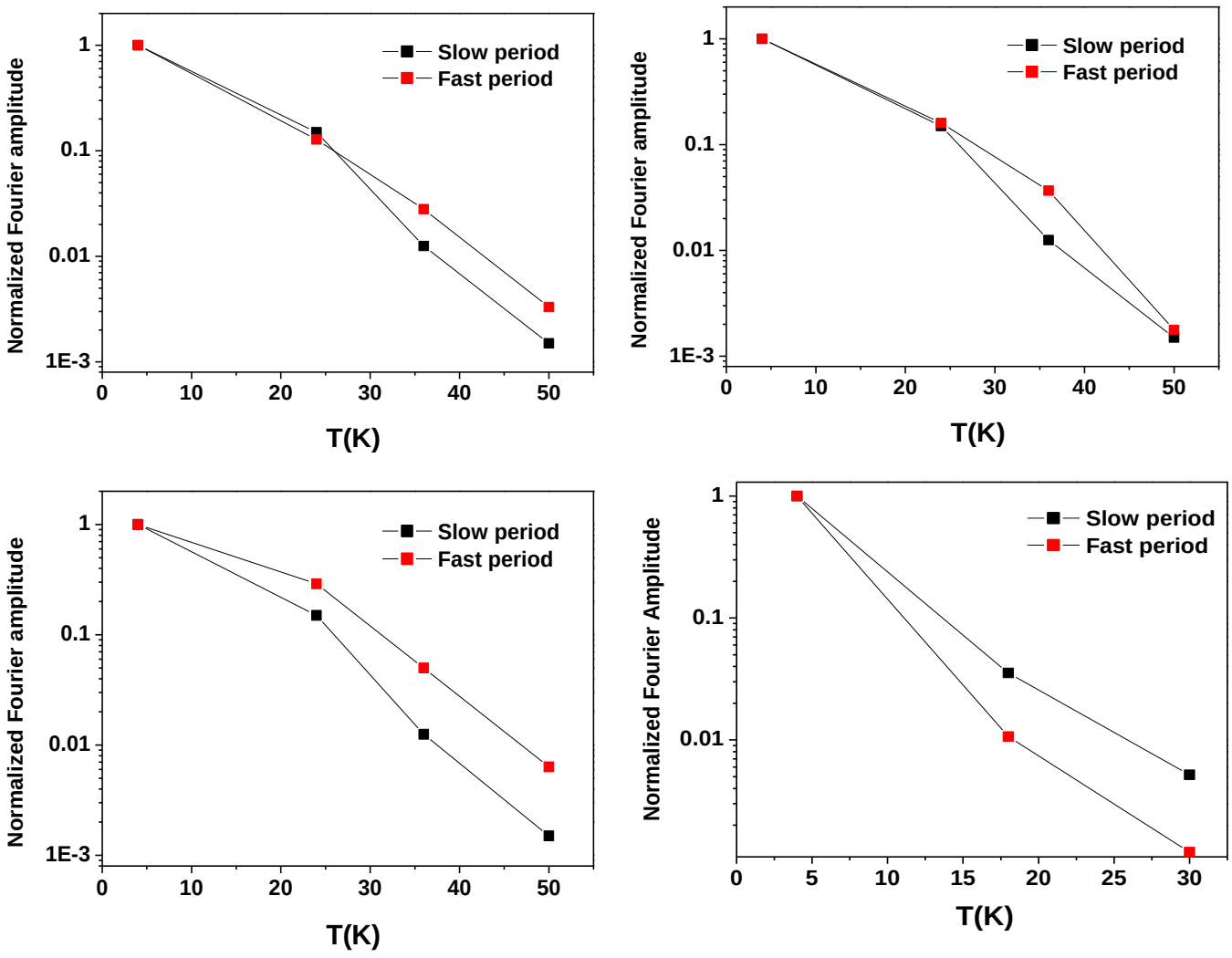

Figure 4.20: FT amplitude of the two periods as a function of temperature for different samples

CHAPTER 5

DISCUSSION

In the previous chapter we presented the results of the transport experiments performed on our metallic QDs. In this chapter we discuss the implications of these results. We suggest a number of possible scenarios which could account for the findings and discuss the merits and shortcomings of each of these. During the discussion we propose additional experiments and theoretical works which could shed further light on the results. Several experimental results which were not presented in chapter 4 are presented during the discussion since they are used to clarify points raised in this chapter.

For the sake of this discussion, the main results which were described in chapter 4 are listed below:

1. The $\frac{dI}{dV_{sd}} - V_{sd}$ exhibits simultaneously two effects resulting from electron-electron interactions: a large resistance dip near Fermi energy termed the ZBA and a set of CB staircase.

2. $\sigma(V_g)$ curve is characterized by two periods. The slow period refers to the CB oscillations while the physical origin of the fast period is unclear and is the main issue of this chapter.

3. The two periods mentioned above behave differently with respect to the coupling and the bias voltage.

When increasing the coupling both periods decrease exponentially but the slow period decreases faster and exists only at relative low coupling strengths. For very high coupling strength only the fast period survives (see Fig. 4.14).

The dependence on the bias voltage has the opposite trend. The fast period is more sensitive to a change in the bias voltage. When increasing the bias voltage the amplitude of the fast period decreases exponentially while the slow period seems to be less affected by small values of bias voltage as shown in Fig. 4.13.

4. The two periods mentioned above behave similarly as a function of temperature as shown in Fig. 4.20.

Throughout this chapter we will refer to these points and discuss their possible interpretations and significance.

In order to verify that the observed effects we described in the previous chapter originate from the dot and not from the leads or other chemical residues in the gap we applied the same experimental process including the electro-deposition to a sample with no dot inside the gap as is shown in Fig. 5.1a.

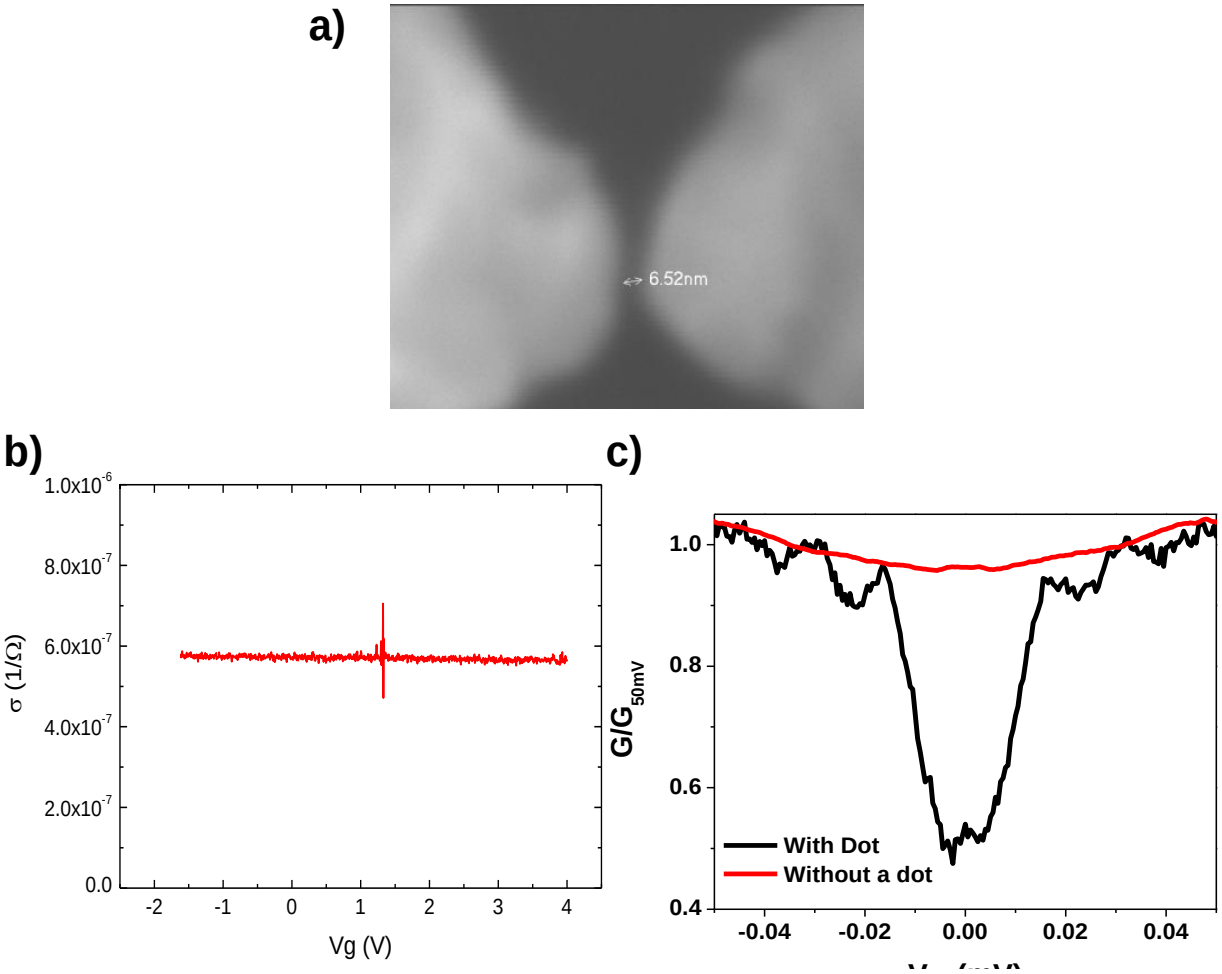

Figure 5.1: **a)** HRSEM image of source and drain electrodes separated by a very small gap of 6 nm after applying the electro-deposition process. **b)** $\sigma(V_g)$ curve of a sample with no trapped dot as presented in a). **c)** dI/dV_{sd} curves of two different samples. The red curve demonstrates the case in absence of a dot and the black curve demonstrates a curve in presence of a dot.

Fig. 5.1b depicts the conductance as a function of gate voltage, $\sigma(V_g)$, in a case where no dot is trapped between the electrodes. In this case no conductance peaks are observed. We applied this process to over 10 samples and none of them showed periodic behavior. Fig. 5.1c depicts the tunneling conductance as a function of V_{sd} in two cases: in the presence and absence of an Au dot trapped between the leads. It is seen that in the absence of a dot the tunneling conductance is nearly ohmic with a very small suppression near zero bias while in the presence of a dot the tunneling curves change drastically as is seen in the black curve of Fig. 5.1c: a large conductance minimum centered around zero bias is observed accompanied by a series of conductance oscillations. These results indicate that all phenomena observed in $\sigma(V_g)$ curve and in dI/dV_{sd} curve are due to the presence of the dot.

5.1 Characterization of the physical regime in our system

The measured gold colloids have a diameter of 30 nm yielding energy level spacing of $\Delta \approx 10\mu V$. Calculating the classical charging energy of gold colloid having radius of $R = 15nm$ taking into account that the dielectric constant is about $\varepsilon \approx 1.5$ yields charging energy $\frac{e^2}{C} = \frac{e^2}{4\pi\varepsilon\varepsilon_0 R} \approx 25meV$. The measurements were performed at $T = 4.2K$. Considering this, we are definitely in the classical regime where the charging energy is far larger than Δ and $k_B T$.

$$\Delta << k_\beta T << E_C$$

In all the measured $\sigma(V_g)$ curves the peaks height were identical. This is not surprising since this is expected from the classical regime as is shown in Fig. 1.4a.

Conductance versus gate voltage, $\sigma(V_g)$, of our least connected dot is shown in Fig. 4.6. Clear periodic conductance peaks are observed. These were attributed to CB phenomena. We noted that the width of the peaks is equivalent to the periodicity of $\sigma(V_g)$. We also showed that the peaks' width is neither temperature dependant nor voltage dependant. This implies that the peaks' width is determined by the level broadening, Γ. It is well known that as the coupling is increased the peak width becomes larger till the peaks overlap and the minima of the peaks are not observed so that the conductance manifests weak periodic modulation[22] as described in Eq. (1.4.24). Similar behavior is observed in our results. The conductance form has sinusoidal shape and the minima of the peaks do not reach zero. All this implies that the dot in our system is within the strongly

coupled regime where Γ is larger than the temperature and comparable to the energy level spacing.

An additional theoretical reinforcement to this claim is by comparing the measured curves to that expected from the Orthodox theory. Fig. 5.2 shows σ(Vg) curve and $I-V_{sd}$ curve for the same experimental energy scales: temperature, bias voltage, charging energy and the measured resistance. One can clearly see that our experimental results are far from filling the Orthodox theory of the weak coupling regime. Fig. 5.2 shows that the measured CB peaks (red curve) are much broadened than expected from the Orthodox theory (blue curve). Moreover, the theoretical $I-V_{sd}$ curve shown in Fig 5.2b (blue curve) predicts very pronounced CB and a threshold voltage is observed, below which the current is totally reduced. The measured $I-V_{sd}$ curve (red curve), however, is smeared at small voltages and no clear threshold voltage is obtained. This could be due to the fact that the charging energy is exponentially reduced in the strong coupling regime.

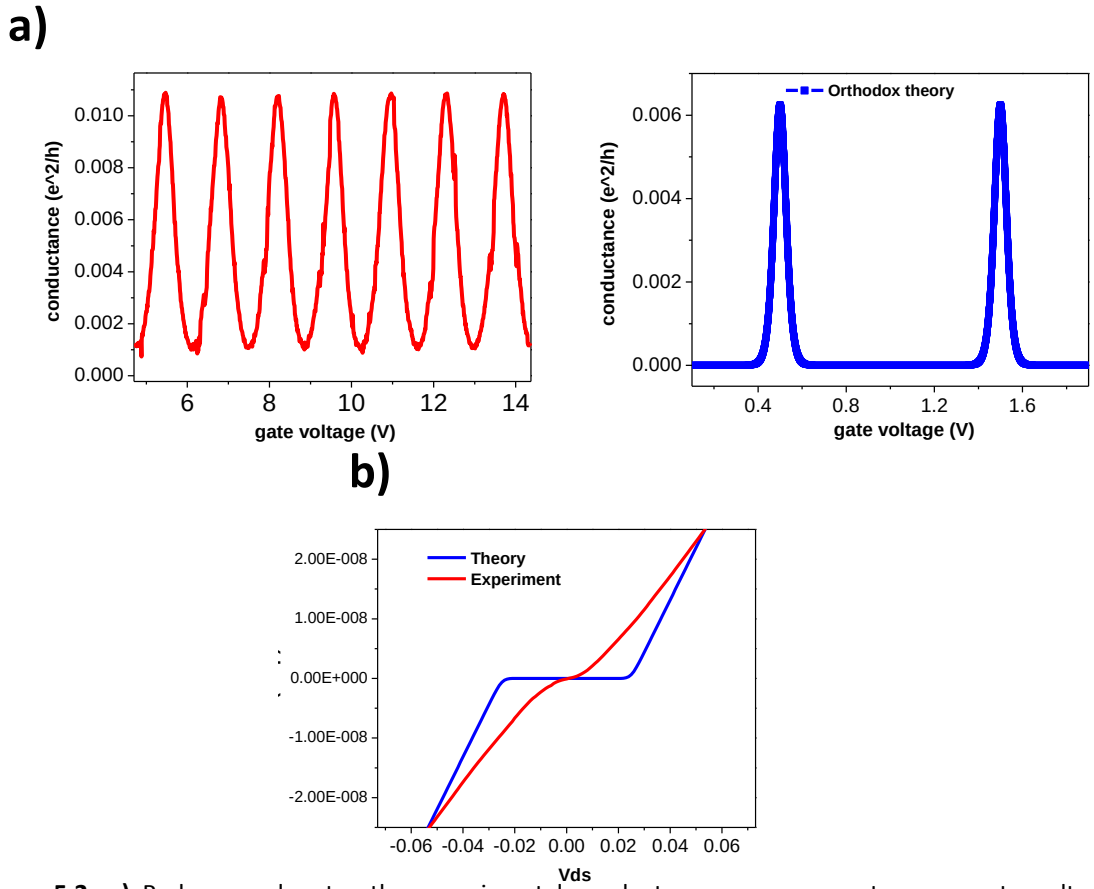

Figure 5.2: a) Red curve denotes the experimental conductance measurement versus gate voltage at $T=4K$ $V_{sd}=1mV$ and $E_C \approx 25meV$ while the blue curve denotes theoretical simulation of $\sigma(V_g)$ according to the Orthodox theory with the same values of energy scales as in the experiment. **b)** $I-V_{sd}$ measurement (red curve) and Orthodox theory simulation of $I-V_{sd}$ (blue curve) with the same values of energy scales denoted in a.

As was mentioned in the introduction the tunneling rate in the Orthodox theory is determined by the temperature and by the electrostatic energy difference before and after the tunneling event. This simplified calculation originates from the Fermi's Golden rule and is valid only in the weakly coupled regime where $\Gamma < \Delta$. The fact that we cannot fit our measurements to the Orthodox theory although we are in the classical regime reinforces the claim that our system is in the strong coupling regime.

This can explain why we do not obtain the CB "diamonds" structure in the charge stability diagram shown in Fig. 5.1.2b as expected from the weak coupling regime. An example of CB "diamonds" measured on gold nanoparticles by Ralph et al[57] is shown in Fig. 5.3a. At zero bias voltage $\sigma(V_g)$ shows resonant peaks, but with increasing the bias voltage the peaks width becomes larger till the peaks overlap. In our case the situation is different. The peak width in our system is not bias voltage dependent. The peak broadening is so large that even at the lowest values of bias voltage the peaks overlap and do not reach zero. Hence, we do not observe the "diamonds" structure. The unique feature in our case is the emergence of additional period in the conductance at low values of bias voltage. This phenomenon will be discussed in section 5.4.

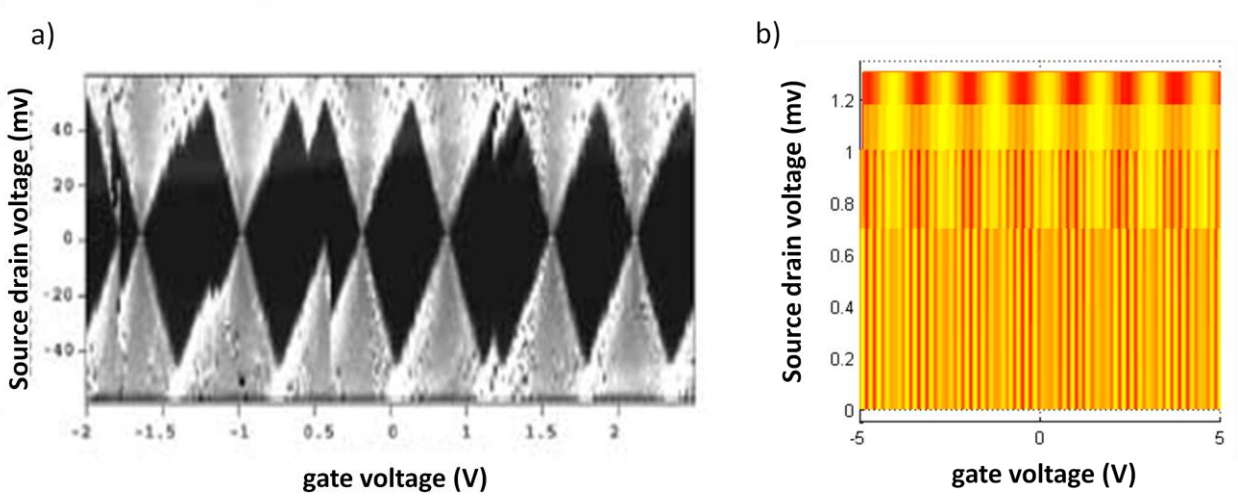

Figure 5.3: Charge stability diagram of a metallic QD in **a)** the weak coupling regime, measured by Ralph et al[1]. **b)** the strong coupling regime, measured in our system.

One may wonder how could it be that the conductance features show signatures of a strongly coupling regime while the value of the measured conductance is relative small, $\sigma(peak) = 0.005 \cdot \frac{e^2}{h}$. The only possible scenario which can explain this is that the dot is highly

asymmetrically coupled. Hence, it is not directly possible to estimate Γ from the conductivity $\sigma(V_g)$. Here Γ is defined by $\Gamma = \frac{\Gamma_S \cdot \Gamma_D}{\Gamma_S + \Gamma_D}$ where Γ_S and Γ_D are the tunneling rates to the right and left electrodes respectively. $\sigma(V_g)$ is governed by the weakly connected lead, Γ_S, resulting in a conductance through the dot which is much smaller than $\frac{e^2}{h}$ while the coupling to the well connected lead, Γ_D, may be relatively high. However, by fitting the $\frac{dI}{dV_{sd}} - V_{sd}$ curves to the theory of Golubev et. al. depicted in Eq. (4.3) we were able to derive g_D, the conductance between the dot and the well connected lead which is proportional to Γ_D. In the previous chapter we found that the extracted values for g_D are ranging between 2 and 8. These values are two or three orders of magnitude larger than the measured conductance which is in our case equivalent to g_S, the conductance between the dot and the source. This is consistent with the assumption that our dots are very highly asymmetrically coupled to the leads. An image of a QD asymmetrically coupled to the leads is shown in Fig. 5.4. The image was taken after the measurements were performed and shows very clearly that dot is more coupled to the left (drain) electrode.

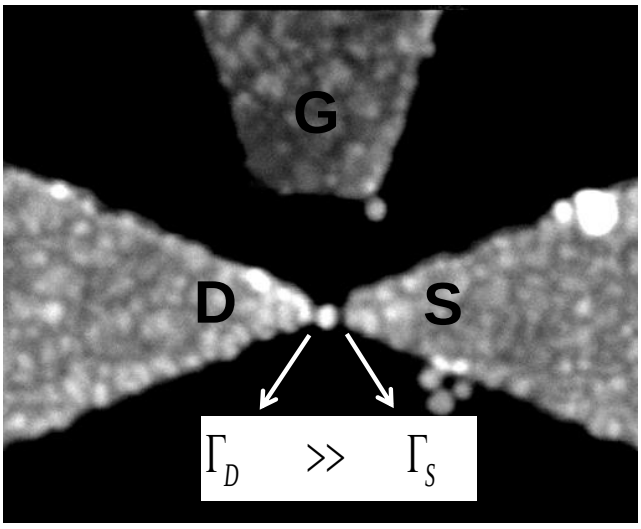

Figure 5.4: HRSEM image of a typical asymmetrically coupled QD. The image was taken after the measurements were performed.

The fact that we measure highly asymmetrically coupled QD system is not surprising. Actually it is a very natural outcome of the experimental process we use. Using AFM nano-manipulation by which we "push" a desired colloid to the gap can be expected to a QD which is better connected to one of the leads than the other. Moreover, one additional atom bridging one of the leads and the dot can

decrease the barrier resistance by an order of magnitude. This asymmetry plays an important role in the obtained results.

5.2 Coexistence of CB and ZBA in a strongly coupled metallic QD

In section 4.1 we showed that the $\frac{dI}{dV_{sd}} - V_{sd}$ curves are composed of two parts. One is a conductance minimum pinned to the Fermi level and is gate voltage independent, and the other is an oscillation with the bias voltage which shifts with the gate voltage. We analyzed the $\frac{dI}{dV_{sd}} - V_{sd}$ curves according to the work by Golubev and Zaikin[58] which describes the transport through mesoscopic metallic grains in the strong tunneling regime. The current they obtained, given by Eq. (1.6.14), is reduced below the classical result by an amount I_0 and is modulated periodically with the gate voltage. We derived the exact expression for the conductance in the physical limit which corresponds to our experiment (see Appendix A). Our derivation is expressed in Eq. (4.3). The second term in this Eq. demonstrates the Exchange term and is related to the ZBA effect. Here the ZBA is due to renormalization of the tunneling DOS by quantum processes resulting from e-e interactions in the dot, leading to suppression in the conductance at small energies. The last term in Eq. (4.3) corresponds to the Hartree term and is a pure *cos* modulation referred to as a CS. In contrast to the ZBA term, the CS is a classical effect and is related to the classical CB regime in which only the number of electrons in the dot plays a role and quantum processes are not relevant.

For most coupling strength one of these two terms will dominate over the other. For a weakly coupled dot ($g << 1$), the electron lingers in the dot for a long time (even in resonance tunneling) and the CB overshadows any other e-e contribution. The Hartree term prevents tunneling conductivity except at the degeneracy point. For a strongly coupled dot ($g >> 1$) the electron hangs around the dot only shortly before continuing to the lead and therefore one expects the Exchange term to dominate, resulting in a ZBA.

The current form predicted by Golubev and Zaikin is unique since it combines two different effects, the CB and the ZBA, each of them usually observed at different coupling regime. Both CB and ZBA contribute to the conductance at zero bias and therefore it is hard to distinguish between them near the Fermi energy. However, when the QD is asymmetrically coupled to the leads the CB effect manifests itself not only near the Fermi energy. In this case CS appears and demonstrates an oscillatory behavior of the conductance as a function of the bias voltage. If the dot is symmetrically coupled to the leads then the averaged charge Q_{av} in the dot becomes bias voltage independent:

$$Q_{av} == \frac{C_D R_D - C_S R_S}{R_D + R_S} \cdot V + C_g V_g = C_g V_g$$

Therefore, in the case of symmetrically coupled dot the last term in Eq. (4.3) has not oscillatory behavior with the bias voltage.

Thus, in order to observe both the classical contribution (CB) and the quantum contribution (ZBA) in the tunneling conductance, two conditions have to be fulfilled:

1. The dot has to be asymmetrically coupled to the leads.

2. Since the CB amplitude is predicted to decrease exponentially with g [59,60], there cannot be a wide coupling regime in which CB has not yet completely vanished while it is suppressed enough to allow a measurable ZBA and the two phenomena can coexist. Hence the best condition for g is $g \approx O(1)$, in which the CB is not totally suppressed but is suppressed enough to allow the ZBA effect appears.

In this sense our dot system demonstrates a unique geometry. On the one hand, the dot is strongly asymmetrically coupled so that the CS is observable. On the other hand, g_D is not too large so that the CB is not totally washed out, and the coexistence of ZBA and CB can be observed. To our knowledge, this is the first time these two effects were simultaneously measured and identified.

5.3 Experimental evidence of CB effect for g >1

In the strong coupling regime charge fluctuation in the QD is very large and the number of the electrons in the QD is no longer well-defined. Hence, one naively expects that CB oscillations may not be observed. Most of theoretical works have been concentrated on the weak coupling regime. However, in the introduction part, section (1.4.2), we mentioned several theoretical works[13-18] which predict that the CB effect, in case of a multi channel tunneling, is not destroyed even in the case of g > 1 but strong renormalization of the dot capacitance occurs. Experiments performed in the regime g > 1 utilizing 2DEG indicate, in agreement with the theoretical prediction, that if the transmission is close to 1 the conductance versus gate voltage shows periodic oscillations although the peaks are not well separated[11,12]. Our work serves as an additional experimental proof for the claim that CB effect survives even when the dimensionless conductance exceeds 1. Moreover, to our knowledge, our experiment shows for the first time that the survival of the CB when g > 1 is valid in a metallic QD as well.

In Fig. 4.16 we plotted the dependence of the CB period on the coupling to the well connected lead, g_D. We showed that the CB period exponentially decreases with the conductance. This is an

experimental evidence for the theoretical argument that the effective capacitance is strongly renormalized and exponentially increased with the conductance as is noted in Eq. (1.4.23).

5.4 The appearance of two periods in a single metallic QD.

The two extreme coupling regimes, the weak and strong coupling regimes, have been investigated intensively. However, the crossover from closed to open dots has not yet been thoroughly studied. Weakly coupled QDs exhibit conductance peaks as a function of gate voltage, Vg, with a well defined periodicity arising from the CB effect. Strongly coupled QDs show mesoscopic phenomena, such as UCF which is composed of many periods, resulting from interference effects. We find that the transition from closed dot to an open dot in our system occurs in a non trivial way. The most weakly coupled QDs exhibit a single period in $\sigma(V_g)$ curve. As we increase the coupling, the oscillations are accompanied by an **additional**, regular feature with faster periodicity. The finding that the conductance through a single metallic nanoparticle is characterized by **two** gate voltage periods is very surprising. One would expect to observe a single CB period in a weak coupling regime where the CB effect overshadows all other effects, or many periods such in UCF phenonmenon resulting from quantum interference effects that can be manifested only in strongly coupled systems where the CB effect is decreased and the mesoscopic nature of the sample can be realized. This mystery of observing exactly two periods will be discussed in details in this chapter.

In order to understand whether the two periods originate from the same physical origin we studied how these two periods behave as a function of different energy scales: coupling, bias voltage and temperature. We have shown that they behave differently with coupling and bias voltage but similarly with temperature.

The experimental results indicate that the slow period which is dominant in the relatively weakly coupled QDs is related to the CB effect. In all samples the slow period is totally suppressed at $V_{sd} \approx 45mV$ which is at the same order of magnitude of the charging energy in our system, while the fast period disappears at much lower values of voltage. The physical origin of the fast period is not straightforward and this issue will be discussed below.

The details of the fast oscillation are sample dependent. This is demonstrated in the following examples:

1. The value of bias voltage below which the fast period is observed is not identical for all samples. The appearance of the fast period can be as high as, $V_{sd} < 10mV$ but in most cases the fast period is observed only for $V_{sd} < 1mV$. In section 4.2.3 we showed that the value of the bias voltage above which the fast period is totally suppressed depends on the coupling to the well connected lead, g_D. High value of g_D results in low voltage drop on the dot-drain barrier, hence, larger bias voltage can be applied and the fast period is still observed. Thus, the applied voltage does not determine the strength of the fast period but both the coupling g_D and the voltage drop on the dot-drain barrier are responsible for the amplitude of the fast period.

2. The ratio between the frequencies of the slow and fast periods varies considerably from sample to sample. In most cases the ratio between the two frequencies is close to a factor of 2. However in some dots the ratio is approximately to 3, 5 or 6 (Fig. 4.10). We tried to check if there is any correlation between this ratio and other physical property in the system, but did not find any such correlation.

In the following we discuss several possible scenarios which could explain the existence of two periods in $\sigma(V_g)$ curve.

5.4.1. Double-Dot, Why not?

The appearance of additional period is very unexpected. A well defined nano-particle based dot is expected to show a single well defined CB period. Hence, a very natural explanation for two periods in conductance would be the presence of two dots participating in the transport. In section 4.1 we explored the characteristics of the $\frac{dI}{dV_{sd}}$ curves and we found a very strong theoretical correspondence to Golubev et al. work which describes the conductance of a strongly coupled **single** metallic dot. The fact that the measured $\frac{dI}{dV_{sd}}$ curves fit very nicely the theoretical prediction for the conductance of a single dot serves as a strong reinforcement that only a single dot is present between the leads.

In addition there are a number of experimental signatures that the presence of two dots between the leads is not a plausible scenario in our system. We searched very carefully for the origin of a second dot in the system. At the beginning of the fabrication process before we pushed the colloid into the gap, we made sure we did not image any other particles in the gap or too close to the gap. Only then we pushed a single colloid to the gap by the AFM tip. Moreover, imaging the samples by

HRSEM ensures that we have only one colloid which is trapped in the gap. In most of the cases the frequency of the fast period is twice larger than the frequency of the slow period. Hence, if the fast period originated from an additional dot, its size should be twice smaller than the QD we use (15 nm). This size should be easily observed by any sophisticated microscope. However, we did not observe any additional grain between the electrodes at any stage of the fabrication process using HRSEM or AFM imaging.

Furthermore, before ''pushing'' a gold particle between the source and drain we never measured conductance peaks as a function of gate voltage. We checked the possibility that a second dot originates from the leads and is created during the electrodeposition process by growing our electrodes one towards the other without placing a dot in the gap. These samples exhibited featureless $\sigma(V_g)$ as shown in Fig. 5.1b. Chemical analysis showed that the gold atoms are evaporated only on the electrodes and not on the SiO substrate. It is hard, therefore, to see what would be the physical origin of a second dot in our system. Hence, from an experimental point of view a double-dot scenario seems very unlikely in our case.

Beside these experimental considerations, one can ask what should be expected if indeed two dots are electrically connected either in series or in parallel between two electrodes. The conductance of a double dot system (DDS) consisting of two QDs coupled in series has been studied both theoretically and experimentally[61][62][63].

Similar to the case of asymmetrically coupled single-dot, lines of high differential conductance, corresponding to CS in the $\frac{dI}{dV_{sd}}$ curve are observed in DDS when a number of excess electrons on the two-dots changes by one. However in contrast to the single-dot device where only one slope is found and steps of CS are equidistant, two different slopes are expected in a DDS, resulting in steps of varying width. For instance, Steps of variable width have been observed in granular metal film using a scanning tunneling microscope and were explained by assuming a double-dot structure[64]. However, in our system all the dots show harmonic oscillation in the $\frac{dI}{dV_{sd}}$ curve with a well defined periodicity, which means that the $I-V_{sd}$ exhibits steps with identical width. The existence of a single periodicity in the $\frac{dI}{dV_{sd}}$ curve strongly indicates that there is a single dot between the leads.

Conductance resonances of a DDS as a function of gate voltage have been studied a lot both theoretically and experimentally[65]. In this system two gate electrodes are coupled to each of the

dots, or each dot is connected only to different electrode and these two electrodes determine the charge stability diagram of the DDS.

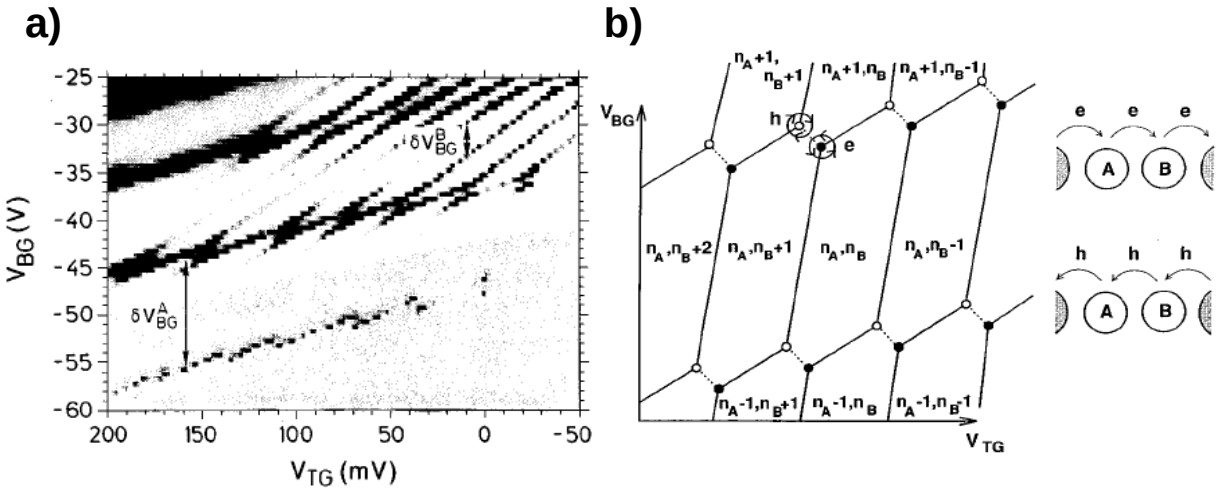

Figure 5.5: a) Measured Charge stability diagram of a DDS observed by R. H. Blick[6] et al. **b)** A magnified part of the charging diagram in a) is shown schematically.

In contrast to the conductance resonances of a single QD, the resonance pattern of the DDS shows two periodic oscillations, referring to the two charging energies of two "single" dots. Experiments which have been performed on a DDS exhibit the "honeycomb" pattern in the charge diagram. One example is the work done by Blick et al[66]. In their experiment they measured the conductance as a function of two gate voltages, top gate voltage (V_{TG}) and back gate voltage (V_{BG}). Each dot was coupled to both of the gate electrodes. The charge diagram they observed is shown in Fig. 5.5a. Depending on the two gate voltages, regions with different numbers of electrons in the two dots can be distinguished resulting in the "honeycomb" pattern. Instead of the common diamond picture of a single dot (Fig. 5.3a), honeycomb feature is observed and two periods are demonstrated by two sets of parallel resonance lines in the DDS charge pattern. It can be easily seen that the two sets of parallel resonance lines have different periodicity and different slope. One with a short period in gate voltage (δV^B_{BG}) and a large slope ($\delta V^B_{TG} / \delta V^B_{BG}$) and the other one with a long period (δV^A_{BG}) and a more gentle slope ($\delta V^A_{TG} / \delta V^A_{BG}$). The different slopes result from the different capacitative couplings of the two dots to the gate electrodes.

For a DDS a conductance resonance is found when an electron tunnels through both dots. The conditions for such a process are met whenever three boundaries in the charging diagram meet at a point. Two kinds of a triple point exist (points h and e in the Fig. 5.5b) one representing a tunneling from one lead to another and the other represents a tunneling for a hole from one lead to the other but in opposite direction. The positions of the two triple points depend crucially on the inter-dot coupling. For electro-statically decoupled dots the triple points are at the same position in the charging diagram. The electrostatic coupling lifts the degeneracy of these points and results in splitting of the resonance for different tunneling processes. The splitting of the triple points appears as an "anti-crossing" of the resonance lines. This splitting can be observed as a "double resonance" when one sweeps the two gate voltages by reaching the charge stability diagram at a specific slope/direction. In our experiment we observe a double period while scanning one gate voltage. Assuming we have an additional-dot in the system, the chance that we change each dot's energy in a way that we follow the direction of the triple point is close to zero. Considering the fact that we do not know the position of the "virtual" additional dot and nor its gate capacitance it is highly unlikely that this effect explain our results.

The DDS charge diagram is much more complicated than the case of a single dot due to the inter coupling of the dots. This picture shows that no matter what direction we move on the charge diagram, two regular periods cannot be observed. In our case, the FT shows that the two periods are close to harmonic, where one period is superimposed on the other.

Here, it is important to note that two periods in conductance are observed in over 15 samples. Assuming that additional dot is occasionally present between the leads at all of the measured samples is not reasonable and we are looking for a different scenario which can explain the regularity of the observed effect.

From all the above considerations we are compelled to give up the double- dot scenario and to assume that the cause for the two periods is an inherent property of a single nanoparticle. In the following sections we explore additional possible scenarios which could explain the existence of the two periods.

5.4.2 Population switching

Most of the experiments on QDs were performed in the weak coupling regime where $\Gamma < \Delta$ and the broadening Γ of the different energy states are more or less comparable to each other. However there could be a situation where there is a distribution of Γ and the widths of the energy states may vary by orders of magnitude. In our case the situation of non uniformity in Γ can by very natural. We control the dot-lead coupling by depositing atoms on the leads. Hence, the electrical connection could be via a single atom or very few atoms bridging the dot and the lead. In

this way we keep the number of channels in the barrier relatively small. At the same time, the number of the available energy states is very large as is expected from a metallic dot. It makes sense to assume that when we increase the coupling the levels get broadened and then a new base of energy levels is formed in which there are few strongly coupled states which are connected well through the channels and many other narrow levels which are much less connected to the leads. This situation of non uniformity in Γ was studied recently by few theoretical groups[22-24]. For instance they treat the case of one broad level which is connected well to the leads and additional ten levels which are very narrow. They found that the same broad level is repeatedly populated. They explained it by a mechanism of population switching. When levels interact with each other, then at some point the electron prefers to populate the narrow level instead of the broad level. Whenever a narrow level is filled, the broad level depopulates, the conductance decreases and then starts to fill the broad level again. This leads to number of successive CB peaks which are carried by the same well connected level since the population of this level is repeatedly cycled. The repeated filling of the same level can be reflected in the conductance in many different ways ranging from essentially no signature to saw-tooth or domelike structures to asymmetric CB peaks (Fig. 5.6a).

A similarity between the theoretical prediction for population switching and our measured conductance can be seen in Fig. 5.6.

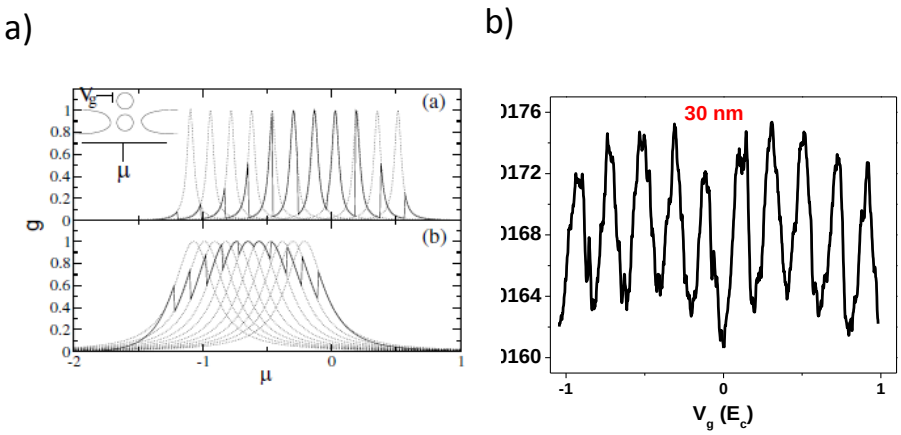

Figure 5.6: a) Conductance (solid line) through one connected level with ten disconnected levels as a function of the chemical potential[23] (or gate voltage) at two situations[20]: **Top:** when $\Gamma \leq \frac{e^2}{C}$ asymmetric peaks are observed. **Bottom:** When $\Gamma \geq \frac{e^2}{C}$ domelike structure is observed. **b)** $\sigma(V_g)$ of one of our QDs.

It is important to note that the theoretical works on the mechanism of population switching were studied for the equilibrium regime, $V_{sd} \approx 0$, and the effect of the bias voltage has not been taken

into account. However, in our system the measurements were carried out for relatively high bias voltage, $V_{sd} > 1mV$. Therefore, theoretical work is required in order to fully understand the relevance of this scenario to our results.

Three possible scenarios were considered using the mechanism of population switching in order to explain the existence of two periods:

1. Two types of energy states may exist. One type refers to levels which are very well connected to leads through the channels. Their level broadening is so large that it exceeds the charging energy, $\Gamma \geq E_C$. The other levels are weakly coupled to the channels and their width is very narrow. A schematic picture of the energy diagram is shown in Fig. 5.7a. An electron which populates the broad levels "spends" more time in the leads, and this population is less affected by the charging energy scale. Thus, these broad levels are observed in the background as an external envelope of the conductance structure and constitute the slow period, which is proportional to Γ of the broad levels. Whenever the gate voltage is increased by an amount of E_C an electron populates the narrow states. This leads to a decrease of the conductance and thus yields an additional regular feature in the conductance. The fast period is then attributed to the population of the narrow states and thus equivalent to E_C.

In our experiment we found that above specific value of bias voltage the fast period disappears while the slow period is still observed, which would mean that the population switching does not occur at high voltages. In order to apply such a scenario to our results, theoretical work for high voltages is required in order to understand the population switching out of equilibrium.

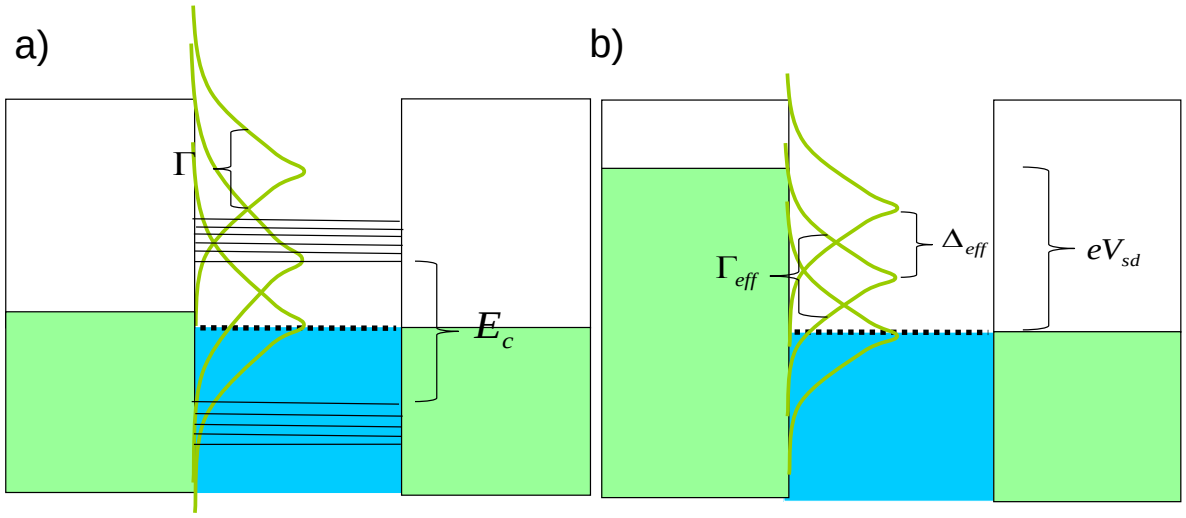

Figure 5.7: a) Schamitic picture of the energy scales according to scenario 1. **b)** Schamitic picture of the energy scales according to scenario 2.

The reason which causes us to give up this scenario is the dependence of the two periods on coupling. If applying this scenario it is not clear why the fast period which corresponds to the charging energy emerges only in the very strong coupling regime. Charging energy is expected to be manifested in the intermediate and weak coupling regime as well. Hence, we believe that the two periods demonstrate a different scenario.

2. When the coupling between the dot and the leads is very high the quantum energy levels as the electron wave function in the dot undergo hybridization. Hybridization of energy levels might yield a new set of energy spectrum including a set of broad states with a new effective broadening, Γ_{eff} . These states are separated by a new energy level spacing Δ_{eff} which is much larger than the original $\Delta \approx 1\mu V$ in our QD, $\Delta_{eff} >> \Delta$. If the new created Δ_{eff} is large enough so that it exceeds the temperature $T = 4K \approx 333\mu V$ then it can be resolved in the experience. A schematic picture of the energy diagram is shown in Fig. 5.7b. In the case of the regime: $E_C > V_{sd} > \Delta_{eff} \approx \Gamma_{eff} > kT$, one can assume the following process: Within the window of the bias voltage there exist many overlapping effective broad levels. When sweeping the gate voltage the levels are shifted and electrons start to fill up one of the broad levels. At some point, due to the electrostatic interaction between the levels, the electron "jumps" to the next broad level. Each time the electron starts to populate a different broad level we see a decrease in the current. According to this scenario the large period is attributed to the charging energy and the smaller period is attributed to Δ_{eff} . Increasing the coupling reduces the CB effect and erases any signature of the large period in the high coupling regimes. The above scenario does not contradict the survival of the fast period at high coupling regime since there could be oscillations of population switching although the CB is totally washed out. Clearly, this requires theoretical treatment to justify this claim.

We recall that increasing the bias voltage causes the fast period to disappear first. This can be explained by the postulation that when the window of the bias voltage is very large the system prefers to populate a more connected level with broadening that exceeds the window of the bias voltage. Hence, in this case there are no signatures of fast period. As was mentioned above, intensive theoretical work is required to understand the population switching at finite voltages.

Nevertheless, this scenario cannot explain the disappearance of the large period in the low voltage regime since the CB should be well observed in the nonlinear regime. Since such a scenario cannot explain the bias voltage dependence of the two periods, we do not believe that this is the direction to explain our results.

3. After discussing scenarios 1 and 2, we conclude that the existence of both broad levels and narrow levels in our dot does not seem to be consistent with the trend that the large period

dominates at high voltages and the fast period dominates at high degrees of coupling. We might need to assume that we have two systems of electronic states with different gate capacitance. This is similar to the case of two dots but here we might have **energetically** two dots in a physical single dot. A possible reason for this is the existence of surface states and bulk states. The surface states are more sensitive to the gate voltage but are only weakly connected to the leads because of their induced localization, and the bulk states are connected well to the leads but are less connected to the gate electrode. When gate voltage is applied, both types of states are shifted but the surface states are shifted more rapidly since their gate capacitance is larger. We start populating the bulk states but when a surface state crosses the bulk state the electron may prefer to populate the surface state. Since the surface states are swept much faster, a number of surface states can cross one broad level. At each cross point population switching occurs and this leads to a decrease in the conductance. Thus, the fast period is attributed to the surface states (narrow states). When high bias voltage is applied it is possible that the system prefers energetically to populate the bulk states (broad levels) and population switching isn't energetically favorable anymore. Thus, only the slow period which is attributed to the "slow" sweep of the bulk states with the gate voltage is observed.

From a theoretical point of view, applying a scenario of this type to explain our results would require theoretical understanding of population switching as a function of coupling and the bias voltage. From the experimental point of view, the requested question should be: what is the physical origin of the surface states. The physical origin could be either defects on the particle surface or the ligands on the surface. Most of the measured QDs contain trace elements of sodium citrate, tannic acid and potassium carbonate. This fact raises the question: how can traces of ligands create a set of consequtive states leading to a very regular period. Defects or residues of chemical elements are expected to be realized as traps in the system unless there exists a fully organized shell.

In order to experimentally study the effect of the surface properties on the fast period emergence, we performed the following checks:

1. We measured transport of several types of colloids with different surface materials. We prepared nanoparticles using different stabilizers resulting in different types of shells ranging from a well defined organic shell to an almost bare gold colloid having only residues of ligands on the surface. The procedures of the nanoparticles preparation is as following: Au nanoparticles (deoxygenated H_2O, 24 h, 20 ^{0}C) were produced by the citrate reduction of $AuCl_4$ anions ($HAuCl_4$, 17 %w HCl, H_2O, 60 ^{0}C)[67,68,69,70] . These Au nanoparticles were stabilized against aggregation by tannic acid. By this procedure Au nanoparticles of 25 +/-3 nm and 60 +/-5 nm were sensitized. Au nanoparticles, without capping agent and stabilizers were also produced by an aggressive reduction process using $NaBH_4$ as a reduction agent. In this process Au nanoparticles with broad size

distribution were obtained, 40+/-20nm.

2. We measured transport of colloids having different sizes. If the interplay between surface states and bulk states is the physical origin for the two periods, one can expect the ratio between the surface area and the volume of a nanoparticle to significantly affect the relative strength between the two periods.

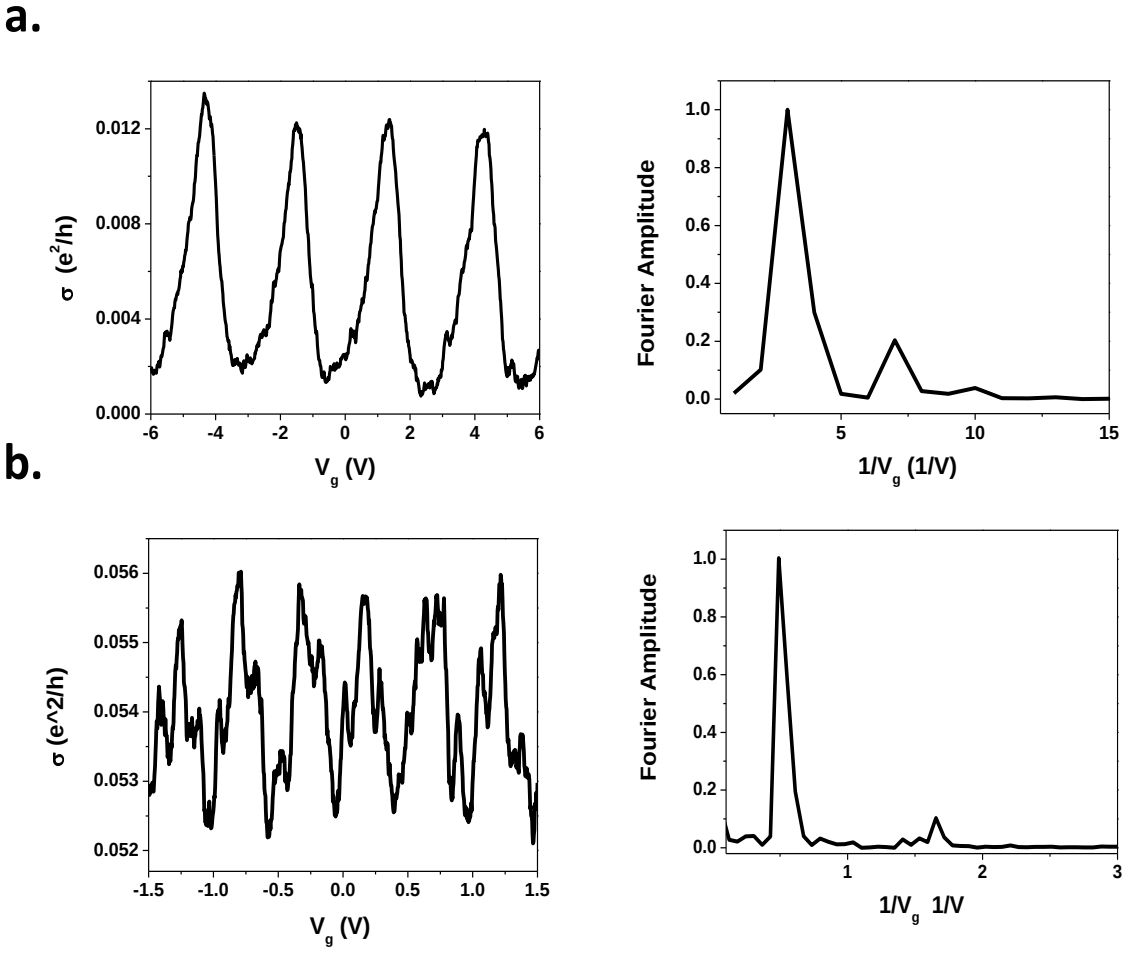

Figure 5.8: Conductance measurement of a QD having diameter of **a)** 20 nm and **b)** 60 nm. The FT in both cases reveals two periods.

Fig. 5.8 depicts $\sigma(V_g)$ of two colloids having diameter of 20 nm and 60 nm, each of them has different type of shell. The FT reveals two periods in conductance. The values of the relative amplitude of the fast period of these samples are within the range obtained for QD having diameter of 30 nm and no dramatic difference was observed. Moreover the ratio between the

frequencies of the fast and slow periods for the 20 nm QD and 60 nm QD are 2 and 3 respectively. These values do not differ from dots having diameter of 30nm which exhibit ratios between 2 and 6. To conclude, though the details of the structure (period frequency, amplitude etc.) differ from sample to sample the overall behavior of a structure combining two major oscillation periods is similar for all samples. We did not see any clear dependence on surface details or dot size as might be expected from a surface-state dependent process. Hence, we do not believe that a mechanism of population switching between surface states and bulk states is the physical origin for the two periods.

To conclude, we considered three different scenarios which are related to the mechanism of population switching and none of each was consistent with the details of our results. Therefore, we were compelled to give up the mechanism of population switching as a possible scenario to explain our results.

5.4.3. Interference effects

A possible scenario which could be related to the additional period is interference between electronic trajectories which would result in conductance fluctuations and is expected to dominate the transport for open dots.

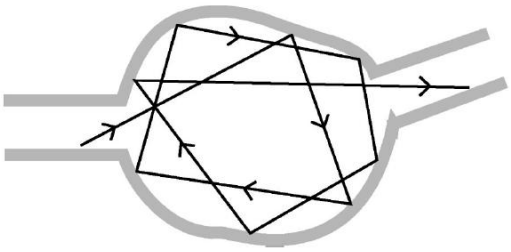

Fig. 5.9: Schematic drawing of a ballistic dot attached to two leads. The electrons move ballistically and are scattered several times from the dot's boundaries before exiting the dot.

In our system, the dot's size is few tens of nanometers and this size is much smaller than the mean free path in gold. Hence, the electrons move ballistically in the dot and might be scattered several times from the dot's boundaries as shown schematically in Fig. 5.9. We recall that in our case the ratio between the dot size and the Fermi wavelength (few angstroms) is relatively large and electron transport within the dot is then semi-classical rather than fully quantum-mechanical. A crucial consequence of the semiclassical regime is that the electron waves can be pictured as moving along classical trajectories. As they do so, the waves accumulate phase. If the dot size is smaller than the dephasing length, L_ϕ, interference between pairs of trajectories that intersect to

form closed loops, occurs. By sweeping V_g one can change the phase difference between the electronic trajectories via $\Delta k_F \cdot l$. Here l is the path length difference between a couple of electronic trajectories dominating the transport through the dot.

In order to check the relevance of interference to the observed fast period, we roughly estimated the value of l which corresponds to the measured conductance periodicity and Δk_F. The energy difference which corresponds to one period is:

$$\Delta E = E_{final} - E_{initial} = \frac{\hbar^2 k_f^2}{2m} - \frac{\hbar^2 \left(k_f + \Delta k_f\right)^2}{2m} \approx \frac{\hbar^2 k_f \Delta k_f}{m}$$

For one period the phase $\Delta k_f \cdot l \approx 1$, hence $\Delta E \approx \frac{\hbar v_f}{l}$, where $v_f = \frac{\hbar k_f}{m}$.

The Fermi wavelength λ_f in our dots is about $5 \cdot 10^{-10} m$, this yields $v_f \approx 1.3 \cdot 10^6 m/s$.

Also, we know that the frequency of the fast period is in most of the cases half the frequency of the slow period which refers to the charging energy, $E_c \approx 20meV$. This yields $\Delta E \approx 10meV$. Extracting l yields $l \approx \frac{\hbar v_f}{\Delta E} \approx 86nm$ which is about the size of the dot. Hence the path length difference between a couple of trajectories is about the size of the dot.

However, there are several experimental facts which raise doubts about this scenario. Here, we list some of them:

1. Interference effect should exhibit Aharonov-Bohm conductance oscillations as a function of magnetic field, B. The oscillations should be periodic in the magnetic flux $\Delta\phi = \Delta B \cdot S = \frac{h}{e}$. The magnetic field that corresponds to the area S enclosed by the trajectories, where $S = \pi R^2$ is the cross-section of the dot, is 6T. In order to check whether interference effects occur in our QDs we performed $\sigma(V_g)$ measurements at various magnetic fields in the range of 6T parallel to the substrates on three of our dots. In Fig. 5.10 we present several conductance measurements of the same sample at different magnetic fields. One can see that no significant magnetic field dependence is observed.

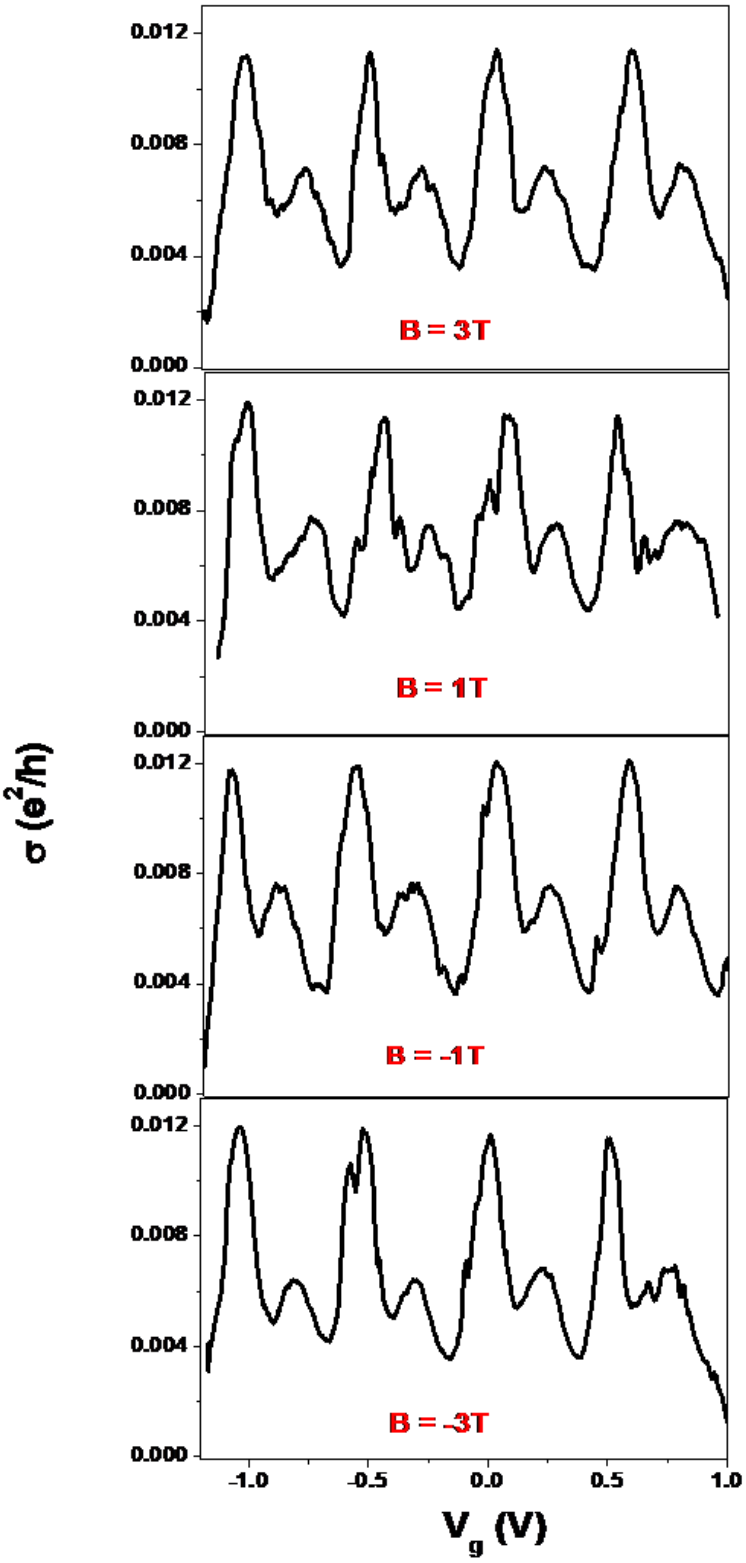

Figure 5.10: Conductance as a function of gate voltage at different values of magnetic field within the regime of 6T.

The fact that we were not able to detect any magnetic field dependence is not consistent with the scenario of interference effect. We considered the possibility that since our QDs are spherical, the area enclosed by the trajectories may be not perpendicular to the magnetic field. However, it is hard to believe that this is the case for all the three samples which we measured. Clearly one would like to perform measurement with different field orientations. This was not possible in the framework of the current study.

2. If applying such a scenario it is not clear why we observe only one additional period in conductance. The fact that a single period exists in the conductance limits the interference picture to only one pair of trajectories and there is no physical reason to assume this for all of the samples. A large number of trajectories are expected to interfere yielding many periods in conductance. For explaining this we considered the possibility that most of the electron trajectory length exceed the decoherence length L_ϕ in our QD so that only the non-scattered electron waves contribute to the conductance. If this is the case, the origin for the possible dephasing in our system which can make L_ϕ at the same order of magnitude as the dot size is still not clear.

3. The fact the fast period decreases with the coupling is not consistent with an interference picture. As coupling is increased the interference effect should increase as expected from strongly coupled dots.

4. If the slow period and the fast period originate from different physical origins (CB and interference effects) we do not expect them to behave similarly regarding to temperature as is shown in Fig. 4.20.

Nevertheless, we do not want to rule out the possibility of interference altogether for the following reason. Fig. 5.11 shows a $\sigma(V_g)$ curve of the sample presented in Fig. 4.14 for a more weak coupling stage. The conductance curve is very unique and exceptional since it presents a more complicated picture which is reminiscent of UCF structure. The FT here reveals several periods. The appearance of several periods in conductance is more consistent with the interference effect scenario. Thus, we still tend to believe that an interference picture could be relevant for explaining our results. We are looking for a dephasing process which could explain why only one pair of trajectories contributes to the conductance and why no magnetic field dependence is observed.

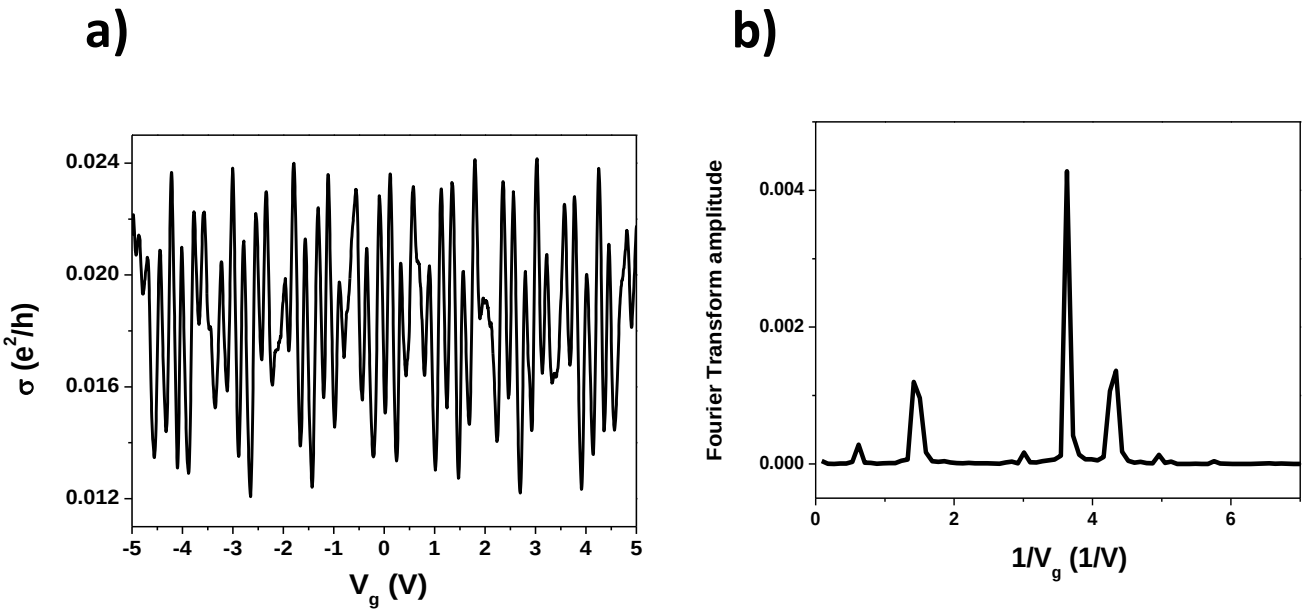

Figure 5.11: a) $\sigma(V_g)$ curve observed in one our QDs. **b)** FT of the curve presented at a).

5.4.4 Oscillation of the transmission probability

We considered the possibility that the fast period originates from the oscillation of the transmission probability of the electron through the dot.

The transmission probability of an electronic wavepacket from one lead to the other through the dot depends on the wavepacket overlaps at the interfaces between the dot and the leads. In our case the dot size exceeds much λ_F, hence, electron transport within the dot is semi-classical rather than fully quantum-mechanical. A crucial consequence of the semi-classical regime is that the electron waves can be pictured as moving along classical trajectories. By sweeping the gate voltage, we continuously alter the number of the electron waves along the trajectory L, causing the wavepacket details at interface to change. Consequently the transmission probability might fluctuate as a function of $\frac{L}{\lambda_F}$.

Such an effect could be observed only in a relatively strongly coupled dot in which the CB peaks are smeared and in the classical regime, $k_B T > \Delta$, in which single states, adding a random transmission coefficient amplitude, are not resolved.

However, a better theoretical understanding is required in order to clarify a number of issues such as why is there only a single, very regular period and what is the role of temperature and bias in suppressing this effect.

5.4.5 Higher order oscillations

In section (1.6.2) we presented the theoretical results for transport through small metallic grain in the strong tunneling regime, derived by Golubev and Zaikin[38,40,41]. In their work they describe single electron tunneling beyond the perturbation theory and the final result for the current is given in Eq. (1.6.14). In section (4.1.2) we analyzed this result regarding to the bias voltage. We recall that Q_{av} is gate voltage dependent as well. Here we focus on the conductance as a function of the gate voltage. Golubev and Zaikin took into account only low values of winding numbers[38] m=0, +1, -1. This yields only one harmonic in the current. When deriving the current for higher values of winding numbers one can expect that the current is composed of additional harmonics:

$$I(V) = G_{as}V - I_0(V) - gG_{as}Ve^{-F(T,V)}\cos(\frac{2\pi Q_{av}}{e}) + \sum_{m=\pm 2}^{\pm n} A(m)\cdot\cos(\frac{2\pi Q_{av}\cdot m}{e})$$

Theoretical work is required to derive the explicit expression for the amplitude $A(m)$. In order to understand whether these additional harmonics are related to the fast period observed in the measured $\sigma(V_g)$ curves, we need to check if the dependence of these harmonics on the coupling, temperature and bias voltage, manifested in the amplitude $A(m)$, is consistent with the behavior of the fast period in our measurements. The theoretical work for deriving the amplitude $A(m)$ is still in progress and once the explicit expression is obtained we will check the relevance of this scenario to our results.

Here we would like to note a very unexpected behavior of the fast period. Fig. 4.19 shows that the Fourier amplitude of the fast period is susceptible to the bias voltage drop on the dot-drain barrier, although the thermal energy is two orders of magnitude larger. We searched for a dephasing process for which the bias voltage dramatically affects the system although the temperature exceeds much the voltage, but we did not find any such a dephasing process. Other possibility is that such a behavior is manifested in the amplitude $A(m)$, but still theoretical work needs to be done. This issue is still a mystery and we are still trying to look for a physical process which can explain this trend.

CHAPTER 6

SUMMARY

Transport properties of a strongly coupled metallic QD were explored. The aim was to advance the understanding of the transport mechanism of a QD when crossing from a closed dot regime to an open dot regime. We presented a unique method by which we could connect a metallic QD between two leads and control the dot-lead coupling.

We found that a metallic QD in the strong coupling regime manifests very interesting and even unexpected results.

The $\frac{dI}{dV_{sd}}$ curve of a strongly coupled QD exhibits simultaneously two different effects: the CB and the ZBA. The coexistence of both effects can be observed thanks to unique geometry of our system. On the one hand, the dot is strongly asymmetrically coupled so that the CB staircase is observable. On the other hand, the conductance to the well connected lead is not too large so that the CB is not totally washed out, and the coexistence of ZBA and CB can be observed. To our knowledge, this is the first time these two effects were simultaneously measured and identified.

The $\sigma(V_g)$ curve showed very intriguing behavior. We found that $\sigma(V_g)$ curve is characterized by two periods. The slow period refers to the CB oscillations while the physical origin of the fast period is unclear and was the main issue of this work.

Although the $\frac{dI}{dV_{sd}}$ curve exhibits characteristics of a single dot, we considered the possibility that the two periods observed in $\sigma(V_g)$ originate from the presence of two dots between the leads. We showed that both from theoretical and experimental point of view the existence of two dots in our system is not a plausible scenario.

We suggested two different scenarios which are related to the mechanism of population switching between broad levels and narrow levels in a single dot. However, these scenarios were not consistent with the details of our results. Then we considered the possibility that interplay between two systems of electronic states: surface states and bulk states could be the physical origin for the two periods. However, we did not observe any clear dependence on surface details or dot size as might be expected from a surface-state dependent process. Therefore, we were compelled to give up the mechanism of population switching as a possible scenario to explain our results.

Additional possible scenario which could be related to the additional period is interference between electronic trajectories. However, this type of scenario is not consistent with the experimental details. First, we did not observe any magnetic field dependence as expected from interference effect. Second, the fact that a single period exists in the conductance limits the interference picture to only one pair of trajectories and there is no physical reason to assume this for all of the samples. Third, the temperature dependence of the fast period is different from what is expected from interference effect.

However, what still keeping us considering the interference scenario is an exceptional conductance picture observed in one of our samples, which shows a reminiscent of UCF. We are looking for a dephasing process which could explain why magnetic field dependence is not observed and why only one pair of trajectories contributes to the conductance. The origin of such a dephasing process is still not clear.

Furthermore, we considered the possibility that the fast period originates from the oscillation of the transmission probability of the electron through the dot. Theoretical understanding is required in order to clarify a number of issues such as why is there only a single, very regular period and what is the role of temperature and bias in suppressing this effect.

In addition, we found that the theory of Golubev et al.[40,41] might predict several harmonics in conductance through strongly coupled metallic grain. However, a theoretical work is required to derive the explicit expression for the current. This theoretical work is in progress and once the explicit expression is obtained, we should check if the behavior of the additional harmonics with regard to different energy scales is consistent with our results.

Finally, we considered several possible scenarios which can explain the existence of two periods in conductance. Some of them were found to be not relevant and other require a comprehensive theoretical work. Further progress in this work would benefit from a more detailed understanding of the relevant questions than that available at present.

[1] J. Bardeen, Phys. Rev. Lett. **6**, 57 (1961).

[2] T.S. Monteiro, D. Delande, A.J. Fisher, and G.S. Boebinger, Phys. Rev. B **56**, 3913 (1997) .

[3] Y. Alhassid, Rev. Mod. Phys. **72**, 895 (2000).

[4] R. C. Ashoori, Nature (London) 379413 (1996).

[5] M. A. Kastner, Phys. Today 24-31 (1993).

[6] I. L. Aleiner, P. W. Brower, and L. I. Glazman, Phys. Rep. **358**, 309 (2002).

[7] I. O. Kulik and R. I. Shekter, Sov. Phys. JETP **41**, 308 (1975).

[8] U. Meirav and E. B. Foxman, Semicond. Sci. Technol. **11**, 255-284 (1996).

[9] Mullen K, Ben Jacob E, Jaklevic R C and Schuss Z Phys. Rev. B. **37,** 98 (1988).

[10] Likharev K K IBM J. Res. Dev. **32,** 144 (1988).

[11] L. J. Geerligs, V. F. Anderegg, C. A van der jeugd, J. Romijn, and J. E. Mooij, Europhys. Lett. **10**, 1 (1989).

[12] "Single Charge Tunneling", Vol. 294 of NATO Advanced Study Institute Series, edited by H. Grabert and M. H. Devoret (Plenum Press, 1992).

[13] D. V. Averin and K. K. Likharev, in "Mesoscopic phenomena in solids", edited by B. L. Altshuler, P. A. Lee, and R. A. Webb (Elsevier, Amsterdam, 1991), P. 173.

[14] N. C. van der Vaart et al., Physica B (Amsterdam) 189, **99** (1993).

[15] C. Pasquier et al., Phys. Rev. Lett. **70**, 69 (1993).

[16] F. Guinea and G. Schon, Europhys. Lett. **1**, 585 (1986).

[17] J. Low Temp. Phys. **69,** 219 (1987).

[18] A. D. Zaikin and S. V. Panyukov, Zh. Eksp. Teor. Fiz. **94**, 172 (1988).

[19] A. D. Zaikin and S. V. Panyukov, Phys. Lett. A **183,** 115 (1993).

[20] G. Schon and A. D. Zaikin, Phys. Rep. **198**, 237 (1990)

[21] G. Falci, G. Schon, and G. T. Zimanyi, Phys. Rev. Lett. **74,** 3257 (1995).

[22] A. Furusaki and K. A. Matveev, Phys. Rev. Lett. **75,** 709-712 (1995).

[23] Book: " Mesoscopic Phenomena in Solids", edited by B. L. Altshuler, P.A Lee and R.A Webb (North-Holland, New York, 1991).

[24] J. P. Bird et al., Rep. Prog. Phys. 66 583 (2003).

[25] C. M Marcus, A. J. Rimberg, R. M. Westervelt, P. F. Hopkins, and A. C. Gossard, Phys. Rev. Lett. **69**, 506 (1992).

[26] M. J. Berry, J. H. Baskey, R. M. Westervelt, and A. C. Gossard. Phys. Rev. B **50**, 8857 (1994).

[27] M. J. Berry et al., Surf. Sci. **305**, 495 (1994).

[28] A. M. Chang, H. U. Baranger, L. N. Pfeiffer, and K. W. West, Phys. Rev. Lett. **73**, 2111 (1994).

[29] M.W Keller, O. Millo, A. Mittal, D. E. Prober, R. N. Sacks, Surf. Sci. **305**, 501 (1994).

[30] Book: "Nanoparticles: from theory to application", Edited by Gunter Schmid, Wiley-VCH Verlag GmbH & Co.KGaA.

[31] A. A. Guzelian, U. Banin, A. V. Kadavanich, X. Peng, A. P. Alivisatos, Appl. Phys. Lett. **69**, 1432 (1996).

[32] B. L. Altshuler and A. G. Aronov, in "Electron-electron interactions in Disordered systems", edited by A. L. Efros and M. Pollak (Elsevier, Amsterdam, 1985).

[33] G. Barak, G. Steiner, L.N Pfeiffer, K.W. West, L. Glazman, Felix von Hoppen and Amir Yacoby Nature Physics **6**, 489 (2010).

[34] Book: “Electron-electron interaction in disordered conductors” , B.L Altshuler and A. G. Aronov. P. 34

[35] A. M. Finkelshtein, Zh. Eksp. Teor. Fiz. **84**, 168 (1983) [Sov. Phys. JETP **57**, 97 (1983)].

[36] D. S. Golubev, Jurgen Konig, Herbert Schoeller, Gerd Schon and A. D. Zaikin, Phys. Rev. B **56**, no. 24, 15782 (1997).

[37] U. Eckern, G. Schon, and V. Ambegaokar, Phys. Rev. B **30**, 6419 (1984).

[38] D. S. Golubev and A. D. Zaikin, Phys. Rev. B **46**, 10903 (1992); Phys. Lett. A **169**, 337 (1992).

[39] D. S. Golubev and A. D. Zaikin, Pis’ma Zh. Eksp. Teor. Fiz. **63**, 953 (1996) [JETP Lett. **63**, 1007 (1996)].

[40] D. S. Golubev, J. Konig, H. Schoeller and G. Schon, Phys. Rev. B **56,** 15782 (1997).

[41] D. S. Golubev and A. D. Zaikin, Phys. Rev. B 46, 10903 (1992); Phys. Lett. A **169**, 337 (1992).

[42] Richard Berkovits, Felix von Oppen and Yuval Gefen, Phys. Rev. Lett. **94**, 076802 (2005).

[43] P.G. Silvestrov and Y. Imry, Phys. Rev. Lett. **85**, 12 (2000).

[44] C. Joachim J.K. Gimzewski, R. R. Schlitter, and C. Chavy et al. Phys. Rev. Lett. **74,** 2102 (1995).

[45] D. Porath, Y. Levi, M. Tarabiah, and O. Millo, Phys. Rev. B. **56,** 9829 (1997).

[46] C.T. Black, D.C. Ralph and M. Tinkham, Phys. Rev. Lett. **74**, 3241 (1995).

[47] M.A. Reed, C. Zhou, C. J. Muller, P.T. Turgin and J. M. Tour, Science **278,** 252 (1997).

[48] J. Reichert, R. Ochs, D. Beckmann, H. B. Weber, M. Mayor, and H. V. Lohneysen, Phys. Rev. Lett., **88**, 176804 (2002).

[49] H. Park, A. K. L. Lim, A. P. Alivisatos, A. P. Park, and P.L. McEuen, Appl. Phys. Lett. **75,** 301 (1999).

[50] A. Bezryadin, C. Dekker and G. Schmid, Appl. Phys. Lett. **71,** 1273 (1997).

[51] D. Porath, A. Bezryadin, S. de Vries and C. Dekker, Nature **403,** 635 (2000).

[52] D. L. Klein and P. L. McEuen, Appl. Phys. Lett. **68,** 2574 (1996).

[53] H. Lam and D. Natelson, Nanoletters **4,** 79 (2003).

[54] T. Dadosh, Y. Gordin, R. Krahne, I. Khivrich, D. Mahlu, V. Frydman, J. Sperling, A. Yakoby and I. Bar-Joseph, Nature **436,** 677 (2005).

[55] A. F. Morpurgo, C. M. Marcus and D. B. Robinson, Appl. Phys. Lett. **74**, 2084 (1999).

[56] D. S. Golubev, J. Konig, H. Schoeller and G. Schon, Phys. Rev. B **56,** 15782 (1997).

[57] Ferdinant Kuemmeth, Kirill I. Bolotin, Su-Fei Shi, and Daniel C. Ralph, Nano Lett. **8** (12) 4506-4512 (2008)

[58] D. S. Golubev, J. Konig, H. Schoeller and G. Schon, Phys. Rev. B **56**, 15782 (1997).

[59] X. Wang and H. Grabert, Phys. Rev. B **53**, 12 621 (1996).

[60] Y. V. Nazarov, Phys. Rev. Lett., **82**, 1245 (1999).

[61] N. J. Craig et al, Science **304**, 565 (2004).

[62] S. Sasaki et al., Pfys. Rev. B 73, 161303 (R) (2006).

[63] H. Jeong, A. M. Chang and M. . Melloch, Science 293, 2221 (2001).

[64] E. Bar-Sadeh, Y. Goldstein, C. Zhang, H. Deng, B. Abeles and O. Millo, Phys. Rev. B **50** 8961 (1994).

[65] Schaller et al., Phys. Rev. B **80**, 245107 (2009).

[66] R.H. Blick, R. J. Haug, J. Weis, D. Pfannkucha, K. v.Klitzing and K.Eberl, Phys. Rev. B **53**, 7899 (1995).

[67] J. Turkevich, P. C. Stevenson and J. Hillier, Discuss. Faraday Soc., 11, **5**5 (1951).

[68] G. Frens, Nature, 241, **20** (1973).

[69] Yonezawa, S.-Y. Onoue and N. Kimizuka, Chem. Lett.,**528** (2002).

[70] T. Yonezawa and T. Kunitake, Colloids Surfaces, A, Physicochem. Eng. Aspects, **149**, 193 (1999).